Università degli studi di Roma tor vergata

Anisotropy and anharmonicity in the zero-point motion of protons in ice and liquid water

Presented to the Physics Department

by

Davide Flammini

October 2012

Thesis for the degree of Doctor of Philosophy

Thesis Advisor : Dr. Roberto Senesi

To my family

Contents

Introduction

Despite the theoretical and experimental efforts done so far, the physics of ice and water still presents a very difficult challenge for physicists. Due to the key role played by water and ice in the biological systems and planet dynamics, a full understanding of the water molecule in all its phases is highly desirable.

Many other common liquids, as blood or milk, are mainly composed of water. Although a number of investigations have been carried out in the last century, water and ice present behaviors that are not or not fully understood or at least considered anomalous. A typical example is the water maximum density at a temperature higher than the triple point temperature (T = 4° C, at ambient pressure, see figure 1). Anomalous behaviors of water, with respect to a simple liquid (simple in the sense that does not present a high molecular interaction and it is well described by simple thermodynamic models), for example, are more than 60 [1], and they are a consequence of the microscopic structure of water molecule that can form very strong and directional bonds, named hydrogen bonds.

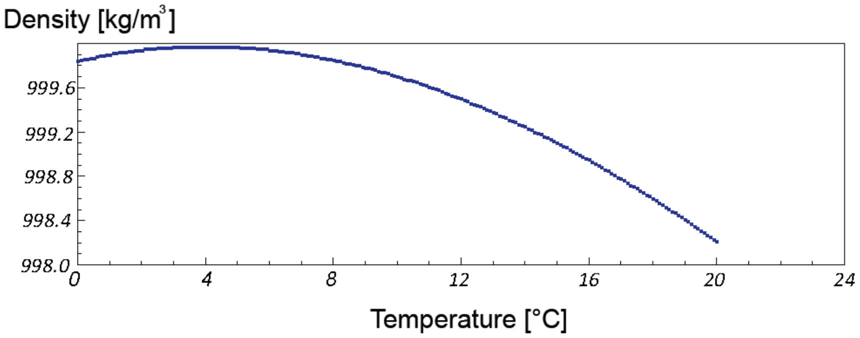

Figure 1: *An example of a water anomaly: the density at ambient pressure as a function of the temperature shows a maximum at $T = 4°$ C [2].*

In this work we will describe three neutron scattering experiments on water and ice. Two of them have been done using DINS (Deep Inelasyic Neutron Scattering), and carried out on polycrystalline and mono-crystalline ice at 271 and 130 K, respectively. The DINS experiments allow us to measure the momentum distribution and the mean kinetic energy of a target, that in the present case is the water proton.

The third experiment, carried out by INS (Inelastic Neutron Scattering), has been performed at 271 K on ice and, over a wider range of temperature (269-300 K), on water . Liquid water below the melting point (T = 273.15 K) is called supercooled water and it is a metastable phase.

In this thesis the data acquisition and data analysis will be discussed. It is important to note that this work introduces new steps in the data analysis that allow us to obtain new physical information such as the mean force experienced by the proton in the analyzed system [3].

In the following sections, after a short introduction on the water molecule, we will describe the addressed problems and we will summarize the state of the art of this kind of measurement. Finally we will give a description of the experiments done.

The water molecule

The chemical and physical properties of water and ice are due to its molecular structure. The oxygen atom has an external electronic configuration ($2s^2 2p^4$) that shows two atomic orbitals with one electron each. The superposition of two $1s$ orbitals of two hydrogen atoms (either with one electron each) with each other produces the two σ bonds of the water molecule (figure 2).

Experimental measurements show that the angle between the bonds of the hydrogens is 105° [4], and not 90°, as expected from from the perpendicularity of the p orbitals. This is due to the repulsion of the partially positively charged hydrogens, and to the hybridization sp^3 among the two O–H bonds and the two *lone pairs* of the oxygen atom. So the partial positive and negative charges are at the maximum distance with each other, forming a structure that is approximatively tetrahedral (the tetrahedron angle is 109.5° and the discrepancy is due to the charge distribution within the molecule).

Water possesses an asymmetric distribution of the electric charge: the oxygen atom is electronegative and it strongly attracts the bonding electrons, so that the center of the negative charge distribution corresponds approximatively to the oxygen. The center of the positive charges is instead on the bisector of the *O-H-O* angle at a distance from the oxygen that is very close to the *H-O* distance.

As a consequence water molecule has a dipole moment that has direction and sign going from the mid point of the segment joining two hydrogens to the oxygen. For free molecules this dipole moment has been determined experimentally to be $(6.186 \pm 0.001) \times 10^{-3}$ Cm [5],

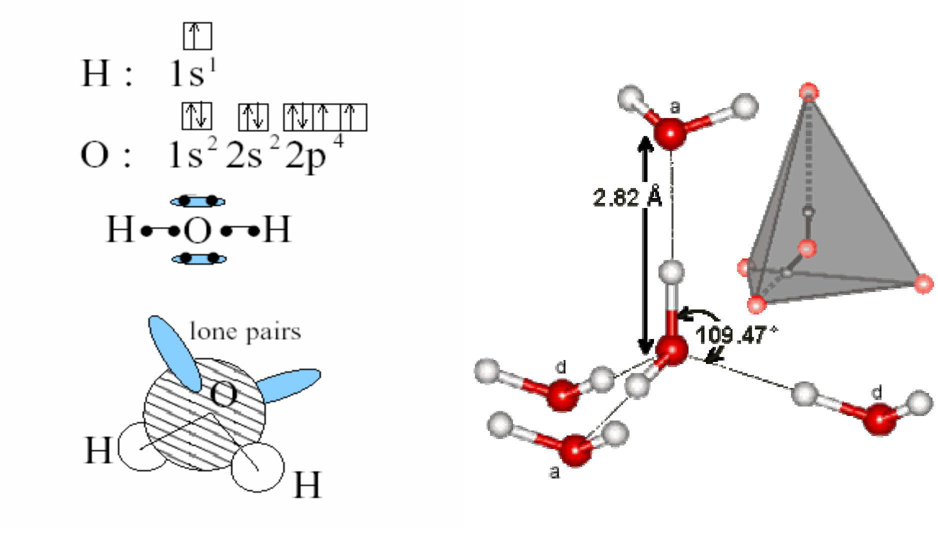

Figure 2: *Left side: electronic structure and covalent bonds of the water molecule. Right side: tetrahedral structure around a central molecule.*

value very close to more recent *ab initio* theoretical calculation [6].

Thanks to the dipole moment molecules interact, but, in the case of water, attractive forces assume strength and directionality that cannot be explained only with the presence of a dipole moment or unpaired charges. Such bonds, a mixture between covalent and ionic bonds, are named hydrogen bonds (H-bonds).

Hydrogen bond is a particular case of dipoles interaction and it was proposed as being responsable for the binding of molecules in water in 1929 by Latimer and Rodebush [7]. It is now known to account for the tetrahedral bonding of molecules in ice. It is a permanent dipole versus permanent dipole bond in which a hydrogen with a covalent bond with a very electronegative element (O, N or F) is involved. The electronegative element attract electrons acquiring a partial negative charge ($\delta-$) and leaving hydrogen with a partial positive charge ($\delta+$).

H-bond forms when the relatively high positive charge of hydrogen is located very close to an electronic doublet of a functional group, that binds the hydrogen so it is named acceptor. The group in which the hydrogen is covalently bonded is named donor. For example, in the OH group there is a partial negative charge in O and a positive one in the H, so the OH is partially polarized (permanent dipole). If this group meets another polar group, for example a carbonyl group, an electrostatic interaction generates.

Water molecule can form 4 H-bonds with 4 other molecules: two of them are acceptors, in the region of the hydrogens, and two are donors, thanks to the two lone pairs. These 4 bonds, when hybridized sp^3, generate a tetrahedral structure (see fig. 2) that is very easy to measure in the solid state [8], where each hydrogen atom is shared between two oxygen atoms.

In water there is a strong directional bond between an oxygen and a hydrogen atom that belongs to another molecule [9]. The ice, the stable solid state of water below 273 K at ambient pressure, is the best example of how water molecules can form a network of hydrogen bonds. Each molecule has four first neighbors and behaves as donor for two of them and as acceptor for the others. The result is that each molecule is surrounded by 4 molecules at the vertex of a regular tetrahedron and all the molecules form a *opened* web, bonded together by th H-bonds. When ice melts at ambient pressure the loss of this long range order causes a rise of the density of 9%.

The binding energy of the H-bond, around few kJ, is smaller than ionic or covalent ones, but larger than the Van der Waals forces. The low value of melting latent heat with respect to the sublimation heat is an evidence of the fact that most H-bonds persist in liquid phase. As a consequence in the liquid phase, even very close to the evaporation point, the tetrahedral symmetry is preserved at short range.

Ice Ih

In principle ice should be a material easier than water to understand, because the molecules are arranged on a regular lattice. However, the ice with which we are familiar (ice Ih) is just one of at least 13 crystalline phases which have been observed under different conditions of pressure and temperature. The crystal structures of ice Ih, and many of the other phases are unusual because, although the molecules lie on a regular crystal lattice, a certain amount of disorder is present in their orientations. This feature introduces a whole series of distinctive properties, of which the most significant are the electrical polarizability and conductivity. Ice can be described as a *protonic semiconductor* [10] and the theory of its electrical property is now well developed. The effort to reach a deeper understanding is relevant to more complicated systems in which proton transfer takes place along hydrogen-bonded chains in biological structures.

Ice is an important material both in our environment and as one of the simplest crystalline materials. It has many distinctive properties and moreover its structure is simple enough to be accessible to serious theoretical treatment. Great progress has been made in understanding the properties of ice, but the task is far from being complete.

Ice Ih is the normal form of ice obtained by freezing water at atmospheric pressure (or by direct condensation from water vapor above $\approx$ 171 K). The number I was assigned by

Tammann [11] following his discovery of the first of the high pressure phases of ice, and the h is commonly added to distinguish this normal hexagonal phase from a metastable cubic variant called ice Ic.

The phase diagram for the equilibrium between ice Ih and the liquid and vapor phase is illustrated in figure 3.

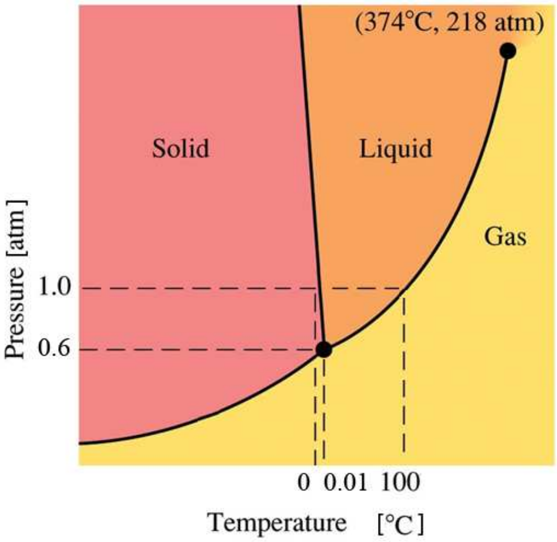

Figure 3: *Schematic phase diagram of water at low pressures (not to scale).*

The triple point, where the three phases are in equilibrium is, by definition, at 273.16 K, and the corresponding pressure is 611.7 Pa. The negative slope of the melting curve is a consequence of the fact that water expands on freezing, causing, for example, floating of ice on water.

The basic structure of ice Ih is well established to be that proposed by Pauling [12] and illustrated in figure 4. The oxygen atoms, shown by the open circles, are arranged on a hexagonal lattice with a structure named *wurtzite* (the hexagonal form of ZnS). Each oxygen atom has four nearest neighbors at the corners of a regular tetrahedron. The hydrogen atoms, shown as the dark spot, are covalently bonded to the nearest oxygen to form H_2O molecules, and these molecules are linked to one other by hydrogen bonds, each molecule offering its hydrogens to two other molecules and accepting hydrogen bonds from another two. The essential feature of the Pauli model is that there is no long range order in the orientation of the H_2O molecules or of the hydrogen bonds.

When ice condenses from the vapor it usually forms single crystals. These have a variety of shapes, including beautiful snow flakes, platelets, and less commonly needles depending on the conditions [13, 14]. These crystals reveal the hexagonal symmetry of the lattice of ice and, in accordance with standard crystallographic convention, the hexagonal axis is denoted

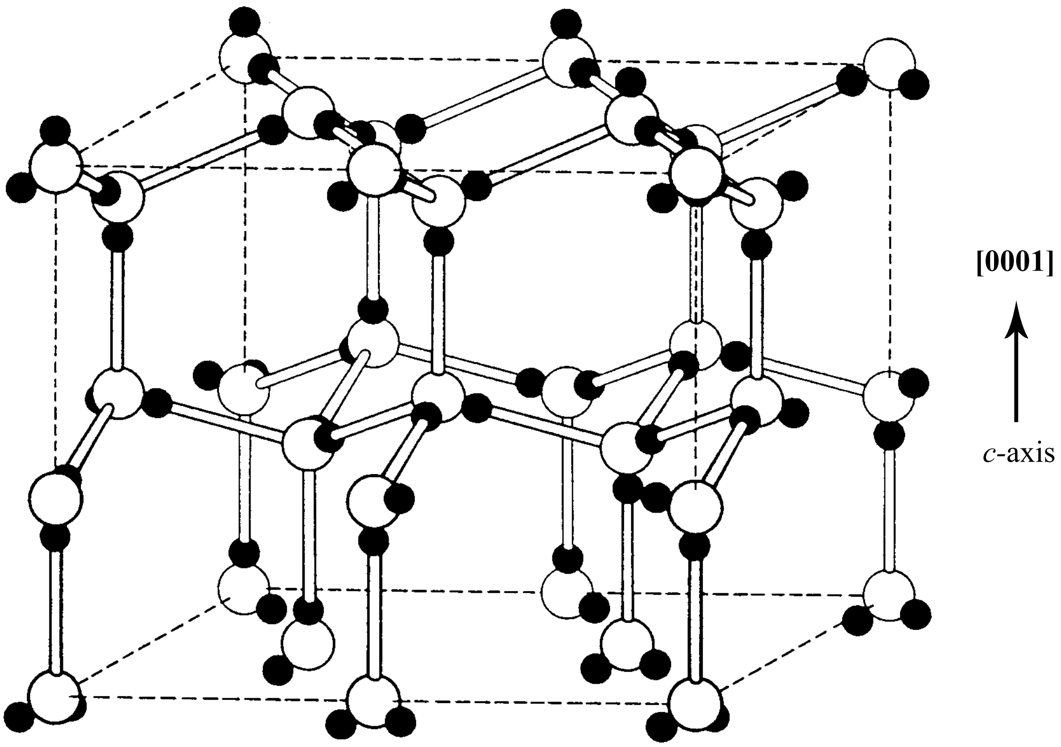

Figure 4: *The crystal structure of ice Ih. The white and the black circles represent the O and H atoms, respectively. The white lines represent the H-bonds.*

as c-axis or [1000] in the Miller-Bravais notation appropriate for hexagonal structures. Under most conditions crystal growth is more rapid in directions perpendicular to the c-axis.

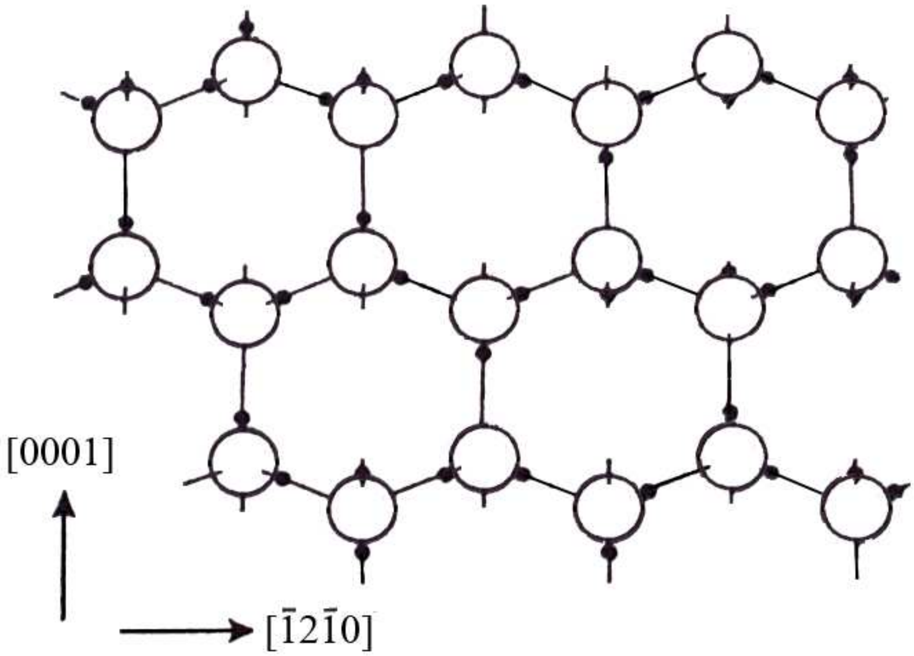

Figure 5: *A layer of the ice structure projected on the* ($10\bar{1}0$) *plane.*

When liquid, water freezes in such a way that the single crystals are nucleated initially, and these may be attached to the walls of the container or float on the surface. A few isolated nuclei form, lying on the surface with the c-axes vertical, and these grow across the surface and then downward, thus forming columnar grains whit their c-axis parallel. If ice is initially formed more rapidly, the surface is covered with a solid mass of randomly oriented grains and, as these spread into the liquid, the grains, which grow perpendicular to the c-axis, grow most rapidly and predominate over the others. As a result a sheet of ice growing from a free surface, as in a lake or at sea, will usually come to consist of long grains running perpendicular to the surface with their c-axis approximately horizontal.

For many experiments single crystals are required. Crystals of good quality can be cut from large-grained columnar ice [15]. At one time it was common to use large crystals which could be piked up from glaciers, Mendenhall Glacier in Alaska, as an example [16]. Single crystal can be formed in the laboratory simply by cooling an open vessel containing water under controlled conditions [17] [18], or much more quickly and stably if surface cooling is achieved by rapid evaporation from the surface under reduced pressure [19]. Single crystal have also been grown by variants of the Czochralski technique in which a cooled seed crystal is gradually lifted from the liquid held at 0 °C, but the highest quality crystals are produced by growing the ice through a capillary into a wider glass tube. The most stable conditions for growth are obtained when the ice forms above the liquid as in the Sapporo technique [20]. This method requires a seed crystal, and, because the expansion on freezing, it cannot be used with the water in a sealed container. These problems do not arise in the Birmingham technique where the ice grows from the bottom [21]. As the growth tube is lowered into the column of cold antifreeze, polycrystalline ice is first formed in the nucleation bulb, and the ice then grows as a single crystal through the twisted capillary into the main part of the tube. However, in this method the liquid is unstable against convection and the temperature distribution has to be carefully controlled to eliminate a gradient in the upper part of the tube.

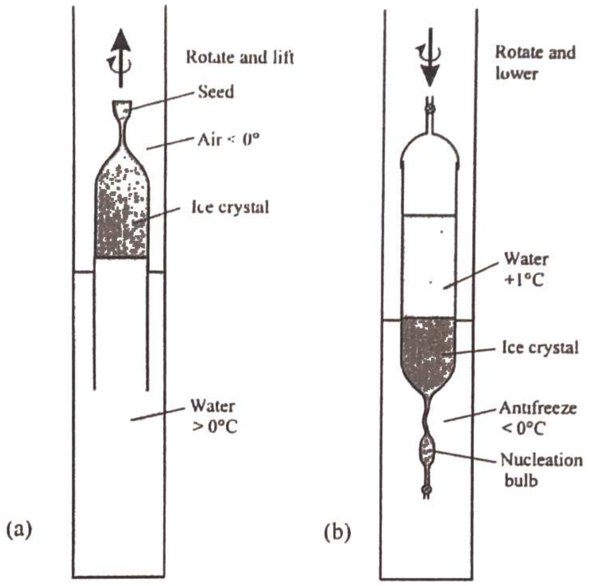

Figure 6: *System for the growth of high quality single crystal of ice. a) Sapporo technique in which the crystal is raised from the liquid; b) Birmingham technique in which the growth tube is lowered into cold antifreeze.*

Measurement of momentum distributions

Since the early development of X-ray Compton scattering, the realization that the target atom in the systems necessarily contains bound electrons, which cannot be stationary, led to the interpretation that Compton scattered beams were Doppler broadened due to the motion of the target electrons [22]. Du Mond (1929) used the novel Fermi-Dirac distribution function to predict the line shape for beryllium samples [23]. His results possibly constitute the earliest direct evidence for the validity of the Fermi-Dirac statistics for the electron gas. Thus, for target electrons possessing a probability density distribution $n(p)$, the Compton profile, $J(p_z)$, where z is the direction of the scattering vector, is the projection of $n(p)$ along the scattering vector.

In isotropic systems $n(p)$ depends only on the magnitude of p, and it can be shown that [24]:

$$J(p_z) = 2\pi \int_{|y|}^{\infty} pn(p)dp\,, \tag{1}$$

and hence that

$$n(p) = -\frac{1}{2\pi p_z}\frac{dJ(p_z)}{dp_z}\bigg|\, p_z = p\,. \tag{2}$$

The latter expression for the momentum distribution in terms of the derivative of the Compton profile is originally due to Du Mond [23].

The possibility of measuring momentum distribution of bounded atoms within the impulse approximation was proposed in 1964 by Ivanov e Sayasov [25]. Instead, a DINS experiment on monoatomic samples was proposed by Hohenberg and Platzmann in 1966 [26], to measure the mean kinetic energy of superfluid ^4He, to have a direct evidence of the Bose condensate. In their work they enhanced the possibility of interpreting the data in a simple way thanks to the Impulse Approximation (I.A.), that holds if the exchanged wave vector of the incoming neutrons is large enough. For this reason DINS had his major development in the eighties, when high flux epithermal neutrons sources (neutrons with an energy around 1 eV) became available.

The impulse approximation consists, in fact, in neglecting the internal binding energies of a sample and considering the interaction between an incoming neutron and a target nucleus as a two free particle scattering event. To reach this regime high exchanged energies (typically $E > 1\ eV$) and wave vector ($q > 30\ \AA^{-1}$) are needed.

Early studies were addressed to test the use of DINS as a method for directly observing the postulated Bose-Einstein condensate in superfluid ^4He [27, 28, 29, 30, 31]. The advent of pulsed neutron sources, with an high flux in the epithermal region, has made DINS experiments feasible [32, 33, 34, 35, 36]. As a result, over the last 20 years, a number of experiments of the neutron Compton profile have been successfully performed and the single-particle short-time dynamics has been studied in a large number of systems in a wide range of thermodynamic states. These include hydrogen bonded systems [37, 38], metal hydrides [39, 40, 41, 42], catalysts [43], glasses [44, 45], amorphous materials [46], quantum fluids and solids [46, 47, 48, 49, 50, 51, 52].

This technique is based on measurements that provide information on the system over very short spatial range ($r \leq 1$ Å) and very short time scale ($t \leq 10^{-15}s$). In this regard, it is not too difficult to understand how DINS relates the scattering cross section to the momentum distribution, whose variance is related to the mean kinetic energy of the target particle. As an example, let us imagine an ideal gas, made of non interacting monoatomic particles, with a Gaussian distribution of momenta and let us suppose to perform a DINS experiment on such a system. With the knowledge of all the neutrons kinematic variables before and after the scattering, it is possible to obtain the exchanged momentum and energy. In this case what is measured is a cross section that can be expressed as a delta function, representing the energy conservation, times a term that takes into account the velocity distribution of the target particles, leading to a Doppler broadening of the delta function. In other words it is possible to measure the momentum distribution of the system.

To better illustrate the strength of this technique it is useful to report some results obtained in the simple case of a monoatomic system, that has a remarkable interest for quantum mechanics: helium [53]. ^4He is very close to an ideal system because of its low mass and the accurate knowledge of his interatomic interactions. It is well known that at a temperature of $T_\lambda = 2.17$ K ^4He undergoes a transition signaled by a specific heat anomaly, whose characteristic shape has led to the name λ point being given to the temperature at which it occurs. This temperature marks the transition between two different forms of liquid ^4He. Above the lambda point, helium behaves like a low-viscosity low-density liquid. Below the transition temperature helium is capable of being viscous and nonviscous at the same time, a contradiction which is the essence of the *two-fluid model* [54].

According to this model, helium in the superfluid phase behaves as if it were a mixture of two liquids: one, the normal fluid, possessing an ordinary viscosity, and the other, the superfluid, being capable of frictionless flow, passing obstacles and flowing through narrow channels. In the Andronikashvili experiment performed in 1946 [55] a pile of equally spaced thin metal discs were suspended by a torsion fiber in order to be able to perform oscillations in liquid helium. It confirmed the prediction that the superfluid fraction would have no effect on the torsion pendulum and it showed that helium is almost entirely superfluid below 1 K. In 1938 London suggested that the lambda point marked the onset of a Bose-Einstein condensation. The condensate was associated with the superfluid fraction of helium below the lambda point, while the normal component corresponds to the elementary (thermal) excitations of the whole system. Miller [56] pointed out that inelastic neutron scattering measurements, with high exchanged wave vector, would allow a derivation of $\frac{N_0}{N}$, the relative number of particles in the condensed state. Following the Honemberg and Platzmann idea, the first experimental results, in the high q regime, were obtained by Cowley and Woods [57], using rotating crystals and triple axis spectrometers with wave vector transfers extending up to 10 $\AA^{-1}$. Their results provided the first experimental estimate of the condensate component: (17 ± 10) % at finite temperature (1.1 K).

With the advent of spallation neutron sources, large fluxes of neutrons in excess of 1 *eV* became available, allowing measurements at larger wave vector transfer, where data interpretation can be more easily described in terms of the IA framework. Two types of neutron spectrometers [58] were used with this aim, both employing the time-of-flight technique:

- the direct-geometry chopper spectrometers, allowing measurements with wave vector transfers up to about 30 $\AA^{-1}$;
- inverse-geometry filter-resonance spectrometers where the wave vector transfer extends up to 250 $\AA^{-1}$ [59].

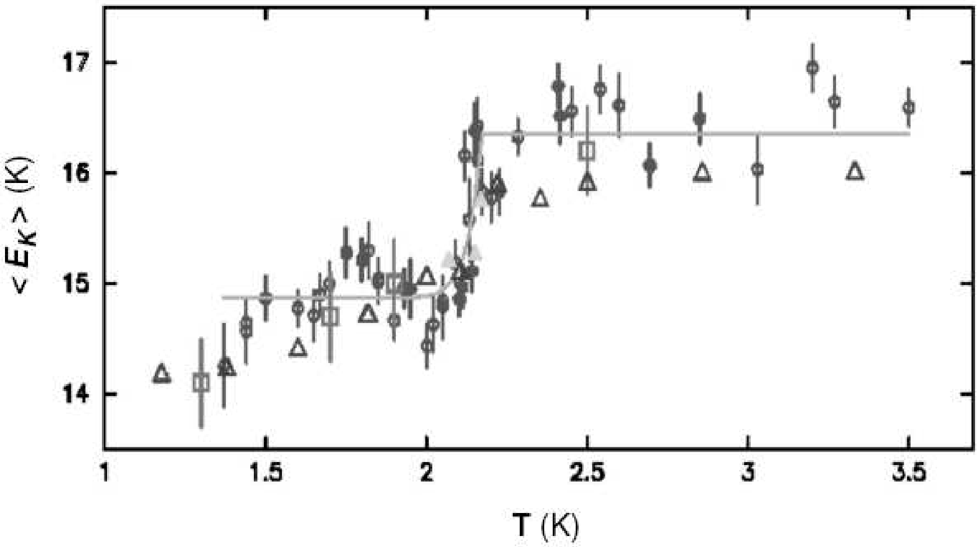

Figure 7: *Mean kinetic energy of ^4He as a function of the temperature, around the transition temperature. Square [60] and circles [61] are obtained by measurements carried on VESUVIO spectrometer at ISIS neutron spallation source, one of the spectrometer used in this work. Triangles refer to Monte Carlo simulation [62]. The step at T= 2.17 K indicates the transition between the superfluid and the normal phase.*

These measurements yield to a condensate fraction $f = 0.088 \pm 0.003$ [61], in very good agreement with more recent results [63].

The first experimental study of the density and temperature dependence of the momentum distribution in the superfluid phase (T =1.5 K) for low exchanged wave vector (range from 5 to 7 $\AA^{-1}$) was performed by Mook [66]. However, this experiment was not exhaustive, because

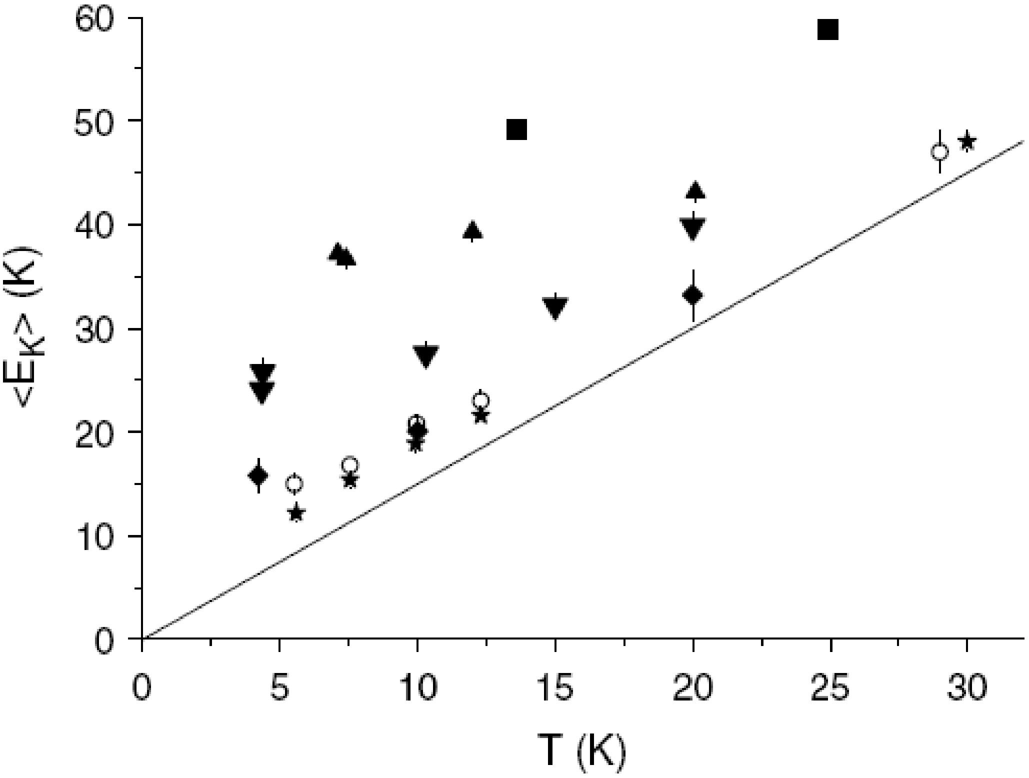

Figure 8: *Measurements of the liquid* ^4He *mean kinetic energy at some temperatures and densities. [46, 64, 65] Equal symbols correspond to equal density:* $n = 44.7\ nm^{-3}$ *(squares),* $n = 37.9\ nm^{-3}$ *(high vertex triangles),* $n = 33.1\ nm^{-3}$ *(low vertex triangles),* $n = 22.5\ nm^{-3}$ *(rombs),* $n = 13.8\ nm^{-3}$ *(circles),* $n = 10.4 nm^{-3}$ *(stars); the line represents the classical behavior. Larger density gives rise to a larger excess of mean kinetic energy.*

the density behavior of the $n(p)$ was analyzed in terms of the changes of the condensate fraction only, neglecting the important localization effects induced by the reduction of the molar volume. In this respect the work by Herwig [67], simplified the scenario measuring the ^4He in the normal phase. Their results assessed an almost quadratic density dependence of $\langle E_k \rangle$, in good agreement with path integral Monte Carlo theoretical predictions [68]. Systematic studies of liquids ^4He have been undertaken on the MARI spectrometer at ISIS, up to a wave vector transfer of the order of 25 $\mathring{A}^{-1}$. These employed a new analysis technique, which simultaneously determined the momentum distribution and the final-state effects [69]: single-particle momentum distributions of normal liquid ^4He and superfluid ^4He have been investigated in this way [70, 71, 72]. A detailed review of these measurements is provided in the book of H. R. Glyde [73], and in Ref. [74].

In figure 8 one can compare the mean kinetic energy, with the same quantity calculated within the classical theory: $\langle E_k \rangle = 3/2 k_b T$. An excess of mean kinetic energy due to quantum effects is visible and this excess increase for higher densities [61, 60, 62]. A similar relation between mean kinetic energy and density has been also observed for ^3He, a system which represents an almost ideal Fermi liquid (o solid), as well the unique available in nature. No measures on ^3He has been done in solid phase before 2001, except for some neutron diffraction experiments, due to its high neutron capture cross section for thermal neutrons. Thanks to the DINS technique, in 2001 the mean kinetic energy was measured [75] in a high density liquid phase and in two densities solid state, with two different crystalline structures and molar volumes, $\nu = 18.75\ cm^3/mole$, for fcc structure and $\nu = 20.1\ cm^3/mole$ for bcc.

Figure 9 shows that experimental data are in a good agreement with simulation [76] and $\langle E_k \rangle$ increase with density. In very general terms one can state that this correlation is a direct consequence of the Heisenberg principle: if the volume in which a particle can move is decreased, then the spatial extension of his wave function is decreased too, so the fluctuation of the wave function in momentum space increases and this gives rise to a higher mean kinetic energy.

It has to be stressed how DINS is sensitive to the atomic masses of the sample and allows us to distinguish among the contribution of different isotopes. In figure 10 a spectrum from a DINS experiment on a mixture of ^3He and ^4He is reported. ^3He and ^4He peaks are well separated, as well as the aluminum peak due the container. From these measures it is possible to conduct an independent analysis on the contribution of these two isotopes. This feature makes DINS very effective for the study of many molecular systems in which isolating the contribution of different atomic masses is desirable [53]. In the case of water, hydrogen has a mass that is at least 16 times smaller than the mass of oxygen and of the material of the container, so the hydrogen peak is well separated from the other peaks. Also

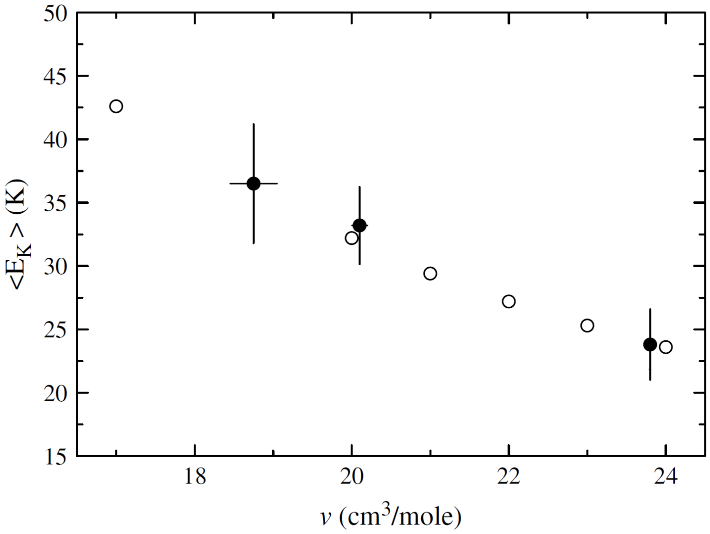

Figure 9: *Mean kinetic energy as a function of the molar volume: black circles represent experimental value, white circles are DMC (Diffusion Monte Carlo) [76]. The temperature is kept fixed: the kinetic energy increases as the molar volume is decreased, showing a direct correlation between* $\langle E_k \rangle$ *and the density.*

the cross section of hydrogen is four time larger than other elements so the DINS is the best experimental technique for studying the momentum distribution of hydrogen in many systems.

Momentum distribution is sensitive to the local environment of the particles (the proton in case of water) and this is because the position and momentum operators do not commute. The equilibrium position of a proton, corresponding to the minimum of the potential in which the particle stays, can be measured, for example, by diffraction. The knowledge of the momentum distribution, however, can reveal what kind of potential the proton feels around its equilibrium position. For example, a proton in an harmonic potential has a Gaussian momentum distribution. In general the extraction of the potential from the momentum distribution is simply obtained by inverting the Schroedinger equation [77]:

$$V(\vec{R}) - E = \frac{\hbar^2}{2M}\Psi^{-1}\nabla^2\Psi\,, \tag{3}$$

where $\Psi(R)$ and $\Psi(p)$ are Fourier transforms of each other, and the latter is obtained from $|\Psi(p)|^2 = n(p)$. The phase ambiguity in extracting the momentum-space wave function from $n(p)$ is not a problem for inversion-symmetric potentials, since $\Psi(p)$ can always be chosen to be real. It should be noted that the technique, at least in its simplest form, is restricted to systems in which all atoms of the species under study have identical chemical environments.

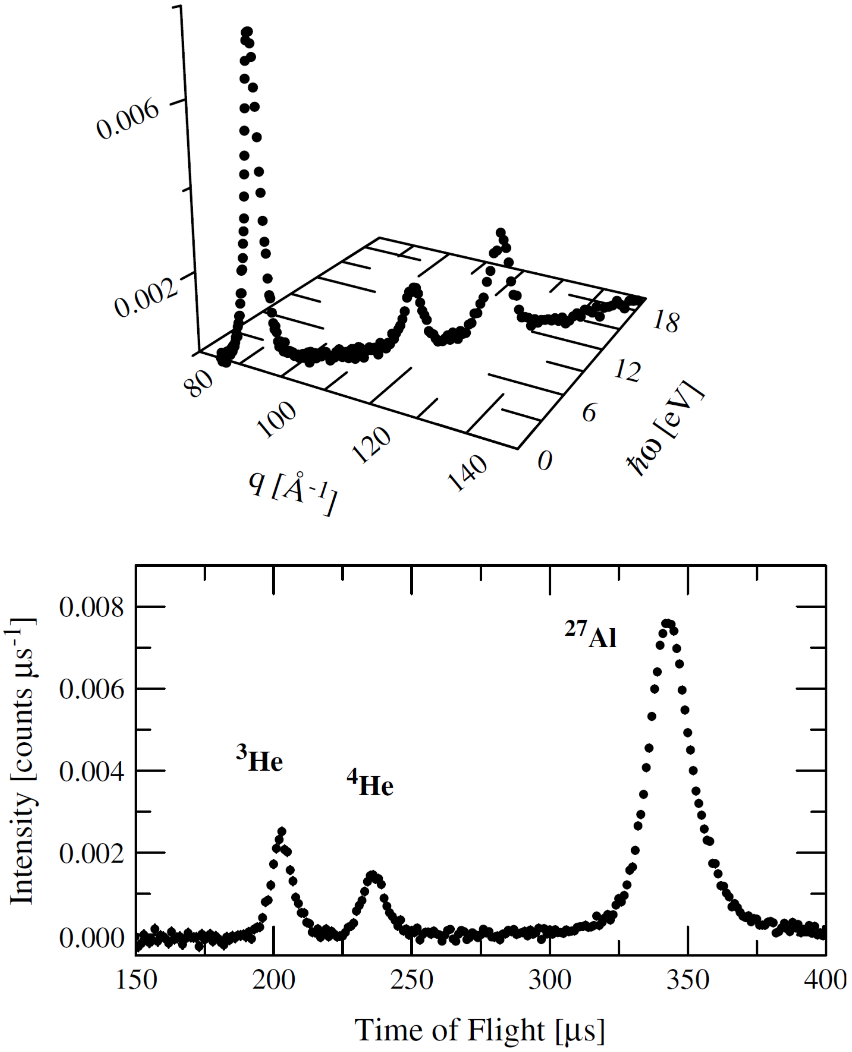

Figure 10: *DINS experiment performed on a sample made by a mixture of* ^4He *with 35% of* ^3He. *The response of a detector placed at* $\theta = 78°$ *with respect to the incoming neutrons is shown for energy and exchanged wave vector spectrum (upper panel) and TOF spectrum (lower panel), showing the clear separation among the recoil peaks of the different atomic masses.*

If they do not, the Compton profile will be a superposition of contributions from different environments. Although the spatial wave function can be obtained from momentum distribution, there is a very important difference between DINS and diffraction in the sampled time scales: diffraction gives informations of the spatial distribution over a long time, while momentum distribution sample very short time scale. For this reason one can distinguish with a DINS experiment a coherent proton tunneling from an induced thermal jump [78].

An extreme case of an anharmonic potential is one with two minima, such as might be expected for a proton in a hydrogen bond [79, 80]. A useful model for illustrating the results expected for a double-well potential is to assume a ground state consisting of two shifted Gaussian of equal amplitude in one dimension:

$$\Psi(x) = e^{-\frac{(x-a)^2}{2\sigma}} + e^{-\frac{(x-a)^2}{2\sigma}}. \tag{4}$$

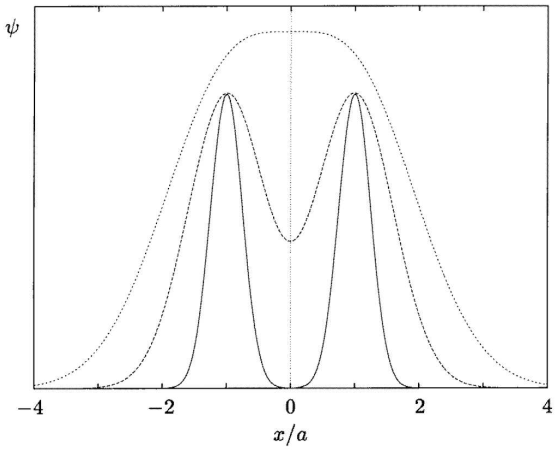

Figure 11: *Model wave functions for an atom in a double-well potential as defined in the equation 4. The wave function is the sum of two Gaussian components of width σ, centered a distance 2a apart. Solid line: a/σ = 0.25; dashed line: a/σ= 0.6; dotted line: a/σ = 1. As the width of the two Gaussian component enlarges or, equivalently, the distance 2a decreases, the wave function tends to a Gaussian function. As a consequence the measured momentum distribution could be indistinguishable from a Gaussian function. As an example the wave function with a/σ = 1 would give a momentum distribution resembling a Gaussian with larger tails, as in the case of water around the maximum density temperature [81]. Instead, the peculiar behavior of the supercooled water, reported in figure 14, can be associated to a wave function with a clear separation between its two maxima.*

This function is plotted in figure 11 for selected values of the ratio a/σ. For the largest value of a/σ the potential consists of rather isolated harmonic wells, which gradually merge

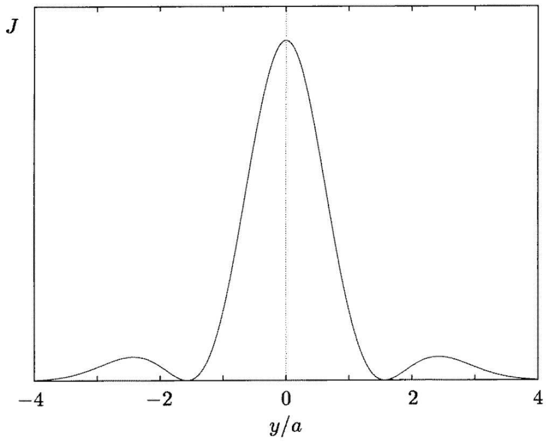

Figure 12: *The Neutron Compton Profile, $J(y)$, corresponding to the two-Gaussian model wave function, with $a/\sigma = 0.6$.*

as a/σ is reduced. For $a \leq \sigma$, the potential is more accurately described as a single harmonic well with a shallow *bump* in the center, and the wave function is a single non-Gaussian peak.

The Compton profile, $J(y) = e^{-\sigma^2 y^2} \cos^2 ay$, is plotted in figure 12 for an intermediate value a/σ. It includes an oscillatory factor, representing interference between wave functions localized in the two wells, and the overall shape is far from Gaussian. The number of oscillations in each half-width of the Gaussian envelope is roughly a/σ, so for weak anisotropy ($a/\sigma \leq 1$) the deviations from Gaussian form are less pronounced. This simple model may be extended to the case where the double-well potential, as in a typical hydrogen bond, is not symmetric. It is found that the asymmetry suppresses somewhat the oscillatory component in the wings of the Compton profile, which no longer goes to zero at its minima.

Previous studies on water samples in various thermodynamical conditions, ice, supercooled and supercritical water, depict a remarkable and anomalous variation of the $n(p)$, especially when water is supercooled. The mean kinetic energy in this case is found to be much higher with respect to ice at the same temperature [82].

Another recent study [81] investigated the possibility that an increase on the density could also give an increase of $\langle E_k \rangle$. In that study a DINS experiment where performed on the VESUVIO spectrometer for temperatures at about the maximum density of the water ($\approx$ 277 K). The results are reported in figure 13. This figure shows the temperature dependence of proton's $\langle E_k \rangle$ measured in both stable and metastable phases of bulk water in the temperature range from 269 to 300 K, along with the calculated $\langle E_k \rangle$, E_c. The temperature dependence of E_c in the stable water phase, shown in figure 13 as a thin solid line, has been derived in Ref. [83]. The calculation takes into account the optical vibrational frequencies of ice and water in different phases, available in the literature, assuming the harmonic approximation and the decoupling between the degrees of freedom of translation, rotation (libration), and internal vibrations.

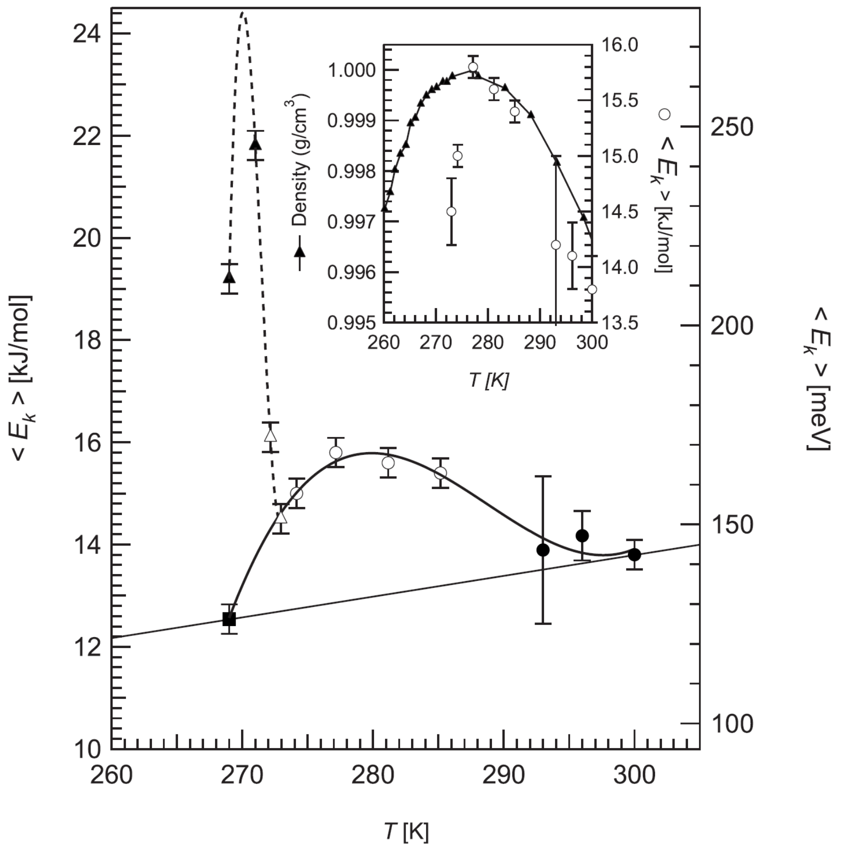

Figure 13: *Water proton mean kinetic energy* $\langle E_k \rangle$ *as a function of temperature for supercooled water (triangles) [82], stable water (circles) [81], ice (square) [84]. The data above 293 K for liquid stable water are from Ref. [85]. The thin solid line corresponds to the calculated* $\langle E_k \rangle$ *[86]. The solid and dashed lines are guides for the eye. In the inset,* $\langle E_k \rangle$ *data in the stable liquid phase (circles and right axis) are reported in comparison with the density of water (line plus solid triangles and left axis) as a function of temperature.*

While data for water [87] above 293 K, including supercritical states, are satisfactorily described by the E_c behavior, data around the temperature of maximum density and in the supercooled phase show an excess of proton mean kinetic energy. Data could confirm the original hypothesis of the possible link between the anomalous temperature dependence of water density and the temperature dependence of $\langle E_k \rangle$, as it has already been observed in helium [64, 88], but not in the whole temperature range. Indeed, and in contrast with earlier report, [82] $\langle E_k \rangle$ shows two maxima instead of one: the first at 277 K and the other in the supercooled phase in the range of 269-271 K, with an excess of $\langle E_k \rangle$ of about 3 kJ/mol (30 meV) and 12 kJ/mol (120 meV), respectively, with respect to E_c.

The peculiar temperature dependence of $\langle E_k \rangle$, suggests that two distinct mechanisms may be considered below and above the melting temperature. As a matter of fact the excess of $\langle E_k \rangle$ in the stable water phase is moderate and its temperature dependence follows that of density, showing a maximum at the same temperature (see inset in figure 13). A correlation between density and $\langle E_k \rangle$, as measured by DINS, has already been observed in helium and explained in that case by using a harmonic model for the fluid. The anomaly of $\langle E_k \rangle$ versus T above 273 K may be explained as a further evidence for water structural anomalies, which manifest through the existence of a maximum of density and transport properties in the stable water phase [89]. Within this hypothesis the maximum of $\langle E_k \rangle$ at 277 K, shown in figure 13, may be an indirect manifestation of the competition between zero point energy, E_0, and thermal fluctuations, which has been proposed as the quantum origin of the density maximum [90]. We notice, however, that quantum effects are not necessarily required to explain the existence of a maximum of density in water [91].

On the other hand the huge increase of $\langle E_k \rangle$ in the metastable state of water could be directly related to the likely delocalization of protons along the H-bond, as shown by the shape of the radial proton momentum distribution $4\pi p^2 n(p)$ of figure 14.

The radial momentum distribution of the proton measured below 273 K shows a peak at low-p ($\approx$7 $\AA^{-1}$), and a shoulder at high-p ($\approx$17 $\AA^{-1}$), indicating a delocalization of the proton over a distance $\Delta d = 2\pi \ /\Delta p) \approx 0.6\,\AA$ from the equilibrium position. The presence of a shoulder at high p in the radial momentum distribution could, indeed, be ascribed to the coherent delocalization of the protons over two sites of a double well potential [79] felt by the proton along the H-bond direction between two water molecules. We notice that $\langle E_k \rangle$ in the supercooled phase is comparable with the H-bond energy ($\approx$ 20 kJ/mol) and Δd is compatible with the width of the fluctuations of the H-bond length (width of the first intermolecular peak of the oxygen-hydrogen radial distribution function) and the oxygen-oxygen distance in supercooled water [92, 93].

Vibrational Neutron Spectroscopy

Vibrational spectroscopy with neutrons is a spectroscopic technique in which the neutron is used to probe the dynamics of atoms and molecules in solids. The most common methods for studying molecular vibrations are the well established optical techniques of infrared (IF)

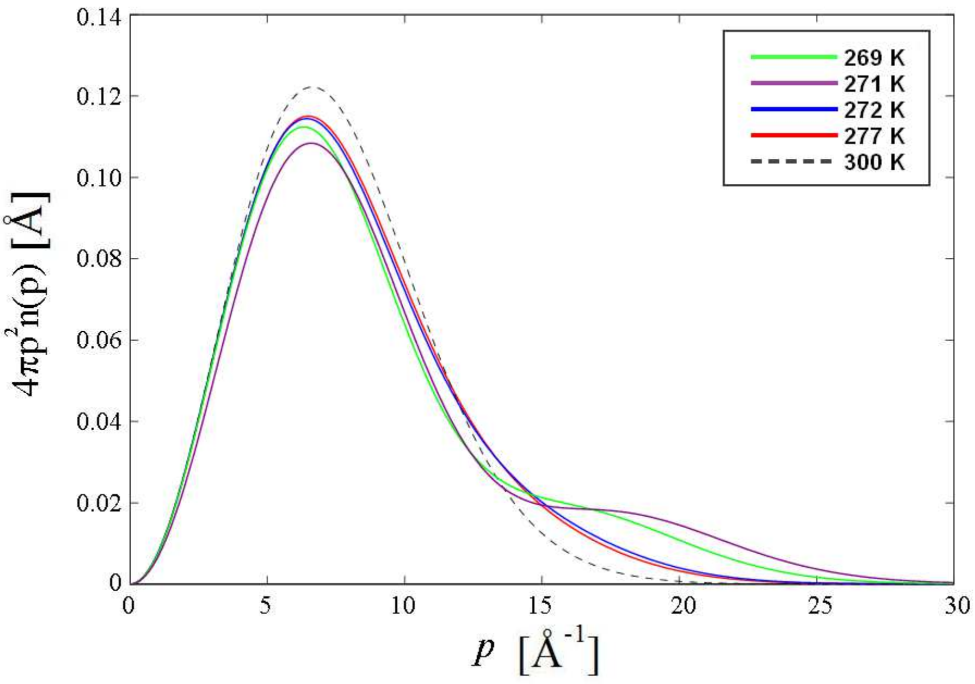

Figure 14: *Radial proton momentum distribution for water in different phases: supercooled water [82] and stable water [81]. The different behavior of the momentum distributions at different temperatures is remarkable. The dotted line is the momentum distribution of the water at room temperature and it is a Gaussian function. The momentum distribution of water above 0 °C and close to the maximum density temperature (4 °C) has a clear larger tail. In the supercooled phase a secondary maximum appears. This effect can be explained with the proton in a double well potential.*

and Raman spectroscopy (RS) [94].

Regarding our work, the main difference between optical spectroscopy and INS is that the latter is very sensitive to hydrogen atom vibrations, while Raman or infrared spectroscopy is mostly sensitive to heavier atoms because of the number of their electrons. Neutron incoherent cross section of hydrogen is instead uniquely high, making hydrogen ten times more visible than any other atom. Measured INS spectra are straightforwardly related to the atomic displacements of the scattering atom, which can be often obtained from simple classical dynamics. Any complication arising from electro-optical parameters are avoided: as an example optical selection rules are not accounted for in an INS spectra where all vibration are active, and in principle measurable. Therefore some peaks that are visible with neutron spectroscopy vanish in Raman or infrared spectra.

The band positions and intensities of most molecular system can be accurately calculated using modern *ab initio* computational methods. This is especially valuable since these methods are a well established part of the modern approach to understand molecular structure and dynamics.

INS spectrometers cover the whole molecular vibrational range (16-4000 cm^{-1}). The lower energy range (below 400 cm^{-1}) is readily accessible, whereas difficult to reach for the IR and Raman spectroscopies. With modern instrumentation, like the SEQUOIA spectrometer at SNS, the quality of INS spectra approaches that of infrared and Raman spectra obtained from the same system in the same condition.

In an INS experiment we observe how the intensities of neutron scattering varies with the energy transfer and momentum transfer. The spectrum is in neutron energy loss, where energy is transferred from the incident neutrons to the scattering atoms.

The atoms are embedded in the molecule and can only gain or loss energy in the vibrational quanta characterized by the molecular structure. Thus INS gives an easy and direct access to the knowledge of the vibrational spectrum of a molecule. Furthermore many other physical quantities can be calculated from neutron vibrational spectra, such as the density of vibrational state (DOS) as we will describe in the chapter 5.

The first extensive study about the vibrational spectrum of water and ice, with an incident energy larger than the excitation of the stretching mode (around 420 meV), was done by Harling in 1969 [95], at T = 268 K for ice and T = 299 K for water. The experiment was carried out with a monochromatic neutron beam, coupled with a TOF spectrometer, or analyzer. In that experiment, the neutron incident energies was set at three values $\approx$ 150, 300 and 600 meV, with an energy resolution of 21 meV, for the 600 meV energy value. As we will see in chapter 2 the resolution of the actual experiment carried on the SEQUOIA spectrometer is improved by at least a factor 2. Each value of the neutron incident energy allow us to distinguish among the different vibrations, that is rotation, libration and stretching.

In figure 15 and 16 the vibrational spectrum of water measured by Harling is shown. In his work he introduced new variables α and β, instead of E or ω and $\vec{q}$. These variables are related to the usual variables in the following way:

$$\begin{cases} \alpha = \frac{\vec{q}}{mk_BT} \\ \beta = \frac{E_1 - E_0}{k_BT}, \end{cases} \tag{5}$$

where $\vec{q}$ is the exchanged wave vector, E_0 is the incident energy and E_1 is the neutron energy after the scattering. In the figures 15 and 16, the triangles represent the energy resolution. The spectrum recorded at 15° shows a peculiar line shape which is attributed to several contributions related to the symmetric and asymmetric stretching modes. The structure observed is considerably wider than the spectrometer resolution and it is therefore not significantly distorted by instrumental resolution. In figure 15 the cross section of the water at 15° exhibits a double peak structure with maxima at about 450 and 530 meV.

The assignments done by Harling of the spectra shown in fiures 15 and 16, are summarized in table 1.

T [K]	E_l [meV]	ΔE_l [meV]	E_b [meV]	ΔE_b [meV]	E_s [meV]	ΔE_s [meV]
299	≈ 64		206	23	≈ 450 ≈ 530	
268	88	≈ 58	206	≈ 41	≈ 427 ≈ 485 ≈ 531	≈ 79

Table 1: *Energies of the vibrational modes in ice and water measured by Harling [95] and shown in figures 15 and 16. E_l, E_b and E_s represent libration, bending and stretching energies respectively.*

The energy values shown in table 1 are larger than other recent results obtained both with neutron spectroscopy [96] both with optical spectroscopy (see for example Ref. [97]). The discrepancy could be attributed to the lack of data reduction and correction for the multiple scattering.

A more accurate result for ice Ih can be found in Ref. [96], were instead a correction of the data from multiple scattering were done. In that work an Ih ice sample was measured with an incident energy of ≈ 600 meV. This work was entirely devoted to the measure of the vibrational density of states at T = 20 K, in order to reduce contribution from multiphonon and to the effects due to the Debye-Waller factor. The data were collected at small scattering angles to minimize the momentum transfer and obtain a more accurate DOS.

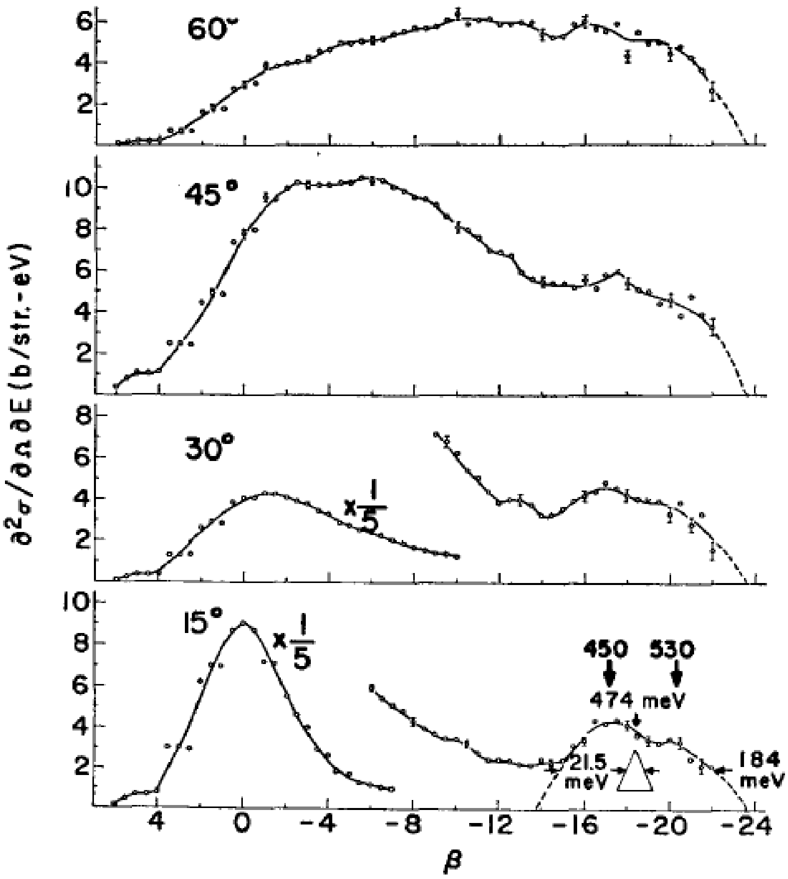

Figure 15: *Double differential scattering cross sections for water with initial energy 608 meV [95] for different detection angles. In the lower plot, the arrows indicate the peaks associated to the stretching mode (E ≈ 450) and to a secondary peak due to the combination of the stretching mode with another mode (probably libration mode) (E ≈ 530). The triangle is an estimation of the width of the peak associated to the stretching.*

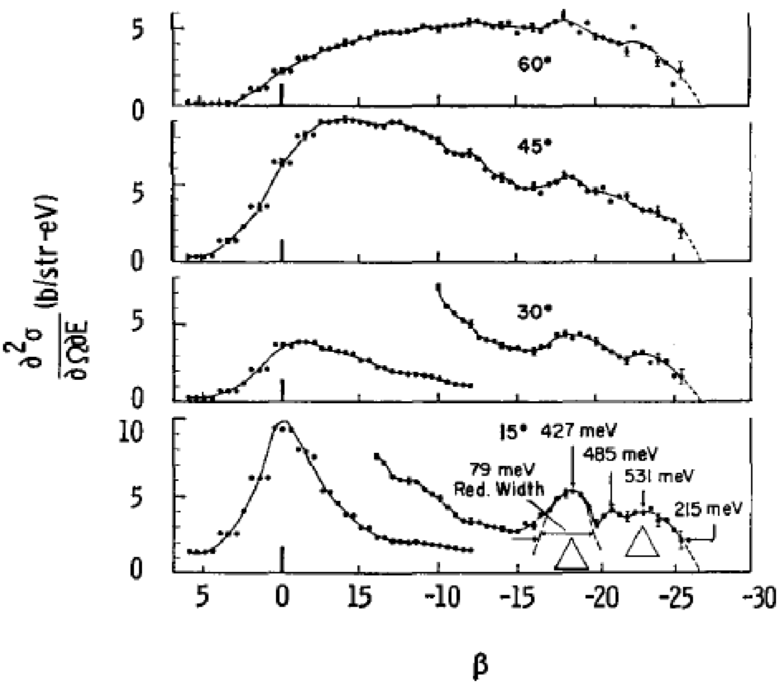

Figure 16: *Double differential cross sections for ice with initial energy 616 meV [95]. In the lower plot, the lines indicate the peaks associated to the stretching mode ($E \approx 427$) and to a secondary peak due to the combination of the stretching mode with another mode ($E \approx 485$), appearing at lower energy with respect the liquid water. The triangles are an estimation of the width of these two peaks. Another peak arises in the case of ice at $E \approx 531$.*

Data were obtained in absolute scattering function by means of standard background subtraction and normalization from the scattered intensities of the sample, empty container and vanadium calibration [98].

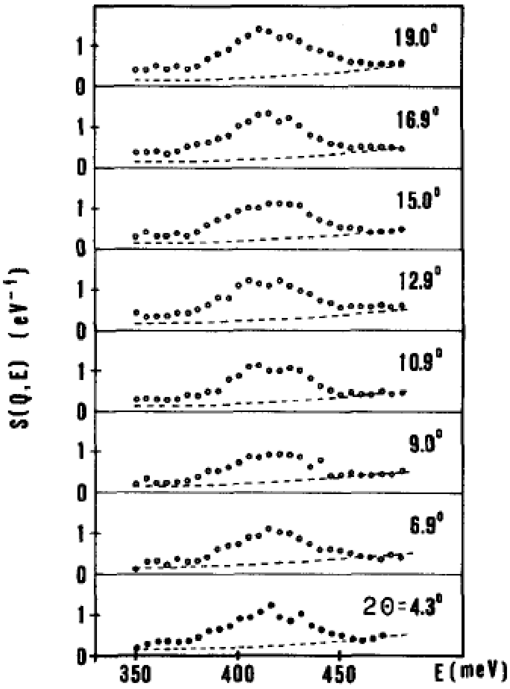

Figure 17: *Scattering function $S(\vec{Q}, E)$ at various scattering angles from [96]. The center of the peak, associated to the stretching mode appears at a lower energy with respect to the Harling measurement. Dashed line is the evaluation of the multiple scattering.*

In figure 17 the dynamical structure factor, also named in the literature scattering function, is reported for various angles. The dashed line represents the multiple scattering evaluation with a phenomenological model that we will use in our INS experiment. That model, described by authors in a subsequent work [99], consists in considering the multiple scattering as a double scattering process (thus neglecting higher scattering orders) in which a double scattered neutron undergoes two subsequent 90° scattering events. At this angle $\vec{q}$ is so large that we can consider the scattering being dominated by single scattering events. The double scattering process is thus a self convolution of the scattering function at 90° and it is well represented by:

$$S(E) = Ae^{-b(E-E_0)^2}, \tag{6}$$

where E_0 is the incident energy. In this framework the sample is treated as an infinite slab, with which it is possible to calculate the fraction of multiple scattering [100], whose calculated value is about 28%.

Once the data reduction done, the INS allows the extraction of the vibrational DOS as reported in figure 18 for the energy range associated to the stretching vibrational mode.

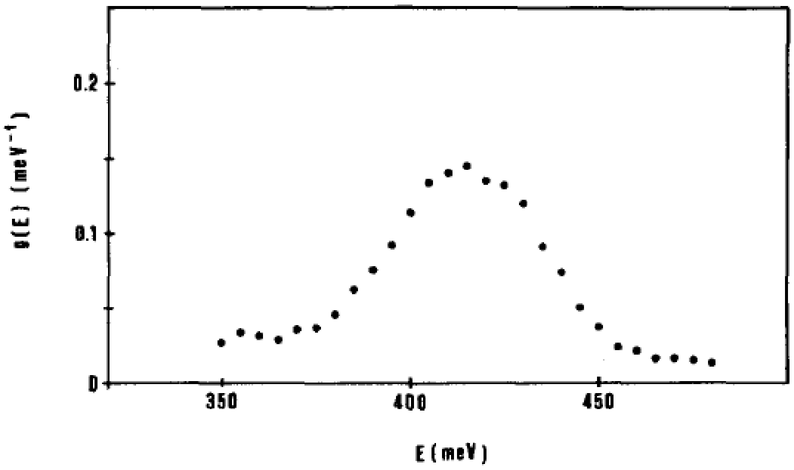

Figure 18: *Density of vibrational states of ice Ih, derived by Andreani [96], in the energy range of the stretching mode.*

Accurate measurements of the DOS in the stretching energy region are very important to check the reliability of theoretical predictions. In a recent work [101] this quantity has been evaluated by means of PICPMD (Path Integral Car Parrinello Molecular Dynamics) that represents nowadays the most accurate simulation method to calculate the dynamical behavior of the proton. However this simulation underestimates the stretching energy, giving a value of $\approx$ 3000 cm^{-1}, corresponding to 375 meV, very far from 417 meV of the work of Andreani [96], even for a relative simple system like ice Ih.

The experiments

Three experiments have been performed in water and ice under various conditions. Two of them are DINS experiments, with a samples of polycrystalline ice Ih and monocrystalline oriented ice at 271 K and 130 K at fixed temperature, respectively. These two experiments have been performed at VESUVIO spectrometer at the ISIS spallation neutron source (UK). The third experiment is an INS experiment performed on water in a range of temperature from supercooled region (269 K) to room temperature and ice at T = 271 K. This experiment has been performed at the SEQUOIA spectrometer at SNS in the ORNL, Tennessee (USA).

DINS on ice

Although the behavior of $\langle E_k \rangle$ or $n(p)$ as a function of the temperature has been measured in recent years and despite many theoretical effort nobody had been able to explain and reproduce the behavior of water.

In the case of ice Ih, things seems to go better thanks to the fact that ice is an ordered system, and ice disorder seems to have small contribution to the simulated momentum distribution.

As stated above, momentum distribution is a physical quantity that is sensitive to the environment of the protons, so in principle one can extract informations on the potential felt by the protons. However, DINS only allows us to access to a spherically averaged momentum distribution and the usual DINS data analysis [53] does not provide any attempt to obtain directional information.

Another limit of the DINS is the discrimination between two effects that certainly alter the momentum distribution with respect an ideal 3-dimensional harmonic oscillator: the anisotropy and the anharmonicity of the proton potential. As an example the second feature in the momentum distribution of supercooled water [82] and confined water [102] was attributed to quantum tunneling between the two wells of an anharmonic one-dimensional potential. It is not clear, however, to what extent the dynamics of an interacting many-body system can be reduced to that of a single proton along a bond. For instance, it has been pointed out that anisotropy can mimic features of a spherical distribution that one might associate to anharmonicity in a 1D model, [103] and yet so far there has been no conclusive study of this issue.

To interpret experiments in confined and supercooled water, the unknown details of the molecular structure are a severe source of difficulty. However, even in the simpler case of ice Ih, it is not clear whether the full understanding of the physic could be achieved by simple model potentials, and how anharmonicity, anisotropy, and structural disorder influence the momentum distribution.

The discrimination between these two effects could in principle be obtained in two ways by DINS:

- making an experiment with very good statistics;
- making an experiment with a controlled and known geometry.

In the first case the statistics on data should be good enough to discriminate between a different model of parametrization of the momentum distribution, in which we reconstruct the $n(p)$ following a physical model consisting in a product of three harmonic momentum distributions.

This is the case of the first DINS experiment. Once allocated 5 days of beamtime at the ISIS spallation source, we planned to measure ice Ih at only one temperature slightly below the freezing point: T = 271 K. This value of the temperature has been chosen in order to have a direct comparison with the supercooled water at the same temperature. This is because the supercooled water exhibits a peculiar momentum distribution, see figure 14 and shows the absolute maximum of $\langle E_k \rangle$ as a function of the temperature among the whole set of thermodynamical point that have been measured.

The momentum distribution and the $\langle E_k \rangle$ of ice was already measured at T = 269 K [84] at the VESUVIO spectrometer in 2004. The authors found an energy ($\approx 130\ meV$) in accordance with the semi-classical behavior reported in figure 13. However, this value should not be considered reliable due to the lack of data reduction [104]. The result of the present measurement will confirm this hypothesis.

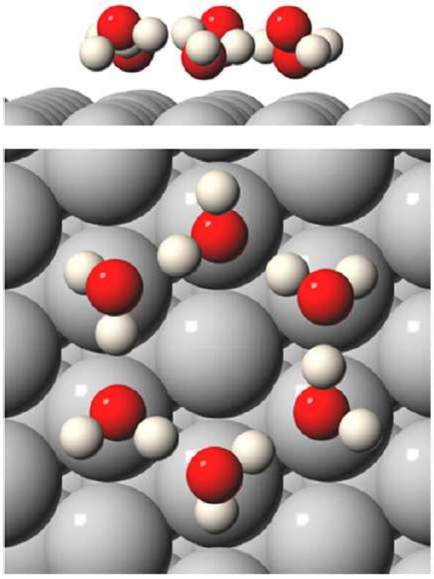

Figure 19: *Symmetric water hexamer adsorbed on Pt(111) showing the 0.7 Å vertical buckling of the O atoms of water. Adapted from the data of Ref. [105].*

In the second case we want to sample the momentum distribution only along particular directions. The sample is an ice film grown on a Pt (111) surface substrate. The ice film was obtained by adsorbing water vapor on Pt(111) at 130 K [106, 107, 108]. During the deposition the water reconstructs first layer, forming an incommensurate bulk ice (0001) film, oriented to the metal surface. Multilayer clusters coexist with the first layer and do not cover the surface until the film is more than ≈ 50 layers thick. Cluster growth is limited by nucleation of new layers. Growth of thick films proceeds rapidly at screw dislocations to form cubic ice [109]. To perform a neutron spectroscopy the thickness of the film should be macroscopic, so all the properties that arise from the interaction of the ice film with its substrate are negligible with respect to that of the bulk ice.

Cubic ice, denoted as ice Ic, is a metastable variant of Ice Ih in which the Oxygen atoms are arranged in the cubic structure of a diamond rather than on the hexagonal lattice of ice Ih. Every molecule forms four hydrogen bonds with its nearest neighbors as in ice Ih, and the densities are virtually identical, but if the (0001) layers of ice Ih are stacked in the sequence denoted by ABABAB..., cubic ice has the stacking sequence ABCABC... The relation between these two structures is the same as that between Face Centered Cubic (FCC) and Hexagonal Close Packing in metals (HCP). In general ice Ih is formed at T = 150 K, and cubic ice between 130 and 150 K.

The second DINS experiment was then carried out at T = 130 K. As we will explain in chapter 4 the directional information will be extracted by selecting DINS data at constant q values. As the value of q increases the momentum distribution is sampled in the direction of the c-axis, analogous to the c-axis of the ice Ih and corresponds to crystal growth direction.

INS in water and ice

The third experiment described in this work has been carried out by the INS technique. The sample is pure water at various temperatures and phases reported in table 2.

The supercooled water is obtained thanks to an Aluminum can with an internal Teflon coating that prevents the transition of water into ice for temperatures slightly below the freezing point. A polycrystalline ice was also measured at T = 271 K. Ice was obtained by cooling down water inside the can and waiting for the transition, that is clearly marked by a sudden increase in the temperature due to the release of heat during the transition. The incident energy was fixed to $E_0 = 800\ meV$.

The aim of this experiment is to track the behavior of the vibrational spectrum as a function of the temperature, searching for hints which that could help us to explain the anomalous behavior of the mean kinetic energy of water in this temperature range.

The anomalous structures appearing in the momentum distribution of the supercooled water are supposed to originate from the modification of the shape of the potential along the H-bonds, that could allow a coherent tunnelling of the proton between two minima of a double well potential. So the increase of the proton mean kinetic energy is reflected in the behavior of the potential along H-bond in all the temperature range. In other words, if the potential along the H-bond gives rise to the stretching mode in the vibrational spectrum, one would in principle observe discrepancies in the stretching mode.

Temperature [K]	Phase
271	Ice Ih
269	supercooled water
271	supercooled water
273	supercooled water
274	stable water
275	stable water
276	stable water
278	stable water
280	stable water
285	stable water
290	stable water
296	stable water

Table 2: *Set of temperatures and phases of H_2O recordered in the inelastic neutron experiment carried on the SEQUOIA spectrometer at SNS. The study of the evolution of the stretching vibrational mode requires data at several temperatures and in different phases (solid, liquid, liquid supercooled).*

A rigorous data analysis of an INS experiment requires a data reduction that takes into account multiple scattering (not negligible in our data) and multiphonon corrections (that one usually minimizes performing experiments at very low temperatures). An accurate multiple scattering correction for the whole energy range requires the development of a Monte Carlo simulation, that would have been beyond the scope of this thesis. In contrast, the multiple scattering correction limited to the higher part of the energy range can be performed by a simple model tested in previous work by our group [99]. The multiphonon contribution cannot be minimized by lowering the temperature, being fixed for physical reasons. However, as we will see in the chapter devoted to the data analysis, the density of vibrational states is obtained as the low q limit of the dynamical structure factor. In this limit the multiphonon contribution is negligible.

For these reasons we will focus our attention on the O-H stretching of ice and water.

Personal contribution

Usually an experimental work is carried on by a team of scientist, and this is the case. For sake of clarity my personal contribution to the single parts of this study is reported in table 3.

Experiment	Proposal	Sample / Can preparation	Measurements	Data Analysis
DINS on Ice Ih	ν	ν	ν	ν
DINS on Ice Ic				ν
INS on H_2O				ν

Table 3: *This table shows the personal contribution of the author of this thesis to this work. Where the symbol ν does not appear the contribution should be considered negligible. The submission of the proposal for the INS on H_2O has been done by my research group in Tor Vergata, as the sample preparation and the measurements. The DINS on ice Ic (also named Oriented ice experiment) has been proposed by the group of Tor Vergata and of the Prof. Andrew Hodgson (University of Liverpool). The latter also provided to the sample preparation.*

Synopsis

In the first chapter of this thesis the theoretical background of the adopted spectroscopic techniques will be presented. The second chapter will be devoted to the description of the experimental set up used for the experiments. A particular attention will be dedicated to the main difference between SEQUOIA and VESUVIO spectrometers: they are both based on the TOF technique, but the former is a direct while the latter is an inverse geometry spectrometer. Chapters from 3 to 5 will contain the data analysis of each experiment: DINS on polycristalline Ice Ih, DINS on single crystal Ice Ic, and INS on water and ice in chapters 3,4, and 5, respectively. Finally in chapter 6 the results of all three experiments will be presented and discussed.

The choice of organizing the results of three different experiments in the same chapter is due to the fact that this work should be read as a unique big experiment aiming at a deeper comprehension of the physics of water and ice. In this regard the author would like to give an overview of results that could be used to arrange together all pieces of this huge puzzle.

Chapter 1

Theory of neutron scattering

In this chapter the theoretical framework of the experimental techniques used in this work will be reported. First of all we will describe the general features of the neutron as a probe. In the following sections, a general treatment of the neutron scattering theory and the spectroscopic techniques will be exposed.

1.1 Neutron as a probe

The discovery of the neutron dates back to the 30' when J. Chadwick showed that when beryllium was bombarded with α particles, neutral particles were emitted having a mass close to the proton mass. The particles were called neutrons and designated by ${}^{1}_{0}$n:

$$ {}^{9}_{4}Be +^{4}_{2} He \rightarrow^{12}_{6} C +^{1}_{0} n \tag{1.1} $$

Neutron scattering techniques are a very useful tools for the investigation of matter, with particular regard to condensed matter, due to the peculiar features of the neutron, as the mass value, the charge, the spin and the magnetic dipole momentum [110].

mass	$939.57 Mev/c^2$
charge	0
spin	1/2
magnetic dipole momentum	-1.913 μ_N

The zero value of the electric charge, for example, allows the neutrons to deeply penetrate into material. For these reasons neutrons are very good probes for the study of the bulk of the system. Indeed, in the case of liquids this feature becomes essential for the presence of the container whose thickness in most cases is comparable to that of the sample.

Neutrons can be also used to study the microscopic magnetic features of a sample such as magnetic structures and fluctuations thanks to their magnetic moment.

In a scattering event a neutron interacts with the atomic nuclei. The cross section is indeed insensitive to the electronic cloud and then it is not correlated to the atomic number. As a consequence lighter atomic nuclei can be revealed with neutrons, still in presence of heavy atoms.

The De Broglie wavelength of a neutron in thermal equilibrium, with an energy of about $k_B T$, at room temperature is of few $\mathring{A}$, corresponding to an energy of about 25 meV. Therefore, on the one hand its energy is comparable to the vibrational energy of a molecule, on the other hand its associated wavelength is very close to the interatomic distance in solids. For this reason, both dynamical and structural information can be gathered from a neutron scattering experiment.

The scattering of a neutron without loss of energy is called *elastic* scattering. If it loses an amount of energy is indeed called *inelastic* scattering. If the scattering is elastic the outgoing neutron wave functions may or may not interfere. *Coherent scattering* arises when there is interference among the neutrons scattered from different nuclei of the same type. Coherent elastic scattering is measured in diffraction experiments and tells us the relative positions of atoms, molecules or even bigger structures such as nanoparticles or macromolecules. *Incoherent scattering* instead arises when the natural isotopic and spin mixture of the sample destroys local order and reduces, or completely removes, interference among the scattered neutrons. In this work we will focus on the *inelastic incoherent neutron scattering*. In a neutron scattering experiment incoming neutrons can be distinguished by their kinetic energy in four main categories and are generally named *cold* neutrons (1 μeV < E < 25 meV), *thermal* neutrons (E $\approx$ 25 meV), *epithermal* neutrons (0.5 eV < E < 1 KeV) and *fast* neutrons (E >> 1 KeV).

To the purpose we used two different pulsed neutron sources with two different spectrometers that can work with epithermal neutrons. In two of the three experiments we carried out a measurement with a technique called Deep Inelastic Neutron Scattering (DINS), allowing for the evaluation of the momentum distribution of an atomic mass in a sample. In the third experiment we carried out a measurement by means of the Inelastic Neutron Scattering technique to measure the vibrational spectrum of a molecule.

1.2 Neutron scattering differential cross section

In a scattering experiment, an incident beam of neutrons with momentum $\hbar\vec{k}$ and energy E, after the interaction with the sample, is scattered within the solid angle Ω, with final mo-

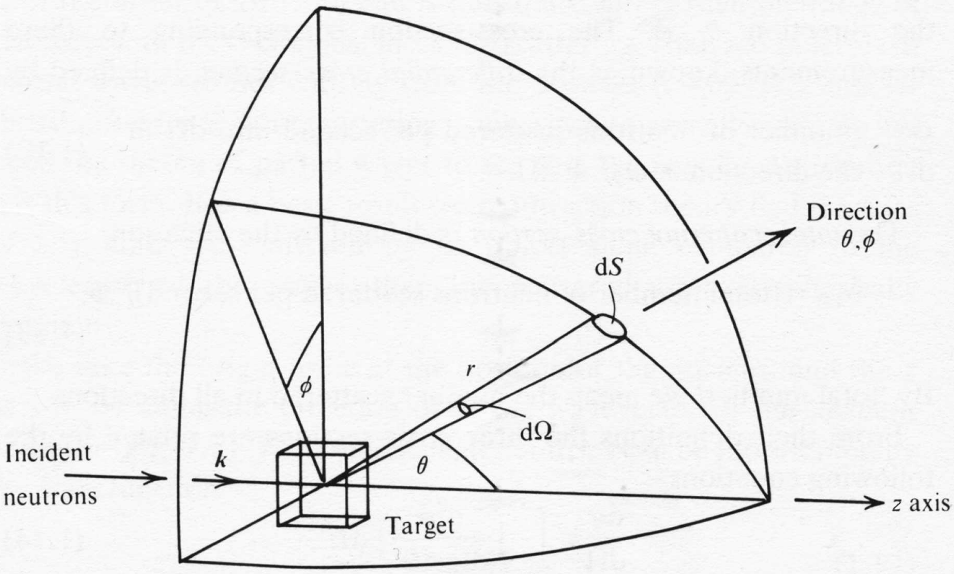

Figure 1.1: *Typical geometry of a scattering event.*

mentum and energy equal to $\hbar\vec{k}_0$ and E_0 respectively (see figure 1.1). The incident neutrons flux Φ is defined as [111]:

$$\Phi = \frac{number\, of\, neutrons}{area \cdot time} = \frac{number\, of\, particles}{volume} \cdot velocity. \tag{1.2}$$

Scattered particles are collected by a detector placed at a distance $\vec{r} = \vec{r}(\theta, \phi)$ from the sample: this counts all the neutrons arriving within a solid angle $d\Omega$ around $\Omega(\theta, \phi)$. If it can perform an energy analysis, then we have access to the double differential cross section, that is the counting rate per unit solid angle and energy interval, normalized to the incident flux:

$$\frac{d^2\sigma}{d\Omega dE'} = \frac{number\, of\, neutrons\, within\, d\Omega\, around\, \Omega}{time\, \Phi dE'}. \tag{1.3}$$

Instead, if all neutrons are collected without energy analysis, the measured quantity is called differential cross section and represents the counting rate in Ω:

$$\frac{d\sigma}{d\Omega} = \int \frac{d^2\sigma}{d\Omega dE'} dE'. \tag{1.4}$$

The total neutron scattering from the sample is instead:

$$\sigma = \int \frac{d^2\sigma}{d\Omega dE'} dE' d\Omega. \tag{1.5}$$

A formally correct derivation of the differential cross section requires application of the scattering theory. Nevertheless in the case of neutrons it can be calculated within the Born approximation, as the perturbation brought by the scattering event to the incident beam is so small that the wave function of the neutron-nucleus system can be factorized as the product of the wave functions of the unperturbed components of the system. This means in practice that the amplitude of wave function of the neutron scattered by a nucleus is already very small at a distance from the scattering center of the order of the first neighbor distance. When this condition is realized, the cross section can be evaluated within the linear response theory: under the hypothesis that the probe does not appreciably perturbs the target, the total scattering function from an ensemble of N molecules is the sum of the scattering functions from the individual nuclei. We can therefore evaluate the cross section starting from the Fermi's gold rule for the transition probability between the initial and final state of the neutron-nucleus system [112].

Let $|\lambda>$ be the target initial state, E_λ its energy, and $|k, s> = |k> |s>$ the plane wave function of the incident neutron, with momentum $\hbar\vec{k}$ and spin $\vec{s}$. In the absence of magnetic field the neutron energy is $E = \frac{\hbar^2\vec{k}^2}{2m_n}$, independent on $\vec{s}$, where m_n is the neutron mass and the transition probability from the initial state $|\lambda> |k> |s>$ to the final state $|\lambda'> |k'> |s'>$ is:

$$W_{ks\lambda \to k's'\lambda'} = \frac{2\pi}{\hbar} | < \vec{k}s\lambda|\hat{U}|\vec{k}'s'\lambda' > |^2 \delta(E + E_{\lambda'} - E' - E_\lambda), \tag{1.6}$$

where $\hat{U}$ is the neutron-nucleus interaction potential. The measured quantity however depends on $W_{ks\rightarrow k's'}$, i.e. the probability associated with the transition between the initial and final state of the probe, which can be obtained from equation 1.6, after summing over all the initial and final states of the nucleus (the latter weighted according to their statistical population, p_λ):

$$W_{ks\rightarrow k's'} = \frac{2\pi}{\hbar}\sum_{\lambda\lambda'} p_\lambda W_{ks\lambda\rightarrow k's'\lambda'}. \tag{1.7}$$

If the incident beam contains N neutrons in the state $|k, s>$, the number of scattered neutrons in the state $|k'>|s'>$ per second is $NW_{ks\rightarrow k's'}$. After integration over all possible $|k'>$, this equals the product of the incident flux times the total neutron scattering cross section:

$$\Phi\sigma_{tot}|_{s\rightarrow s'} = N\sum_{k'} W_{ks\rightarrow k's'} = NV\int \frac{d^3k'}{2\pi^3} W_{ks\rightarrow k's'}. \tag{1.8}$$

The final energy is $E = \frac{\hbar^2\vec{k'}^2}{2m_n}$, $dk' = \frac{m_n}{\hbar^2 k'}dE'$ and $\frac{\Phi V}{N} = \frac{\hbar k}{m_n}$, the latter equation gives:

$$\sigma_{tot}|_{s\rightarrow s'} = \frac{V^2}{(3\pi)^3}\frac{k'}{k}\frac{m_n^2}{\hbar^3}\int W_{ks\rightarrow k's'}dE'd\Omega \tag{1.9}$$

and the double differential cross section can be expressed as:

$$\frac{d^2\sigma}{d\Omega dE'} = \frac{k'}{k}\frac{m_n^2}{(2\pi\hbar^2)^2}\sum_{\lambda\lambda' ss'} p_\lambda p_s < ks\lambda|\hat{U}|k's'\lambda' > |^2\delta(E_{\lambda'} - E_\lambda + \hbar\omega), \tag{1.10}$$

with $\hbar\omega = E' - E$.

Since the neutron wavelength is of the order of $\approx 10^{-10}$ m and the range of the nuclear forces is of the order of $\approx 10^{-15}$ m, neutrons see the atoms as if they were points. As a consequence the scattering from a single atom can only be isotropic: in practice it is characterized by a single scalar parameter, b, named scattering length [113]. This means that the differential cross section can be calculated by replacing $\hat{U}$ with the Fermi's effective potential:

$$\hat{U} = \sum_\alpha \frac{2\pi\hbar^2}{m_n} b_\alpha \delta(r - r_\alpha), \tag{1.11}$$

where r_α is the time dependent position of the α^{th} nucleus and b may be a complex number, whose imaginary part represents the absorption of neutrons during the interaction. In general b depends on the atomic species and on its isotopic state.

The Fermi potential gives the correct value of the scattering from a single bound nucleus, within the Born approximation. A thermal or epithermal neutron (with energy up to few eV) cannot indeed excite nuclear transitions (requiring energy of the order of 1 Mev), moreover the quantum numbers cannot change for a bound atom, hence the element of matrix in 1.10

becomes: $< \lambda\lambda' >< k|\delta(x)|k' >= \delta_{\lambda\lambda'} \int dr^3 e^{-i\vec{k}\cdot\vec{r}} \delta(r) e^{i\vec{k}'\cdot\vec{r}} = \delta_{\lambda\lambda'}$. The differential and total scattering cross section are: $\frac{d\sigma}{d\Omega} = |b^2|$ and $\sigma = 4\pi|b^2|$ respectively.

Let us consider an array of nuclei and let b_α be the scattering length of the α^{th} nucleus. The interaction of the neutron beam with the array is described by: $\hat{U}(r) = \frac{2\pi\hbar^2}{m_n} \sum_\alpha b_\alpha \delta(\vec{r} - \vec{R}_\alpha)$ and its matrix elements between the initial and final states of the neutron is:

$$< k|\hat{U}|k' >= \sum_\alpha b_\alpha \int d^3 r e^{-i\vec{k}\cdot\vec{r}} \delta(\vec{r} - \vec{R}_\alpha) e^{i\vec{k}'\cdot\vec{r}} = \sum_\alpha b_\alpha e^{i(\vec{k}-\vec{k}')\cdot\vec{R}_\alpha}. \tag{1.12}$$

If we now define the exchanged wavevector $\vec{q} = (\vec{k} - \vec{k}')$ the double differential cross-section is:

$$\frac{d^2\sigma}{d\Omega dE'} = \frac{k'}{k} \sum_{\lambda\lambda'} p_\lambda \sum_{ss'} p_\sigma | < \lambda, s| \sum_\alpha b_\alpha e^{i\vec{q}\cdot\vec{R}_\alpha} |\lambda', s' > |^2 \delta(E_{\lambda'} - E_\lambda + \hbar\omega). \tag{1.13}$$

If the nuclei are bound, $\hat{U}$ is not an operator and consequently the product $< \lambda|\lambda' >$ gives a delta function in $\lambda\lambda'$; E_λ equals $E_{\lambda'}$ and $\delta(E_\lambda - E_{\lambda'} + \hbar\omega)$ becomes $\delta(\hbar\omega)$, implying that there is no energy exchange and $k = k'$. In this case the differential cross-section is immediately found to be:

$$\frac{d\sigma}{d\Omega} = \sum_{\sigma\sigma'} p_\sigma \sum_{\alpha\alpha'} e^{i\vec{q}\cdot(\vec{R}_\alpha - \vec{R}_{\alpha'})} < \sigma|b^*_\alpha b_{\alpha'}|\sigma >, \tag{1.14}$$

that is:

$$\frac{d\sigma}{d\Omega} = \sum_{\alpha\alpha'} e^{i\vec{q}\cdot(\vec{R}_\alpha - \vec{R}_{\alpha'})} < b^*_\alpha b_{\alpha'} >, \tag{1.15}$$

where $< b^*_\alpha b_{\alpha'} >$ represents the average over the nuclear spin states and allows to drop hereafter the sum over these states. On the other hand the sum over $\alpha\alpha'$ can be separated into the sum over $\alpha = \alpha'$ and the sum over $\alpha \neq \alpha'$, and being $< b^*_\alpha b_{\alpha'} >$ equal to: $| < b > |^2$ if $\alpha \neq \alpha'$ and to $< |b|^2 > \alpha = \alpha'$, we can write:

$$< b^*_\alpha b_{\alpha'} >= | < b > |^2 + \delta_{\alpha\alpha'}(< |b|^2 > -| < b > |^2). \tag{1.16}$$

As a consequence:

$$\frac{d\sigma}{d\Omega} = | < b > |^2 \sum_\alpha e^{i\vec{q}\cdot\vec{R}_\alpha} + N \left[(< |b|^2 > -| < b > |^2)\right] = \left(\frac{d\sigma}{d\Omega}\right)_{coh} + \left(\frac{d\sigma}{d\Omega}\right)_{inc}. \tag{1.17}$$

From the physical point of view this means that neutrons do not see the array of nuclei as a crystal with uniform scattering potential, since the scattering length depends on the isotopic state and on the orientation of the nuclear spin with respect to the neutron spin. The scattering potential changes from site to site, nevertheless we can define an average potential, represented by the average scattering length $< b >$ and imagine the array of nuclei as an *average array*, giving coherent interference between the scattered neutrons, plus a random distribution of deviations from the average. These random disordered contributions to the scattering potential cannot give coherent interference, but contribute to the incoherent scattering from the sample.

1.3 Incoherent inelastic neutron cross section

In DINS and INS techniques the scattering from the sample is totally incoherent and with energy loss of the scattered neutrons. To describe this physical process we need the double differential cross section.

The matrix element in equation 1.13 can be rewritten in the following form:

$$| < \lambda, s | b_\alpha e^{i\vec{q}\cdot\vec{R}_\alpha} | \lambda', s' > |^2 = b_\alpha^* < \lambda', s' | e^{i\vec{q}\cdot\vec{R}_\alpha} | \lambda, s >^* b_{\alpha'} < \lambda', s' | e^{i\vec{q}\cdot\vec{R}_\alpha} | \lambda, s >, \tag{1.18}$$

Since the scattering lengths are real and using the propriety $< a|O|b >^* = < b|O^*|a >$:

$$b_\alpha b_{\alpha'} < \lambda, s | e^{-i\vec{q}\cdot\vec{R}_{\alpha'}} | \lambda', s' >< \lambda', s' | e^{i\vec{q}\cdot\vec{R}_\alpha} | \lambda, s >, \tag{1.19}$$

The integral expression for the delta function is:

$$\delta(E_{\lambda'} - E_\lambda + \hbar\omega) = \frac{1}{2\pi\hbar} \int_{-\infty}^{+\infty} e^{i\frac{E_{\lambda'} - E_\lambda}{\hbar}t} e^{-i\omega t} dt. \tag{1.20}$$

On substituting equations 1.19 and 1.20 into the equation 1.13, we obtain:

$$\begin{aligned} \frac{d^2\sigma}{d\Omega dE'} =& \\ & \frac{k'}{k} \sum_{\lambda\lambda' ss'} p_\lambda p_s \sum_{\alpha\alpha'} b_\alpha b_{\alpha'} < \lambda, s | e^{-i\vec{q}\cdot\vec{R}_{\alpha'}} | \lambda', s' > \times \\ & < \lambda', s' | e^{i\vec{q}\cdot\vec{R}_\alpha} | \lambda, s > \frac{1}{2\pi\hbar} \int_{-\infty}^{+\infty} e^{i\frac{E_{\lambda'} - E_\lambda}{\hbar}} t e^{-i\omega t} dt. \end{aligned} \tag{1.21}$$

Furthermore $e^{\frac{-i\hat{H}t}{\hbar}} | \lambda, s >= e^{\frac{-iEt}{\hbar}} | \lambda, s >$, so 1.21 becomes:

$$\begin{aligned} \frac{d^2\sigma}{d\Omega dE'} =& \\ & \frac{k'}{k} \frac{1}{2\pi\hbar} \sum_{\lambda\lambda' ss'} p_\lambda p_s \sum_{\alpha\alpha'} b_\alpha b_{\alpha'} < \lambda, s | e^{-i\vec{q}\cdot\vec{R}_{\alpha'}} | \lambda', s' > \times \\ & < \lambda', s' | e^{\frac{i\hat{H}t}{\hbar}} e^{i\vec{q}\cdot\vec{R}_\alpha} e^{\frac{-i\hat{H}t}{\hbar}} | \lambda, s > \int_{-\infty}^{+\infty} e^{-i\omega t} dt. \end{aligned} \tag{1.22}$$

Summing over the final state λ' and s' and using the enclosure relationship, the double differential cross section becomes:

$$\begin{aligned} \frac{d^2\sigma}{d\Omega dE'} =& \\ & \frac{k'}{k} \frac{1}{2\pi\hbar} \sum_{\lambda s} p_\lambda p_s \sum_{\alpha\alpha'} b_\alpha b_{\alpha'} \times \\ & \int_{-\infty}^{+\infty} < \lambda, s | e^{-i\vec{q}\cdot\vec{R}_{\alpha'}} e^{\frac{i\hat{H}t}{\hbar}} e^{i\vec{q}\cdot\vec{R}_\alpha} e^{\frac{-i\hat{H}t}{\hbar}} | \lambda, s > e^{-i\omega t} dt. \end{aligned} \tag{1.23}$$

An operator $O_H(t)$ in the so called Heisenberg picture is related to the O_S operator in the Schroedinger picture via the relation $O_H(t) = e^{i\hat{H}t/\hbar} O_S e^{-i\hat{H}t/\hbar}$. The main difference between the Heisenberg and the Schroedinger pictures is that in the former the operators have an explicit time dependence, while in the latter the time dependence is a feature of the wave vectors only. However, as a particular case, an operator in the Schroedinger picture can be viewed as an operator in the Heisenberg picture defined at a particular fixed time. The choice of the particular time is arbitrary, so we will choose the time $t = 0$. Following this ideas the operators in the matrix element of 1.23 can be exchanged with their counterparts in the Heisenberg picture at the times 0 and t. So the 1.23 becomes:

$$\frac{d^2\sigma}{d\Omega dE'} = \frac{k'}{k}\frac{1}{2\pi\hbar}\sum_{\lambda s} p_\lambda p_s \sum_{\alpha\alpha'} b_\alpha b_{\alpha'} \int_{-\infty}^{+\infty} < \lambda, s| e^{-i\vec{q}\cdot\vec{R}_{\alpha'}(0)} e^{i\vec{q}\cdot\vec{R}_\alpha(t)} |\lambda, s > e^{-i\omega t} dt. \tag{1.24}$$

Now the matrix element in 1.24 is a correlation function of the position of a nucleus at the time 0 with the position of another nucleus at the time t. However if the scattering is totally incoherent this correlation function is zero except for $\alpha = \alpha'$, i.e. a nucleus motion is not correlated with other nuclei in the system. By integrating the incoherent part of 1.17 we obtain $\sigma_{inc} = 4\pi(< b^2 > - < b >^2)$ and defining the thermal average of an operator as $< O >_T = \sum_i p_i < \phi_i|O|\phi_i >$ we obtain from 1.24:

$$\frac{d^2\sigma}{d\Omega dE'} = \frac{\sigma_{inc}}{4\pi}\frac{k'}{k}\frac{1}{2\pi\hbar}\sum_{\alpha}\int_{-\infty}^{+\infty} \left\langle e^{-i\vec{q}\cdot\vec{R}_{\alpha'}(0)} e^{i\vec{q}\cdot\vec{R}_\alpha(t)} \right\rangle_T e^{-i\omega t} dt. \tag{1.25}$$

Let us define the Dynamical Structure Factor, that we will express as a function of the double differential cross section, since we will handle this function in the data analysis. From now on we suppress all the labels indicating incoherence:

$$S(\vec{Q}, \omega) = \frac{4\pi}{\sigma}\frac{k_i}{k_f}\left(\frac{d^2\sigma}{dE_f d\Omega}\right). \tag{1.26}$$

The dynamical structure factor is also related to the Intermediate Scattering Function:

$$S(\vec{Q}, \omega) = \frac{1}{2\pi\hbar}\int \Im(\vec{Q}, t) e^{-i\omega t} dt. \tag{1.27}$$

1.4 Scattering from vibrating molecules

INS technique samples molecular vibrations. In this section we will derive the dynamical structure factor of a sample composed of vibrating molecules.

We will express the dynamical structure factor in terms of the internal and external dynamics of the molecules in the sample. If the molecule consist of N_{atoms} atoms then the total number of atoms in the system is $N = N_{atoms} \times N_{mol}$, where N_{mol} is the total number of molecules. It is useful to treat the contribution of the atoms and molecules separately. We will indeed focus our attention to the atoms vibrations.

If $r(t)$ is the position of the atom in space, it can be expressed as:

$$\vec{r}(t) = \vec{u}_{ext}(t) + \vec{u}_{int}(t), \tag{1.28}$$

where $u_{ext}(t)$ and $u_{int}(t)$ are the position of the molecular center of mass and the position of the atom with respect to the molecular center of mass, respectively. So the Heisenberg operator in 1.23 becomes:

$$e^{i\vec{Q}\cdot\vec{r}(t)} = e^{i\vec{Q}\cdot\vec{u}_{ext}(t)} e^{i\vec{Q}\cdot\vec{u}_{int}(t)} \tag{1.29}$$

and since the Fourier transform of a product of two functions is the convolution product of the Fourier transformed functions the dynamical structure factor can be written as:

$$S(\vec{Q},\omega) = S_{int}(\vec{Q},\omega) \otimes S_{ext}(\vec{Q},\omega). \tag{1.30}$$

We can write the dynamical structure factor of the intramolecular vibrations only:

$$S_{int}(\vec{Q},\omega) = \frac{1}{2\pi\hbar} \sum_i \int \left\langle e^{i\vec{Q}\cdot\vec{u}_{int}(0)} e^{i\vec{Q}\cdot\vec{u}_{int}(t)} \right\rangle_T e^{i\omega t} dt. \tag{1.31}$$

It is convenient to develop the total internal atomic displacements into their individual vibrations in Cartesian components. The displacement, as a function of time, of a particular atom l is then the sum of the displacements of the atom in each of the internal modes, labelled $\nu = 1, 2, ..., 3N_{atom} - 6$:

$$\vec{u}_{l,int}(t) = \sum_\nu {}^\nu\vec{u}_l(t) =^1 \vec{u}_{l,x}(t) +^1 \vec{u}_{l,y}(t) +^1 \vec{u}_{l,z}(t) +^2 \vec{u}_{l,x}(t) +^2 \vec{u}_{l,y}(t) +^2 \vec{u}_{l,z}(t) + ... \tag{1.32}$$

We shall focus on the dynamics of a single atom, suppressing the subscript l, since the INS experiment subject of this work concerns the hydrogen motion in a water molecule. For the sake of completeness the dynamics of the molecule could be eventually described as the sum of its atoms taken individually.

Considering only one dimension, as x direction, the dynamical structure factor for one atom is:

$$S_{int}(\vec{Q},\omega) = \frac{1}{2\pi\hbar} \int \left\langle e^{i\vec{Q}\cdot\sum_\nu {}^\nu\vec{u}_x(0)} e^{i\vec{Q}\cdot\sum_\nu {}^\nu\vec{u}_x(t)} \right\rangle_T e^{i\omega t} dt. \tag{1.33}$$

We can expand the summation over the internal modes that, within the harmonic approximation, are dynamically decoupled. The sum of the arguments in the exponential terms turns out to be a product of exponentials and the equation 1.33 becomes:

$$S_{int}(\vec{Q},\omega) = \frac{1}{2\pi\hbar} \prod_{\nu=1}^{3N-6} \int \left\langle e^{i\vec{Q}\cdot{}^\nu\vec{u}(0)} e^{i\vec{Q}\cdot{}^\nu\vec{u}(t)} \right\rangle_T e^{i\omega t} dt, \tag{1.34}$$

where we suppressed the Cartesian indicator x.

In the following, we shall treat each mode individually and, as done for the equation 1.27, rewrite each term of 1.34 as:

$$S(\vec{Q},\omega_\nu) = \frac{1}{2\pi\hbar}\int \Im_{nu}(\vec{Q},t)e^{-i\omega t}dt, \tag{1.35}$$

where $\Im_{nu}(\vec{Q},t)$ is:

$$\Im_{nu}(\vec{Q},t) = \left\langle e^{i\vec{Q}\cdot{}^{\nu}\vec{u}_x(0)} e^{i\vec{Q}\cdot{}^{\nu}\vec{u}_x(t)} \right\rangle_T . \tag{1.36}$$

The position of the nucleus, as a function of time, is given in terms of the creation, $\hat{a}^+$, and the annihilation operators $\hat{a}^-$ by:

$${}^{\nu}u(t) ={}^{\nu} u\left[\hat{a}^+e^{i\omega t} + \hat{a}^- e^{-i\omega t}\right]. \tag{1.37}$$

This is equivalent to the alternative representation:

$${}^{\nu}\vec{u}(t) ={}^{\nu} \vec{u}\cos\omega t + \frac{p_{atom}}{m\omega}\sin\omega t, \tag{1.38}$$

where ${}^{\nu}u$ is the time independent maximum amplitude of the vibration and p_{atom} is the linear momentum of the atom. Using the relation $\left\langle e^A e^B\right\rangle_T = \left\langle e^{A^2}\right\rangle_T \left\langle e^{AB}\right\rangle_T$ for the thermal average of operators equation 1.36 becomes:

$$\Im_{nu} = e^{\left\langle -\left[\vec{Q}\cdot{}^{\nu}\vec{u}(0)\right]^2\right\rangle_T} e^{\left\langle \left[\vec{Q}\cdot{}^{\nu}\vec{u}(0)\right]\left[\vec{Q}\cdot{}^{\nu}\vec{u}_(t)\right]\right\rangle_T}. \tag{1.39}$$

Let's consider the terms of equation 1.39 individually. For a given mode ν only the energy levels 0, 1, 2 3 ... are available and given by the quantum number, n. The thermal average of the argument of first term is:

$$\begin{aligned} &\left\langle -\left[\vec{Q}\cdot{}^{\nu}\vec{u}(0)\right]^2\right\rangle_T = \\ &\qquad \sum_n P_n \left\langle n\right| - \left[\vec{Q}\cdot{}^{\nu}\vec{u}(0)\right]^2 \left|n\right\rangle = \\ &\qquad -\left[\vec{Q}\cdot{}^{\nu}\vec{u}\right]^2 (2 < n >_T +1)\,. \end{aligned} \tag{1.40}$$

The expectation value of the quantum number n is:

$$< n >_T = \sum_n P_n \left\langle \lambda s|n|\lambda' s'|\right\rangle = \sum_n nP_n \left\langle \lambda s||\lambda' s'|\right\rangle = \sum_n nP_n. \tag{1.41}$$

The population of a level P_n can be written as:

$$P_n = \frac{e^{-\frac{n\hbar\omega_\nu}{k_BT}}}{\sum_n e^{-\frac{n\hbar\omega_\nu}{k_BT}}}, \tag{1.42}$$

so for $< n >_T$ we obtain:

$$< n >_T = \sum_n n \frac{e^{-\frac{n\hbar\omega_\nu}{k_B T}}}{\sum_n e^{-\frac{n\hbar\omega_\nu}{k_B T}}} = \frac{e^{-\frac{\hbar\omega_\nu}{k_B T}}}{1 - e^{-\frac{\hbar\omega_\nu}{k_B T}}} = \frac{1}{e^{\frac{\hbar\omega_\nu}{k_B T}} - 1}. \tag{1.43}$$

Substituting this result into the equation 1.40, we obtain:

$$\begin{aligned} \left\langle - \left[\vec{Q} \cdot {}^{\nu}\vec{u}(0)\right]^2 \right\rangle_T &= \\ & - \left[\vec{Q} \cdot {}^{\nu}\vec{u}\right]^2 \left(\frac{1 + e^{\frac{\hbar\omega_\nu}{k_B T}}}{e^{\frac{\hbar\omega_\nu}{k_B T}} - 1} \right) \left(\frac{1}{2}\right) = \\ & - \left[\vec{Q} \cdot {}^{\nu}\vec{u}\right]^2 \coth \frac{\hbar\omega_\nu}{2k_B T}. \end{aligned} \tag{1.44}$$

The first term of equation 1.39 is known as the Debye-Waller factor and it is often found in the literature as e^{2W}. The Debye-Waller factor is a temperature dependent term, through the atomic displacement, and its major effect is to decrease the observed intensity in neutron spectroscopy. This is the reason why experimental efforts are done to reduce this factor as much as possible. This can be done in two ways: decreasing T or $\vec{Q}$.

The second term of equation 1.39 is:

$$e^{\left\langle [\vec{Q}\cdot {}^{\nu}\vec{u}(0)][\vec{Q}\cdot {}^{\nu}\vec{u}_(t)] \right\rangle_T} = e^{\left\langle [\vec{Q}\cdot {}^{\nu}\vec{u}]^2 \left[(<n_T>+1)e^{-i\omega t} + <n_T> e^{i\omega t}\right] \right\rangle} \tag{1.45}$$

and substituting from equation 1.43:

$$\begin{aligned} e^{\left\langle [\vec{Q}\cdot {}^{\nu}\vec{u}(0)][\vec{Q}\cdot {}^{\nu}\vec{u}_(t)] \right\rangle_T} &= \\ & e^{\left[\left([\vec{Q}\cdot {}^{\nu}\vec{u}]^2 \frac{e^{\frac{\hbar\omega}{2k_B T}}}{e^{\frac{\hbar\omega}{k_B T}} - 1} \right) \left(\frac{e^{\frac{\hbar\omega}{2k_B T}}}{e^{i\omega t}} + \frac{e^{i\omega t}}{e^{\frac{\hbar\omega}{2k_B T}}} \right) \right]}. \end{aligned} \tag{1.46}$$

In the latter equation we can recognize the modified Bessel function of the first kind I:

$$\sum_{n=-\infty}^{+\infty} y^n I_n \{x\} = e^{\left[\frac{x}{2}\left(y + \frac{1}{y}\right)\right]}, \tag{1.47}$$

where x and y are:

$$\begin{aligned} x &= 2 \left[\vec{Q} \cdot {}^{\nu}\vec{u}\right]^2 \frac{e^{\frac{\hbar\omega}{k_B T}}}{e^{\frac{\hbar\omega}{k_B T}} - 1}; \\ y &= \frac{e^{i\omega t}}{e^{\frac{\hbar\omega}{k_B T}}}. \end{aligned} \tag{1.48}$$

Substituting the equation 1.47 into 1.46 and using the hyperbolic sine function, we can regroup the terms from equations 1.41, 1.45, 1.46 and 1.47:

$$\begin{aligned} e^{\left\langle [\vec{Q}\cdot {}^{\nu}\vec{u}(0)][\vec{Q}\cdot {}^{\nu}\vec{u}_(t)] \right\rangle_T} &= \\ & \sum_{n=-\infty}^{+\infty} e^{n\frac{\hbar\omega}{2k_B T}} e^{in\omega t} I_n \left\{ \frac{\left[\vec{Q} \cdot {}^{\nu}\vec{u}\right]^2}{\sinh \frac{\hbar\omega}{2k_B T}} \right\}. \end{aligned} \tag{1.49}$$

In the INS experiment we will concentrate our attention on the O-H stretching mode which shows an energy value above 400 meV. The value of k_BT at room temperature is around 25 meV, so the argument of the hyperbolic sine in 1.49 is larger than 10. As a consequence the argument of the Bessel function is small enough that we can take only the first term of its power series expansion:

$$I_n\left\{x\right\} \approx \frac{1}{|n!|}\left(\frac{x}{2}\right)^{|n|}. \tag{1.50}$$

Furthermore for high x, $\sinh x \approx e^x$, so we obtain, for a certain order n:

$$e^{\langle[\vec{Q}\cdot{}^{\nu}\vec{u}(0)][\vec{Q}\cdot{}^{\nu}\vec{u}_{(}t)]\rangle_T^n} = e^{in\omega t}\frac{e^{\frac{n\hbar\omega}{2k_BT}}}{e^{\frac{|n|\hbar\omega}{2k_BT}}}\frac{\left[\vec{Q}\cdot\,{}^{\nu}\vec{u}\right]^{2|n|}}{|n!|}. \tag{1.51}$$

The order n labels the final state of the sample and n=1 represent the (0-1) transition, n=-1 is (1-0) and so on, while the n=0 solution refers to the elastic scattering. Considering only neutron energy loss processess allow us to remove the modulus of the n and $n!$.

This result can be generalized in three dimensions. From equation 1.34, the contribution to the spectrum of each Fourier component is a δ-function corresponding to each normal mode and its overtones.

The time independent product of exponentials in the equation 1.44 becomes the exponential of a sum over all modes. Thus equation 1.34 becomes for the individual ν^{th} normal mode, excited to its n^{th} harmonic:

$$S(\vec{Q},\omega_\nu)^n = \frac{\left[\vec{Q}\cdot\,{}^{\nu}\vec{u}\right]^{2n}}{n!}e^{-\left(\vec{Q}\sum_\nu{}^{\nu}\vec{u}\right)^2}\delta(E_i - E_f + n\hbar\omega_\nu). \tag{1.52}$$

Finally, let us reintroduce the atomic index l and include the atomic cross section σ. Then the scattering intensity contribution to a given spectral band, that arises from the l^{th} atom is:

$$S^\bullet(\vec{Q},\omega_\nu)_l^n = \frac{\sigma_l}{4\pi}\frac{\left[\vec{Q}\cdot\,{}^{\nu}\vec{u}\right]^{2n}}{n!}e^{-2W}. \tag{1.53}$$

From now on, we will refer to this equation for the dynamical structure factor.

1.5 Deep inelastic neutron scattering

It was first pointed out by Hohenberg and Platzmann, Gol'danskii, and Ivanov and Sayasov about 40 years ago [26, 114, 25, 115], that neutron scattering at high energy, $\hbar\omega$, and high momentum transfers, $\hbar q$, could be used to measure directly the distribution of atomic momentum $\vec{p}$ in condensed matter systems. The interest of such measurements is clear when we consider the fundamental role played by momentum in both classical and quantum mechanics. In the kinematic regime of interest at high momentum and energy transfer, the two dynamical variables $\vec{q}$ and ω become coupled into a single variable y, and the results of the measurements can be described in isotropic systems by the so-called single-particle neutron Compton profile (NCP), $J(y)$ [77]. The experimental technique is analogous to the measurement of the electron momentum distribution through the Compton scattering of high-energy photons from electrons, or the nucleon momentum distribution via the quasi-elastic electron scattering from nuclei, and is known as Neutron Compton Scattering (NCS), or Deep Inelastic Neutron Scattering (DINS) [59]. It is possible to find in DINS conceptual elements and computational approaches common to other techniques, namely the Compton scattering of X-rays and γ-rays, used for the determination of electron momentum distributions in solids, and quasi-elastic electron scattering of nucleons in nuclei, used for the determination of nucleon momentum distributions [116]. However, at present DINS is the only effective technique for deriving the single-particle (atomic and molecular) momentum distributions, $n(p)$, in condensed matter systems. This represents an important physical quantity in all those systems where the dynamic behavior departs from the classical one. The so called Impulse Approximation (IA) is the key feature of the DINS, consisting in assuming a target particle as free, therefore neglecting the interaction with all other particles. In other words, the energy exchanged between the incident and the target particles is much larger than the binding energy of the system. In a classical system the IA holds when [117]

$$q >> F_i \Delta t, \tag{1.54}$$

where q is the momentum exchanged in the scattering event, F_i the strength acting on the target particle due to the the presence of all the other particles of the system and Δt is the duration time of the interaction [118].

The IA has some important implications:

- the scattering event is completely incoherent: the scattering is from a single particle, the presence of the other particles can be completely neglected;
- the interaction occurs in a very short time interval. Typically of the order of $\Delta t = \Delta r / v$, where Δr is the radius of the interaction and v is velocity of the incident particle;
- final wave function of the target particle is a plane wave;
- the system in its initial state can be considered as a non interacting system with momentum distribution $n(\vec{p})$;

Then this allows us to consider the system as a free particle system. In this framework the dynamical structure factor is a δ function with a Doppler broadening arising from the velocity distribution of the particle. The reconstruction of the momentum distribution is then straightforward.

The IA is an exact approximation in in the asymptotic case where the wave vector exchanged takes an infinite value. In all practical cases one must consider the corrections to the model and we will refer to that corrections as initial or final state effects (ISE and FSE). In the latter case it is considered that the target particle does not behave exactly as a free particle, while the ISE takes into account that the particles in their initial state could have a discrete energy distribution instead of a continuous one.

Under these conditions, applying the momentum and energy conservation laws, the energy and momentum transfer are related by:

$$\hbar\omega = \frac{(p_n - p_n')^2}{2M} + \frac{(p_n - p_n') \cdot p}{M}, \tag{1.55}$$

where $\vec{p_n}$ and $\vec{p_n'}$ are the momenta of the incident and scattered neutron, respectively, M and $\vec{p}$ are the mass and the momentum of the struck particle before collision. Thus, the energy distribution of the scattered neutrons is directly related to the distribution of the momenta of the particle parallel to the momentum transfer.

The inelastic scattering cross-section for unpolarized neutrons can be rewritten as a function of the incoherent part of the dynamic structure factor $S(\vec{q}, \omega)$ via the relation [53]:

$$\frac{d^2\sigma(E_0, E_1, \vartheta)}{d\Omega dE_1} = \hbar^{-1}\sqrt{\frac{E_1}{E_0}} \left[|b|^2 S\left(\vec{q}, \omega\right) + \left(\left|b^2\right| - |b|^2 \right) S_I\left(\vec{q}, \omega\right) \right], \tag{1.56}$$

where E_1 is the energy of the scattered neutron, E_0 that of the incident neutron and θ is the scattering angle.

The incoherent structure factor is related to the single particle correlation function, as we see in equation 1.36, also named the intermediate scattering function. We are however interested in the total motion of the atoms $\vec{r}(t)$ and not simply to the motion with respect to the molecular center of mass. Then we will rewrite the single particle correlation function as:

$$Y_{jj'}\left(\vec{q}, t\right) = \left\langle \exp\left(-i\vec{q} \cdot \hat{r_j}\right) \exp\left(-i\vec{q} \cdot \hat{r_{j'}}\left(t\right)\right) \right\rangle. \tag{1.57}$$

Again, $\hat{r_j}\left(t\right)$ is the Heisenberg operator for the position of particle j at time t, $\hat{r_j} = \hat{r_j}\left(0\right)$, and N is the number of particles in the target system.

The incoherent dynamic structure factor $S_I\left(\vec{q}, \omega\right)$ is related to the single-particle correlation function, that is the equation 1.57 with $j = j'$, according to the following:

$$S_I(\vec{q}, \omega) = \frac{1}{2\pi N} \int_{-\infty}^{+\infty} \exp\left(-i\omega t\right) \sum_j Y_{jj}\left(\vec{q}, t\right) dt. \tag{1.58}$$

At the high q values, the scattering can be considered entirely incoherent, so the scattering occurs from a single particle. The interpretation of DINS data relies essentially on the fact that, if the momentum $\hbar q$ transferred between the incident neutron and the target system is sufficiently high, the inelastic neutron scattering cross section provides a direct probe of the distribution of atomic momenta in the target system.

The key approximation used in equations 1.57, with $j = j'$, for interpretation of the data is that providing t sufficiently small, $\hat{r}_j\,(t)$ can be replaced by:

$$\hat{r}_j\,(t) \approx \hat{r}_j + \frac{t}{M_j}\hat{p}_j, \tag{1.59}$$

where $\hat{p}_j$ is the momentum operator and M_j the mass of the particle j. Physically this approximation implies that the particle travels freely over times short enough that its interaction with other particles can be neglected. Inserting this approximation in the equation 1.57, and using the standard commutation relations between momentum and position,

$$[\vec{r}_i, \vec{p}_j] = i\hbar\delta_{ij}\,, \tag{1.60}$$

gives:

$$Y_{jj'}\,(\vec{q},t) = \exp\left[\frac{i\hbar t q^2}{2M_j}\delta_{jj'}\right]\left\langle \exp\left[i\vec{q}\cdot\left(\hat{r_{j'}} - \hat{r_j}\right) + \frac{it}{M_{j'}}\vec{q}\cdot\hat{p_{j'}}\right]\right\rangle\,, \tag{1.61}$$

and in the limits of high q only terms with $j = j'$ are retained, obtaining:

$$Y_{jj}\,(\vec{q},t) = \exp\left[\frac{i\hbar t q^2}{2M_j}\right]\left\langle \exp\left[\frac{it}{M_j}\vec{q}\cdot\hat{p_j}\right]\right\rangle\,. \tag{1.62}$$

It follows from equations 1.58 and 1.62 that the incoherent dynamic structure factor is given by:

$$S_I(\vec{q},\omega) = \frac{1}{2\pi N}\sum_j\int_{-\infty}^{+\infty}\exp\left(-i\omega t + \frac{i\hbar t q^2}{2M_j}\right)\left\langle \exp\left[\frac{it}{M_{j'}}\vec{q}\cdot\hat{p_j}\right]\right\rangle dt\,. \tag{1.63}$$

The correlation function in equation 1.63 can be evaluated in terms of momentum states as:

$$\left\langle \exp\left[\frac{it}{M_{j'}}\vec{q}\cdot\hat{p_j}\right]\right\rangle = \int n(\vec{p})\exp\left[\frac{it}{M}\vec{q}\cdot\vec{p}\right]d\vec{p}, \tag{1.64}$$

where $n(\vec{p})$ is the single-particle momentum distribution.

Formally, this is the diagonal matrix element in the p representation of the one particle reduced density matrix. In the simplest case in which the system can be described by a single particle in a potential, $n(\vec{p}) = |\phi(\vec{p})|^2$, where:

$$\phi(\vec{p}) = \frac{1}{\sqrt{2\pi}}\int \exp\left[\frac{i\vec{p}\cdot\vec{x}}{\hbar}\right]\Psi(\vec{x})d\vec{x}\,, \tag{1.65}$$

where $\Psi(\vec{x})$ is the spatial wave function.

Inserting equation 1.64 into equation 1.63 and performing the integration over t gives the impulse approximation to $S_{IA}(\vec{q}, \omega)$:

$$S_{IA}(\vec{q}, \omega) = \hbar \int n(\vec{p}) \delta \left[\hbar\omega - \hbar\omega_r - \frac{\vec{p} \cdot \hbar\vec{q}}{M} \right] d\vec{p}, \tag{1.66}$$

where $\hbar\omega_r = \hbar^2 q^2 / 2M$ is the recoil energy.

The physical implication of equation 1.66 is that scattering occurs between the neutron and a single particle, with conservation of kinetic energy and momentum of the system particle-neutron. $\hbar\omega_r$ is the kinetic energy the target particle would have, provided that the target is at rest and absorbs all the momentum transferred by the neutron. It gives the centroid of the observed peak at a given q associated with the particle of mass M. The momentum distribution of the struck particles broadens in a similar way as in the Doppler broadening induced by the motion of the atoms. Since the position depends on M, different masses in the sample can be separated in the observed spectrum. For example in measurements on H_2X systems the signal from hydrogen ions is easily separated from the signal due to oxygen or other heavier ions in hydrogen bonded systems.

If the impulse approximation is valid, the two dynamic variables, ω and q, can be explicitly coupled through the definition of the West scaling variable y as [119]:

$$y = \frac{M}{\hbar^2 q} \left(\hbar\omega - \hbar\omega_r \right) . \tag{1.67}$$

Equation 1.66 can be then reduced to the form

$$S_{IA}(\vec{q}, \omega) = \frac{M}{\hbar q} J \left(y, \hat{q} \right) , \tag{1.68}$$

where

$$J \left(y, \hat{q} \right) = \hbar \int n \left(p' \right) \delta \left(\hbar y - \vec{p'} \cdot \hat{q} \right) d\vec{p'}. \tag{1.69}$$

$J \left(y, \hat{q} \right)$ is the neutron Compton profile and is formally the Radon transform of the momentum distribution. Physically the quantity $\hat{q}$ is a unit vector with the same direction and sign of $\vec{q}$. The function $J \left(y, \hat{q} \right) dy$ is the probability for an atom to have a momentum parallel to $\hat{q}$ of a magnitude between $\hbar y$ and $\hbar \left(y + dy \right)$.

In an isotropic system, the direction $\hat{q}$ is immaterial, and equation 1.69 becomes:

$$J \left(y \right) = 2\pi\hbar \int_{|\hbar y|}^{\infty} pn \left(p \right) dp. \tag{1.70}$$

The geometrical interpretation of $J \left(y \right)$ in the momentum space is shown in 1.2, where $J \left(y \right)$ is calculated by measuring a distance y along the direction of q from the origin of momentum space to the point $R = y\hbar\hat{q}$, and then integrating $n(\vec{p})$ over the plane passing through R and perpendicular to q. In the simple case of a Fermi gas at $T = 0$, reported in

1.2, the momentum distribution is a solid sphere, i.e. $n(\vec{p}) = \rho$ for $p < p_f$ (where p_f is the Fermi momentum) and $n(\vec{p}) = 0$, for $p > p_f$. The function $J(y)$ is then proportional to the area of intersection of the sphere with a plane at a distance $\hbar y$ from the center of the sphere:

$$J(y) = \begin{cases} \rho\pi\hbar\left(p_f^2 - \hbar^2 y^2\right) & \text{for } p < p_f \\ 0 & \text{otherwise}. \end{cases} \tag{1.71}$$

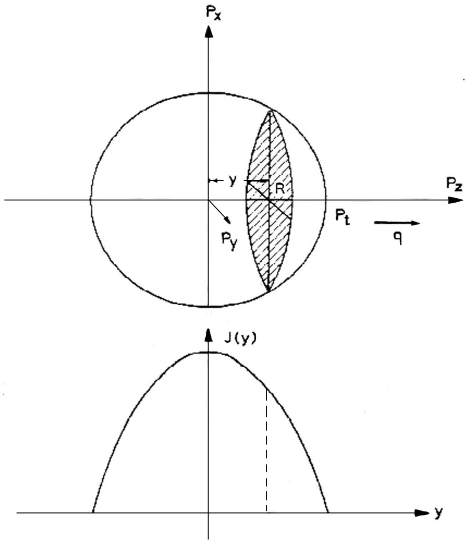

Figure 1.2: *Illustration of how the neutron Compton profile is calculated.* $J(y)$ *is obtained from an integration of* $n(\vec{p})$ *over a plane perpendicular to* $\hat{q}$ *at a distance* $\hbar y$ *from the origin of atomic momentum space. In the simple case illustrated here,* $n(\vec{p})$ *is represented by a solid sphere (i.e. an ideal Fermi liquid at zero temperature), and* $J(y)$ *is the area of the intersection between the sphere and the plane.*

Although the Radon transform of $n(\vec{p})$ for a particular y and $\hat{q}$ is an average over a plane, no information is lost, and $n(\vec{p})$ can be reconstructed from $J(y, \hat{q})$. In the isotropic case, from equation 1.70 we have:

$$n(p) = -\frac{1}{2\pi\hbar^3 y}\frac{d}{dy}J(y)|_{\hbar y = p}\,. \tag{1.72}$$

The single-particle mean kinetic energy, $\langle E_k \rangle$, is related to the second moment of $J(y)$ via:

$$\int_{-\infty}^{+\infty} y^2 J(y)\, dy = \sigma_y^2 = \frac{2M}{3\hbar^3}\langle E_K \rangle\,, \tag{1.73}$$

where σ_y is the standard deviation of the Neutron Compton Profile.

1.5.1 Correction at finite q

The first approximation implicit in the impulse approximation is that the scattering is incoherent. Roughly speaking this approximation is valid provided the atomic nearest neighbor distance is much larger than $2\pi/q$, so that the interference of the scattering amplitudes from different atoms averages to zero.

The experiments are typically done far into the limit where this approximation is valid. The second approximation of the IA is the short-time approximation embodied in equation 1.59. We wish to determine when this is valid and what the corrections are.

There is a characteristic time τ associated with the scattering process. τ is essentially the decay time of the correlation function $Y_{jj}\left(\vec{q},t\right)$ defined in equation 1.62 and, at high q, τ has the value [24]:

$$\tau = \frac{M}{q\Delta p}\,, \tag{1.74}$$

where Δp is the width of the momentum distribution of the struck particle. This decay time is due to phase mixing (see equation 1.64) as a consequence of the spread in velocities of the particles [120, 121]. Providing there are no significant deviations from a free particle motion over the time τ, then the impulse approximation will hold. For the systems we are studying τ is a short time, in the attosecond range.

If we consider the mean quadratic velocity $\left\langle v^2\right\rangle$ of the struck particles, the time of the interaction then will be approximately $1/q\left\langle v^2\right\rangle$. On the other hand $\left\langle v^2\right\rangle = \Delta p/M$. τ can be considered as the time lapse during which we can approximate the recoil of the struck particle as free.

Then a criterion for the validity of the impulse approximation for a particle confined in a potential is:

$$\omega\left(\vec{q}\right)\tau << 1\,, \tag{1.75}$$

where $\omega\left(\vec{q}\right)$ is the oscillation frequency for the particle when it has initially wave vector $\vec{q}$. The point here is that if the criterion is satisfied, the particle will have traveled only a very small part of a periodic orbit, and its motion can be treated as being unaffected by the forces. Since $\omega(\vec{q})$ is bounded, the impulse approximation will always be satisfied for sufficiently large q.

If we suppose that the condition 1.54 holds, we can demonstrate that the cross section is that of a free particle system with a momentum distribution $n(\vec{p})$. This condition in our case means that the intermolecular forces are negligible, as the potential energy, and does not appear in the conservation law. However, it is very important to point out that all the system interactions are significant because they determine the momentum distribution $n(\vec{p})$ together with its thermodynamical state.

Initial state effects

The ISE [122] account for the fact that the energy distribution of a system is a discrete set of value E_i, and in the low temperature limit all the particle would have the zero point energy [117]. The dynamical structure factor can be expressed, then, as follows:

$$S\left(\vec{q},\omega\right) = \int n\left(\vec{p}\right)\delta\left(\omega\left[\left(\vec{p}+\vec{q}\right)^2/2M + E_i\right]\right)d\vec{p}, \tag{1.76}$$

In this case the $S\left(\vec{q},\omega\right)$ is a set of many peaks. However, the ISE correction is important only at very low temperature which is not the case of this work. In the following we will not take into account this correction.

Final state effects

In the framework of the IA, the final wave function of the struck particle is a plane wave. This approximation is not valid if the exchanged wave vector is finite and then the struck nucleus does not strictly recoil as a free particle. So FSE are due to the presence of other atoms around the struck nucleus. This introduces two effects on the NCP: $J(y)$ is not yet symmentric nor centered in $y = 0$. Furthermore the width of the peak and its maximum has an oscillatory dependence on q. This arises from interference effects that are neglected in the IA approximation.

The calculation of the FSE has been done by Sears [24], which in his work represents the corrections as a power series in $1/q$ of the $S(\vec{q},\omega)$:

$$S\left(\vec{q},\omega\right) = \frac{m}{\hbar q}\left[\sum_{n=0}^{\infty}\left(-1\right)^n A_n\left(q\right)\frac{d^n}{dy^n}\right]J\left(y\right)\ , \tag{1.77}$$

where

$$A_n\left(q\right) = \begin{cases} 1, & n=0 \\ 0, & n=1,2 \\ \propto \frac{1}{q}, & n=3 \\ \propto \frac{1}{q^2}, & n=4 \\ \ldots & \end{cases} \tag{1.78}$$

As we can see from equation 1.77, it is possible to write $S(\vec{q},\omega)$ as a sum of a symmetric and antisymmetric parts. For high q values the series quickly converges and the IA improves. Considering only the first two terms of the series:

$$S\left(\vec{q},\omega\right) = \frac{m}{\hbar q}\left[J\left(y\right) - \frac{A_3}{q}\frac{d^3}{dy^3}J\left(y\right) + \frac{A_4}{q^2}\frac{d^4}{dy^4}J\left(y\right) + \ldots\right]\ , \tag{1.79}$$

where the coefficients A_3 and A_4 depend on the shape of the potential in which the struck particle is:

$$A_3 = \frac{M}{36\hbar^2}\left\langle\ \nabla^2 V\right\rangle\ ;\ A_4 = \frac{M^2}{72\hbar^4}\left\langle\left(\nabla V\right)^2\right\rangle\ . \tag{1.80}$$

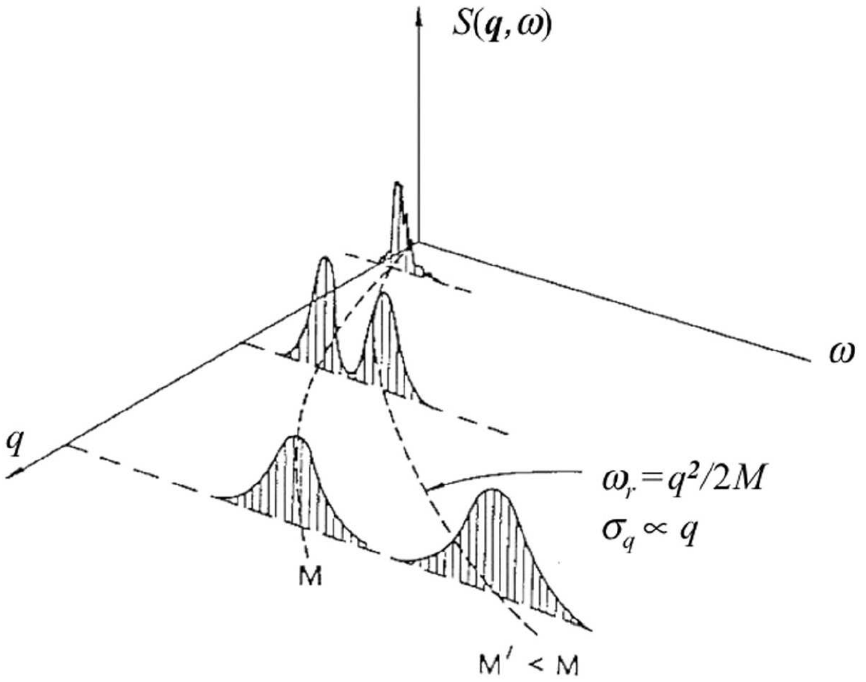

Figure 1.3: *Schematic of the inelastic structure factor as a function of energy and momentum transfer. The neutron scattering, with increasing ω, becomes dominated by: incoherent elastic and Bragg scattering (ω=0), diffusive modes (at very low ω values), collective excitations (placed around low and medium ω), and intramolecular vibrations (medium high ω), while at very high ω (and q) values, the various collective excitations are damped by the Debye Waller factor and the single particle properties alone determine the scattering, which is well described by the IA [53].The two peaks correspond to different atomic masses (M' < M). As q and ω increase the separation between the recoil peaks increases as well.*

1.5.2 Property of the dynamical structure factor in the IA

The properties of $J(y)$ that follow from equations 1.67 and 1.67 when $q \to \infty$ are known in the literature as y scaling. The condition for conservation of momentum and kinetic energy in equation 1.66 links the variables $\vec{q}$ and ω, reducing the number of degrees of freedom by one. The presence or absence of y scaling in the experimental data can be used to test the validity of the impulse approximation. It is useful to recall the properties of $S(\vec{q},\omega)$ in the framework of the y scaling. These follow from the fact that scattering in the impulse approximation is incoherent so that $S(\vec{q},\omega)$ must satisfy the rigorous sum rule [123]:

$$\int S_{IA}\left(\vec{q},\omega\right) d\omega = 1. \tag{1.81}$$

Equation 1.81 follows directly from equation 1.66. The physical interpretation of $J(y)$ as a probability distribution for atomic momenta implies that it is an even function of y with its maximum value at $y = 0$. It follows from equations 1.67 and 1.68 that, at constant q, $S_{IA}(\vec{q}, \omega)$ has its maximum at the recoil frequency ω_r, and is symmetric in ω around ω_r. From equation 1.67 one obtains:

$$\left(\frac{\partial \omega}{\partial y}\right) = \frac{\hbar q}{M}, \tag{1.82}$$

so if the full width half maximum (FWHM) of $J(y)$ is Δy, then the FWHM of $S(\vec{q}, \omega)$, at constant q is: $\Delta\omega = \hbar \Delta y / M$, i.e. the width of $S(\vec{q}, \omega)$, is proportional to q. At a fixed y, the magnitude of the dynamical structure factor is proportional to $1/q$ (from equation 1.68).

The DINS technique results very useful in the case of different atomic masses in the sample. The locus of the recoil peaks in the $S(\vec{q}, \omega)$, at constant q, follows the parabola:

$$\omega = \omega_r\left(q\right) = \frac{\hbar q^2}{2M}. \tag{1.83}$$

So providing the positions ω_{max} of the maxima in $S_{IA}(\vec{q}, \omega)$ determined for different scattering angles, it is possible to plot ω_{max} as a function of q^2: a straight line passing through the origin is obtained, whose slope inversely proportional to the atomic mass (see figure 1.4). This procedure can be used to test for inaccuracies in the IA.

It is interesting to recall a relationship between the initial and the final velocities of the scattered neutrons whose energy and momentum transfers are linked by $\omega = \omega_r(q)$:

$$\alpha = \frac{v_1}{v_0} = \frac{cos\theta + \left[(M/m)^2 - sin^2\theta\right]^{1/2}}{(M/m) + 1}, \tag{1.84}$$

where v_0 is the incident neutron velocity, v_1 the final neutron velocity after the scattering, m is the neutron mass, θ is the scattering angle and M is the nucleus mass. If $M = m$, as in the case of scattering from a proton, this relation reduces to $\alpha = cos2\theta$, so $\alpha = 0$ for $\theta = 90°$. Thus measurements of proton momentum distributions are performed only at forward scattering angles, whereas for $\theta > 90°$, scattering from stationary hydrogen atoms does not occur at all.

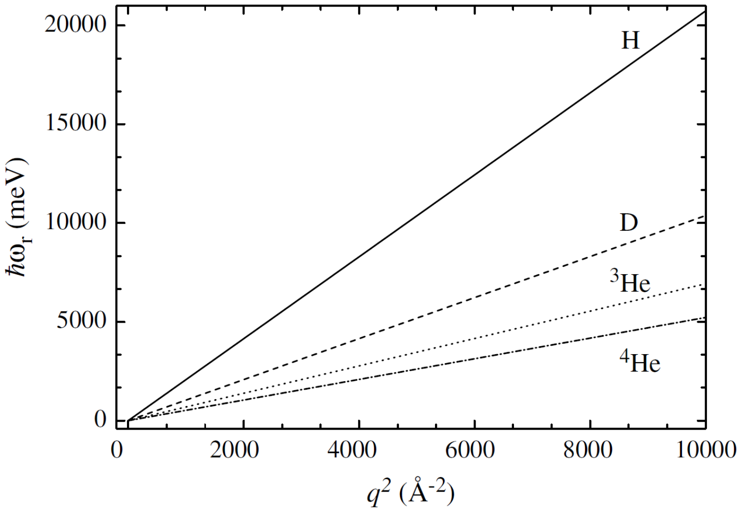

Figure 1.4: *Recoil energy as a function of the squared wave vector transfer for different masses nuclei. Hydrogen recoil energy is well separated by other nuclei's recoil energies, while differences between heavy nuclei decrease as the mass increases. DINS works better with light nuclei [53].*

Chapter 2

Experimental apparatus

In this chapter the experimental apparatus will be described. We used two neutron spectrometers: VESUVIO installed at the ISIS spallation neutron source in Didcot (UK) and SEQUOIA, installed at the Spallation Neutron Source (SNS) of the Oak Ridge National Laboratory (ORNL), Tennessee, USA. VESUVIO has been designed for DINS measurements and it allows to reach the kinematic condition in which the IA holds. Two of the three experiments discussed in this work were done on the VESUVIO spectrometer: the polycristalline ice and the monocrystalline oriented ice DINS measurements. The SEQUOIA spectrometer, where the third experiment was carried out, vibrational spectra of water and ice, is instead devoted to the vibrational neutron spectroscopy, so that the exchanged energy and wave vector are lower with respect to VESUVIO. The main difference between these two spectrometers is in the determination of the neutron final energy: VESUVIO is a time of flight (TOF) inverse geometry spectrometer, while SEQUOIA is a direct geometry TOF spectrometer.

2.1 Neutron sources

Neutrons can be obtained as the result of many reactions that involve heavy atomic nuclei. It could be useful to illustrate some methods to obtain a neutron source:

- production of photo-neutrons from electrons;
- fission;
- spallation.

Photo-neutrons from electrons are obtained from the relaxation of an excited heavy nucleus. The excitation of the nucleus is obtained from the *bremsstrahlung* radiation emitted by the acceleration of the high energy electrons when they interact whit the electromagnetic fields of the nucleus. However, this process is not very efficient because only a small fraction of incoming electrons gives rise to the neutron emission, also providing a huge increase of temperature of the heavy nuclei sample.

Fission is the reaction that produces neutrons into the usual reactors. Nuclear reactor can be used not only to produce energy, but also to produce neutrons with the fission reaction. In the facilities designed for this scope neutrons are usually packed in a pulsed beam.

The spallation process is used at SNS and ISIS and consists in making collide accelerated proton beam on a target made of heavy nuclei. A spallation source presents many advantages with respect to other sources [58]. The dissipated mean power, for example, is very low if compared to the nuclear reactors ($160\,kW$ against tenth of MW of the reactors). Again the mean energy per neutron is about $55\,MeV$, while it is $180\,MeV$ for reactors and $2000\,MeV$ for photo neutron sources.

From an economic point of view one must consider that the proton accelerators are more expensive than the electron accelerators, but the spallation sources are still less expensive than the high flux reactors that can reach the intensity of a spallation source. In this respect major advantages consist in the possibility to perform the TOF and to have a neutron energy spectrum with a larger energy range.

As introduced above a spallation source allows us to obtain neutrons from the collision of high energy protons and a target made of heavy nuclei. The heavy nuclei fragments, produced in the collision, emit many particles, among which there are neutrons. In the case of ISIS the target is tantalum, while at SNS mercury is used. The nuclei are excited in the collision with protons and the relaxation can be divided in two steps: in the first, named *cascade*, high energy neutrons are emitted, in the second, the *evaporation*, neutrinos, pions, protons and other particle are emitted, together with low energy neutrons.

Incident proton beam is produced and accelerated in several steps. Protons are produced starting from the excitation of gaseous hydrogen that produces H^- ions. These are accelerated by an electric potential and introduced in a linear accelerator (LINAC) in which they reach an energy of about $70\,MeV$ in the case of ISIS. At SNS the LINAC accelerates the H^- up to to $1\,GeV$. The LINAC is a superposition of normal conducting and superconducting radio-frequency cavities that accelerate the beam and a magnetic lattice that provides focusing and steering. Three different types of accelerators are used. The first two, the drift-tube LINAC and the coupled-cavity LINAC, are made of copper, operate at room temperature, and accelerate the beam to about $200\,MeV$. The remainder of the acceleration is accomplished by superconducting niobium cavities. These cavities are cooled with liquid helium to an operating temperature of 2 K. Diagnostic elements provide information about the beam current, shape, and timing, as well as other information necessary to ensure that the beam

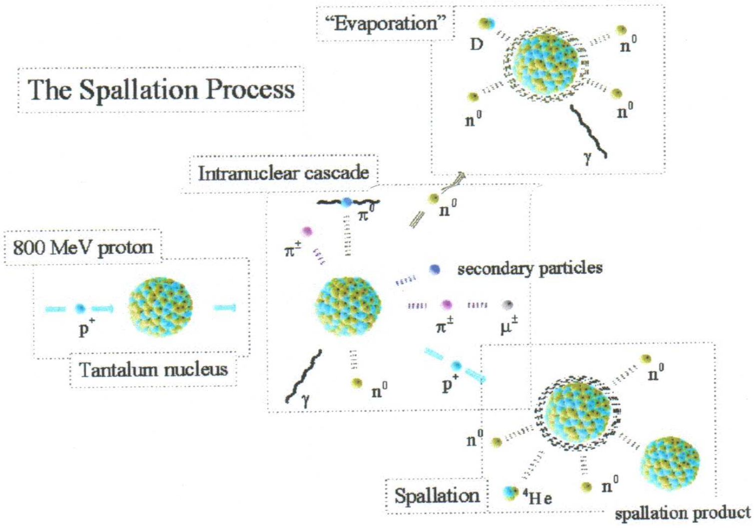

Figure 2.1: *Schematic representation of a spallation process.*

is suitable for injection into the accumulator ring and to allow the high-power beam to be safely controlled .

The accelerated pulse of H^- from the LINAC is wrapped into the ring through a stripper foil (Al, $0.3\,\mu m$ at ISIS) that strips the electrons from the negatively charged hydrogen ions to produce the protons that circulate in the accumulation ring. The protons are further accelerated up to $800\,MeV$ and $2\,GeV$, at ISIS and at SNS, respectively, and packed in a very short bunch which collides with the target, with very short pulses of less than $1\,\mu m$ for both sources. The frequency of the pulses is 50 and 60 Hz, respectively.

At ISIS the *target station* is a set of Ta folis surrounded by a very complex system of neutrons reflectors, moderators and heat absorbers. The neutron production of this target is about 15 neutrons per proton. Moderators slow down fast neutrons up to energy that are useful for neutron spectroscopy (typically from 1 meV up to 100 eV).

At SNS the *target station* is made of Hg atoms that provide 20 to 30 spalled neutrons per incident proton. In the same way, the outgoing neutrons are moderated and guided out of the target vessel into beam guides that lead directly to instrument stations.

The characteristics of a moderator can be chosen to obtain a neutron beam with an optimized energy distribution. In the case of VESUVIO and SEQUOIA an high flux in the epithermal region is desirable.

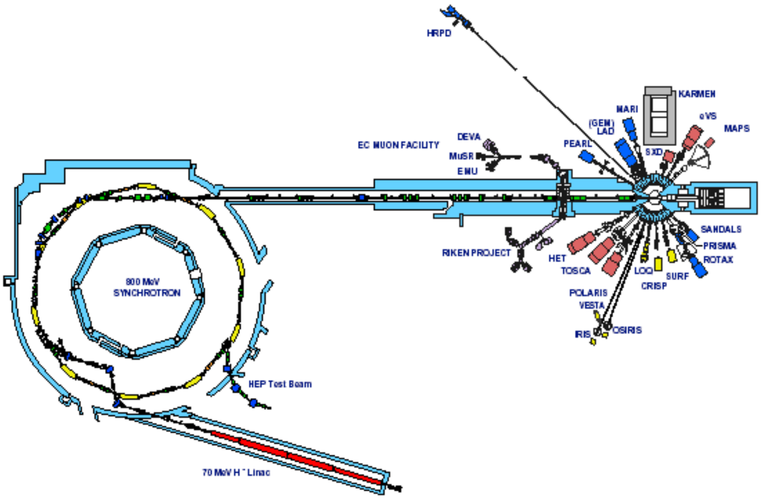

Figure 2.2: *Scheme of ISIS neutron source.*

2.2 Basic principles of the time-of-flight technique

The total neutron Time-Of-Flight (TOF) t is the time spent by a neutron to travel from the moderator to the detector. It can be written as:

$$t = t_0 + \frac{L_0}{v_0} + \frac{L_1}{v_1} \tag{2.1}$$

where t_0 is a fixed electronic time delay, L_0 and L_1 are the incident and scattering flight paths of the instrument, while v_0 and v_1 are the initial and final neutron velocity, respectively. The figure 2.3 represents a schematic drawing of an instrument, where the geometrical parameters are clearly indicated.

In the TOF technique, once L_0, L_1, the scattering angle ϑ and the initial or the final neutron energy (E_0 or E_1) are known, the kinematics of the scattering process can be reconstructed. In practice if we know the initial (final) energy, the total neutron TOF allows for the measurement of the final (initial) one, while the detector$^{\prime}$s angular position (ϑ) allows for the determination of the wave vector transfer, q, as it will be briefly explained in the following.

The TOF acquisition chain can briefly be described as follows: before the proton bunch impinges on the heavy metal spallation target, a proton beam monitor, placed close to the target, triggers the opening of a time gate ($t = t_{start} = 0$) of fixed duration Δt, which

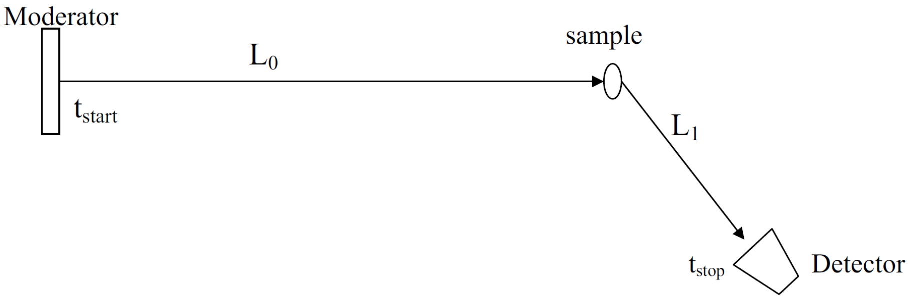

Figure 2.3: *Schematic of an instrument using the TOF technique:* L_0 *is the primary flight path (moderator-sample distance),* L_1 *is the secondary flight path (sample-detector distance). The* t_{start} *and* t_{stop} *are provided by the proton beam monitor and the detectors, respectively.*

depends on the bunch time structure of the source. During Δt the acquisition electronics of an instrument is enabled to process the electric signals provided by neutron detection system (neutron counters). Each signal is stored in a channel of a Time to Digital Converter (TDC), its value being the time difference between the opening of the gate t_{start} (approximatively corresponding to the instant the neutron leaves the moderator) and the detection instant (t_{stop}). A fixed time delay t_0 (see equation 2.1) of about 5 μs is electronically provided, allowing for the recovery of the detectors of all instruments from the saturation induced by the "γ-flash", produced in the spallation process. As we have to deal with a direct and an inverse TOF geometry a brief description of this two geometry is reported in the following.

2.3 Direct and inverse geometry inelastic spectrometers

To reconstruct the kinematics in an inelastic scattering measurement, the initial and final neutron energies (wave vector) have to be calculated. The wave vector, q, and the energy transfer, ω, can be then extracted by using the linear momentum and energy conservation equations:

$$\overrightarrow{q} = \overrightarrow{k_0} - \overrightarrow{k_1}, \tag{2.2}$$

$$\omega = \frac{\hbar^2}{2m}(k_0^2 - k_1^2) = E_0 - E_1, \tag{2.3}$$

k_0 and k_1 being the initial and final neutron wave vectors, and m the neutron mass, respectively. The conservation laws apply rather stringent limitations to the values of q and ω observed. The relation linking q and ω can be found starting from the relation:

$$q^2 = k_0^2 + k_1^2 - 2k_0k_1cos\vartheta, \tag{2.4}$$

or in energy units:

$$\frac{\hbar^2 q^2}{2m} = E_0 + E_1 - 2\sqrt{E_0 E_1} cos\vartheta. \tag{2.5}$$

In the direct geometry configuration E_0 is selected. Thus the equation 2.5 becomes:

$$\frac{\hbar^2 q^2}{2m} = 2E_0 - \hbar\omega - 2\sqrt{E_0(E_0 - \omega)} cos\vartheta. \tag{2.6}$$

For an inverse geometry instrument E_1 is selected and the relation 2.5 becomes:

$$\frac{\hbar^2 q^2}{2m} = 2E_1 + \hbar\omega - 2\sqrt{E_1(E_1 + \omega)} cos\vartheta. \tag{2.7}$$

From a kinematic point of view, the main difference between the direct and inverse configuration is that in the direct geometry the maximum energy loss is limited to E_0, while there is no limit to the energy loss in the inverse geometry. This is clearly observed in figures 2.4 and 2.5, where contour plots of equal scattering angles are plotted as a function of wave vector and energy transfers for fixed initial (figure 2.4) and final (figure 2.5) neutron energy of 6.67 eV.

2.4 VESUVIO

VESUVIO is a TOF inverse geometry spectrometer installed at ISIS neutron source near Didcot (Oxfordshire, UK). VESUVIO is a unique neutron spectrometer because of the high intensity in the eV energy range, and whose pulsed time structure allows for the measurements of momentum distributions in a variety of condensed matter systems.

Energy transfer in the 1-100 eV region and wave vector transfer between 30 and 200 $\AA^{-1}$ are achieved using a filter difference technique. The energy of the scattered neutron is fixed by a nuclear resonance absorption foil and the incident energy (and hence energy and momentum transfers) are determined using the standard time of flight techniques.

Incoming neutrons are slowed down by a water moderator at $T = 295\,K$. The energy spectrum shows a peak at $E = 0.03\,eV$ and an epithermal tail that goes as $E_n^{0.9}$, where E_n is the incident energy (figure 2.6).

Figure 2.7 show a schematic of the spectrometer. In table 2.4 main experimental parameters are reported. As we can see from table 2.4 and from the scheme, VESUVIO uses two banks of detectors that are the forward and backward detectors.

2.4.1 VESUVIO: the resonance detectors

The neutron final energy selection is performed by the absorption of the neutron by an heavy nucleus. In the present case the heavy nucleus is ^{197}Au: a 12.5 μm thickness foil (the *analyzer*

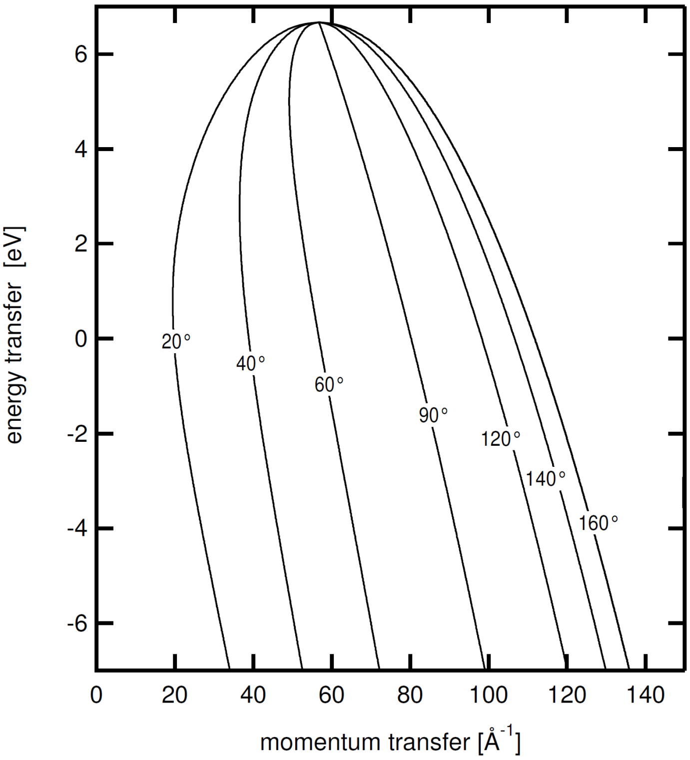

Figure 2.4: *Contour plot of iso-angular loci as a function of wave vector and energy transfers for a direct geometry instrument with E_0 = 6.67 eV. In the direct geometry configuration the maximum energy that a neutron can loss is fixed by the E_0 value.*

foil) is placed in front of the detectors. The absorption cross section has a huge and sharp peak for $4.908\,eV$ neutrons, with an HWHM of $0.144\,eV$ (the cross section is $\sigma(E_r) = 36592\,bn$) [124] with a $10^3 - 10^4$ ratio between non-resonat to resonant energy (see figure 2.8). The process can be described by the formula:

$$A + n \rightarrow (A+1)^* \rightarrow (A+1) + \sum_i^N \gamma_i + K, \tag{2.8}$$

where the nucleus, with atomic number A, absorbs a neutron, is excited and immediately ($\leq 10^{-16}\,s$) relaxes, emitting high energy photons $\sum_i^N \gamma_i$. The last term, K, is the recoil energy of the nucleus, that can be neglected.

The energy range of our interest for the final energy of the neutrons can be restricted from 1 to 100 eV. As we can see from figure 2.8, in this energy range the resonance at $4.908\,eV$ is much larger than the other resonances.

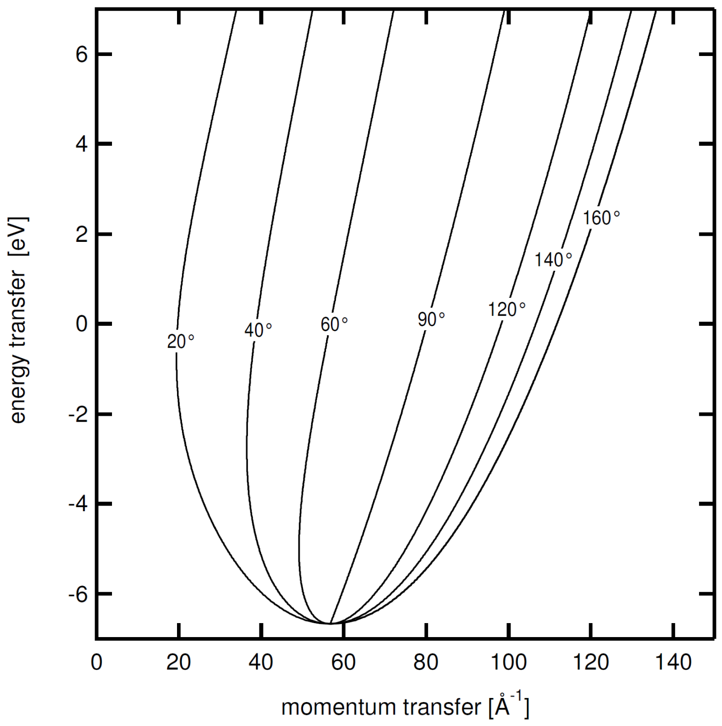

Figure 2.5: *Contour plot of iso-angular loci as a function of wave vector and energy transfers for an inverse geometry instrument with* E_1 *= 6.67 eV. In the inverse geometry configuration the maximum energy that a neutron can loss depends on the maximum energy of the neutrons of the incoming beam. As a consequence the inverse geometry configuration allow us to reach larger values of the exchanged energy with respect to the direct geometry configuration, with the same energy resolution.*

Neutrons with an energy larger than 100 *eV* are less effectively detected, due to the combined effect of low absorption cross section and decreasing neutron flux. The only resonance that could in principle give a peak in the experimental spectra is the 60 *eV* resonance. In all cases however the peak generated by this resonance is not distinguishable over the background or it can be cut off from the spectrum because it appears at very small TOF.

In figure 2.9 the acquisition line is shown. The efficiency in the neutrons detection is a function of the absorption probability of an incoming neutron that hits the analyzer foil and of the efficiency of the γ detectors. The absorption probability is proportional to the thickness of the analyzer foil, that should be chosen comparable to the mean free path of a neutron, to minimize the absorption probability of a neutron with energy far from the resonance. With the present configuration the total efficiency is about 0.63.

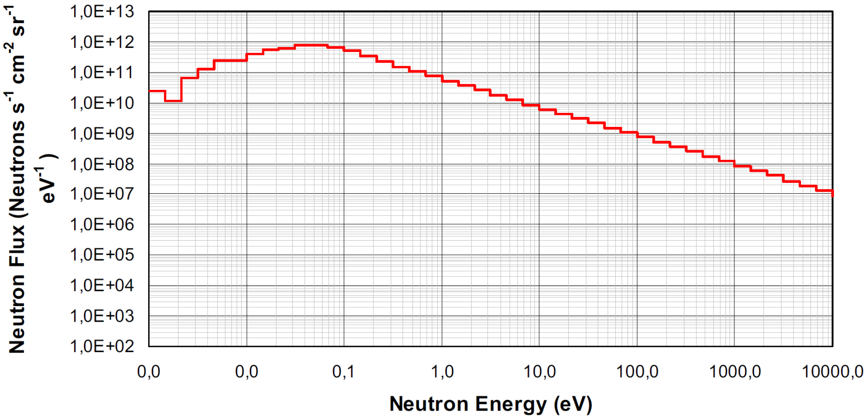

Figure 2.6: *Neutron flux at VESUVIO.*

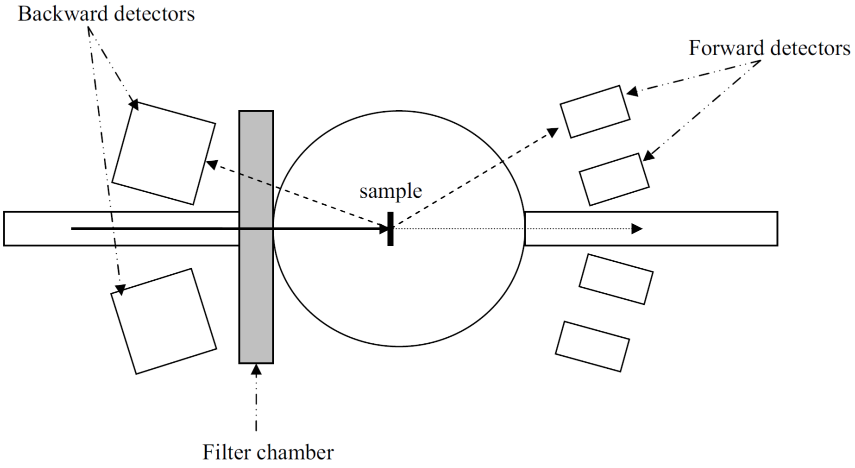

Figure 2.7: *Schematic of VESUVIO.*

Geometric configuration	Inverse
Neutron energy selection	Nuclear Resonance
Detectors	YAP scintillators
L_0	$11.055\,m$
L_1	$\approx 0.6\,m$
Angular range(forward)	30°-70°
Angular range (backward)	120°-170°
Available (q, ω) region	$q \geq 30\,\AA^{-1}$, $\omega \geq 1eV$

Table 2.1: *Experimental parameters of VESUVIO.*

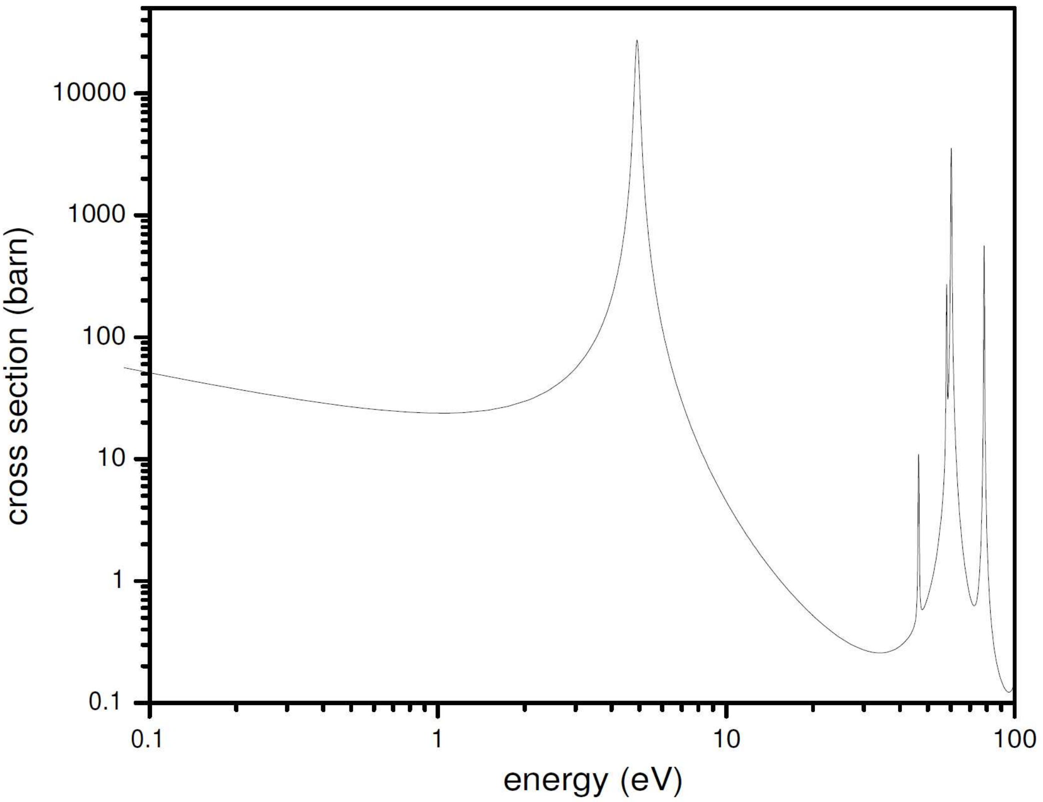

Figure 2.8: ^{197}Au *absorption cross section. The intensity of the resonance at 4.908 eV is much larger than other resonances in the energy range of our interest (the intensities are in logarithmic scale).*

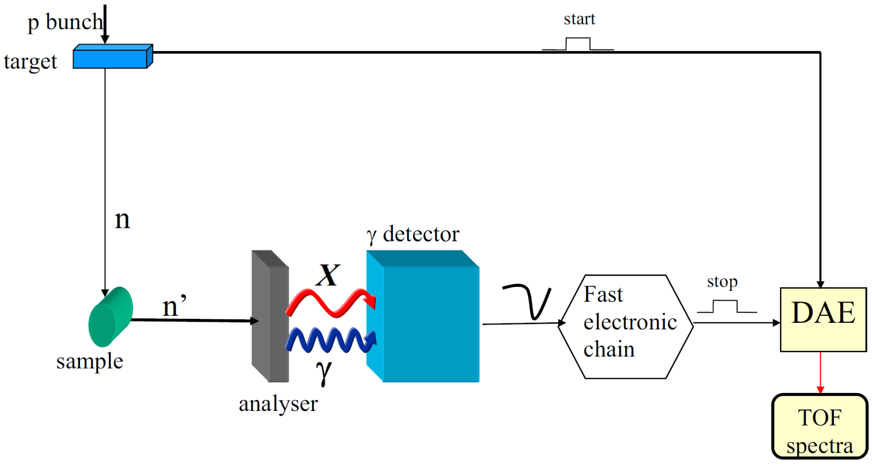

Figure 2.9: *Schematic of the data acquisition with the resonance detectors: a neutron impinges on the detector an it can be absorbed by the analyzer foil. The absorption produces a γ rays that is detected by the scintillator.*

The condition for the detection of a neutron is then the detection of a γ photon that releases part of its energy in the scintillator. The photon detection generates an electric signal that is processed by the fast electronic chain, emitting another signal that stops the acquisition. This stop signal is generated with a time lapse that is negligible (shorter than 1 μs) with respect to the absorption of the neutron.

The γ detectors should not have neutron capture resonances in an energy interval between 1 and 100 eV, otherwise they would became gamma emitters, producing a wrong neutron count. In this work we used the YAP (Ittrio-Allumino-Perovskite) scintillators as γ detectors. The scintillators are materials that can absorb high energy radiation, remitting them as visible light after a decay time t_d. YAP are very fast scintillators (t_d is very short), they have a good mechanical and chemical resistance, they are not hygroscopic, they have a glassy structure with a high density (5.55 gcm^{-3}) but low atomic number (Z=36) and they posses the crucial feature for a scintillator: they are transparent to the visible light. The material is also stable in a wide range of temperatures. Main features of YAP are reported in table 2.4.1.

VESUVIO is equipped by 64 detectors in forward scattering, disposed in an angular range between 33° and 72° with respect to the incoming neutron direction. Detectors are mounted in 8 columns, each of which mounts 8 detectors (see figure 2.10).

2.4.2 FCT: Foil Cycling Technique

To increase the energy resolution, the acquisition is done with a gold foil between the sample and the detectors that works as band cut filter [85]. The width of the J(y) has two con-

Atomic Number	36
Density	5.55 gcm^{-3}
λ of maximum emission	350 nm
Refraction index ($\lambda = 350nm$)	1.94
Light production	18000 $photons/MeV$
Time of decay	27 ns
Hygroscopic	no

Table 2.2: *Main features of a YAP scintillator.*

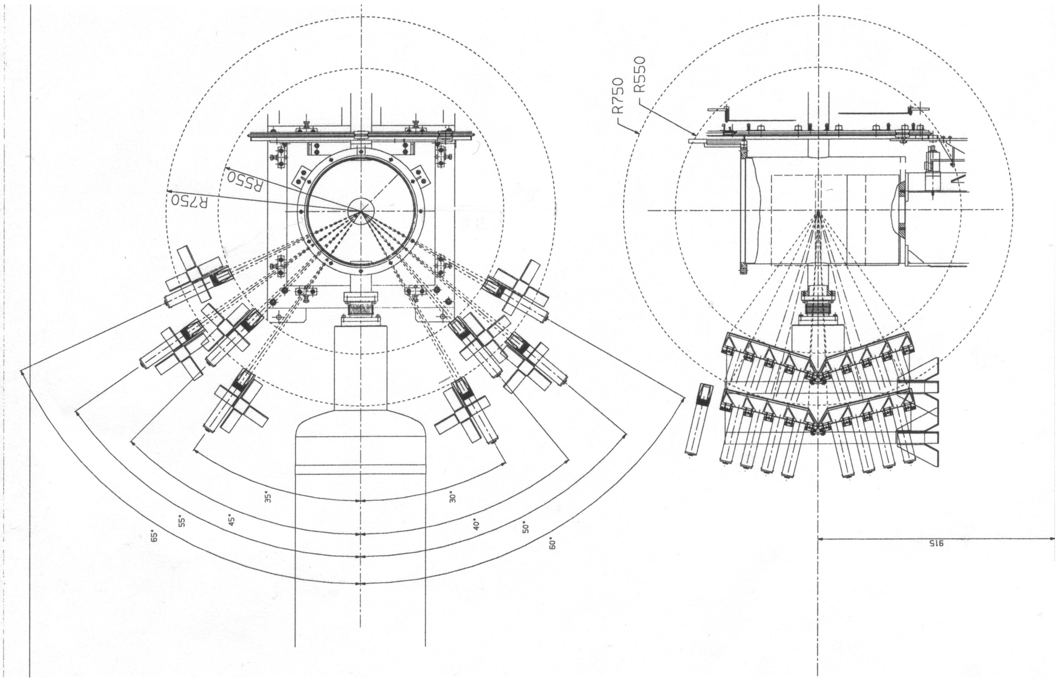

Figure 2.10: *Design of the experimental chamber. Plan(left) and side view (right).*

tributions: one is intrinsic and related to the $n(p)$ of the target particle, the other is the instrumental resolution. In the chapter dedicated to the data analysis we will compare the result of the proton mean kinetic energy obtained by a numerical derivation (with no correction to the instrumental resolution) and by a fitting procedure that takes into account the resolution.

The data produced by the VESUVIO spectrometer is then obtained by taking differences among spectra produced with gold foils in different positions. The foil changers are also illustrated in figure 2.11

By the use of a secondary foil placed in two suitable positions, the energy resolution can be much improved and the background almost eliminated. This method, named *Foil Cycling Technique* (FCT), is illustrated in Figure 2.12

The data acquisition with the FCT can be described in two steps: in the first step an acquisition is done with the secondary foil interposed between the sample and the detectors while in the second step an acquisition is done without the secondary foil. The final spectrum is obtained then by the subtraction of the spectrum without the foil and the spectrum obtained with the foil.

The improvement of the instrumental energy resolution can be explained as follows: let us call d the thickness of the primary and secondary gold foil, then the transfer function of the neutron beam in the foil out position can be expressed as:

$$T_{out} = 1 \, - \, e^{-N\sigma_y(E)\,d}, \tag{2.9}$$

where $\sigma_y(E)$ is the neutron capture cross section as a function of the energy and N is the number of absorbing nuclei per unit volume. The transfer function for the neutron beam passing through the secondary foil is:

$$T_{filter} = e^{-N\sigma_T(E)\,d}, \tag{2.10}$$

where $\sigma_T(E)$ is the total cross section that takes into account all the physical processes that remove a neutron from the beam. So when the secondary foil is interposed the transfer function can be calculated from the equation 2.9 times equation 2.10:

$$T_{in}(E) = e^{-N\sigma_T(E)\,d}\left(1 - e^{-N\sigma_y(E)\,d}\right). \tag{2.11}$$

From the difference spectrum in the two foil positions, one obtains an effective transfer function that can be expressed as follows:

$$T(E) = \left(1 - e^{-N\sigma_y(E)\,d}\right)\left(1 - e^{-N\sigma_T(E)\,d}\right). \tag{2.12}$$

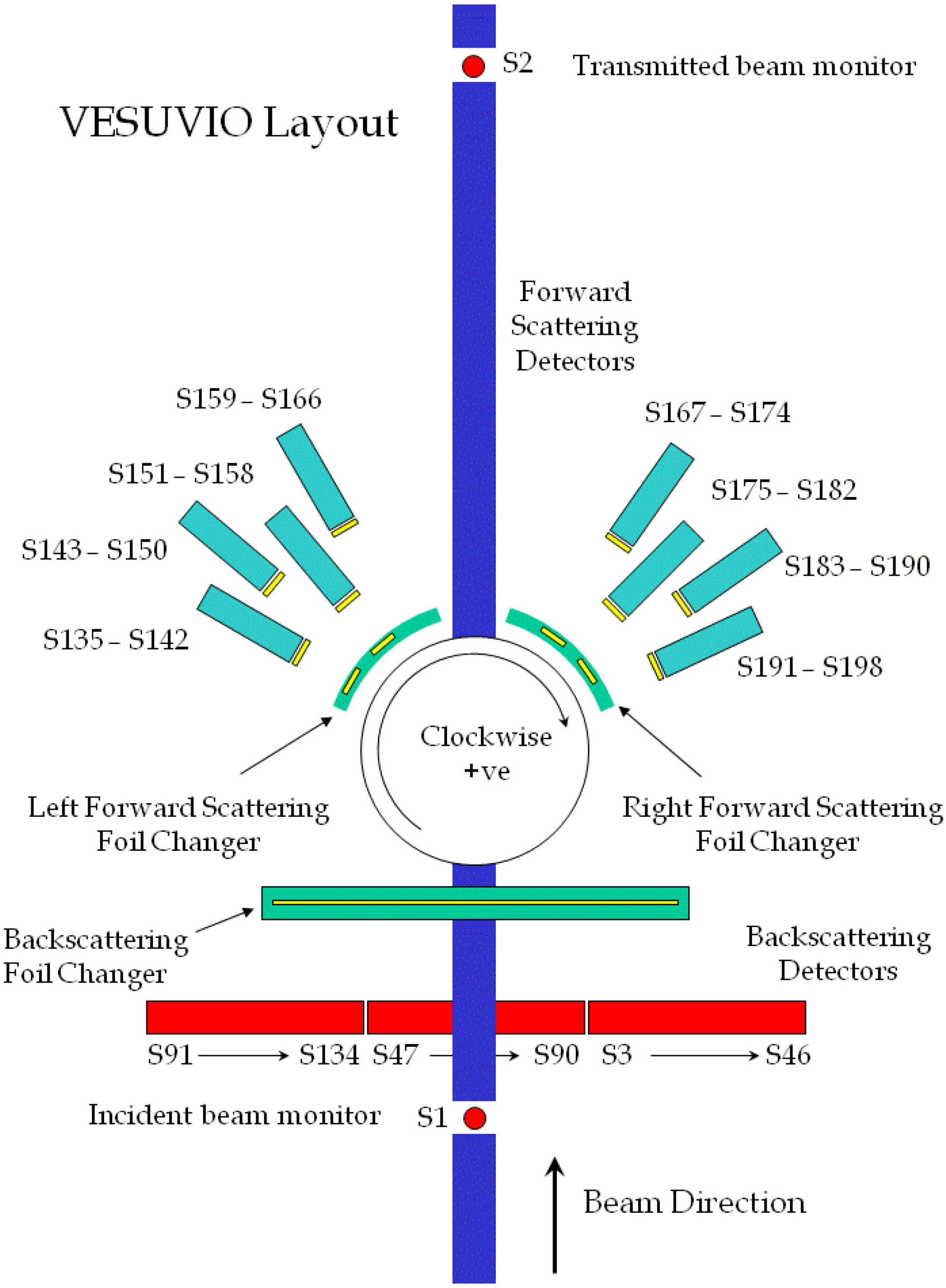

Figure 2.11: *VESUVIO layout.*

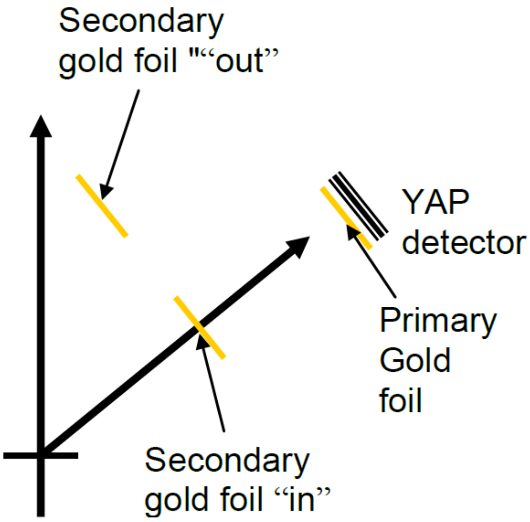

Figure 2.12: *Foil cycling method used on VESUVIO. There is a primary gold foil fixed on the surface of the YAP detector and a movable secondary gold foil of identical thickness. The secondary foils are cycled, that is moved many times between the two positions within a data collection period. The cycling removes drifts in detector efficiency with time, due for example to ambient temperature changes.*

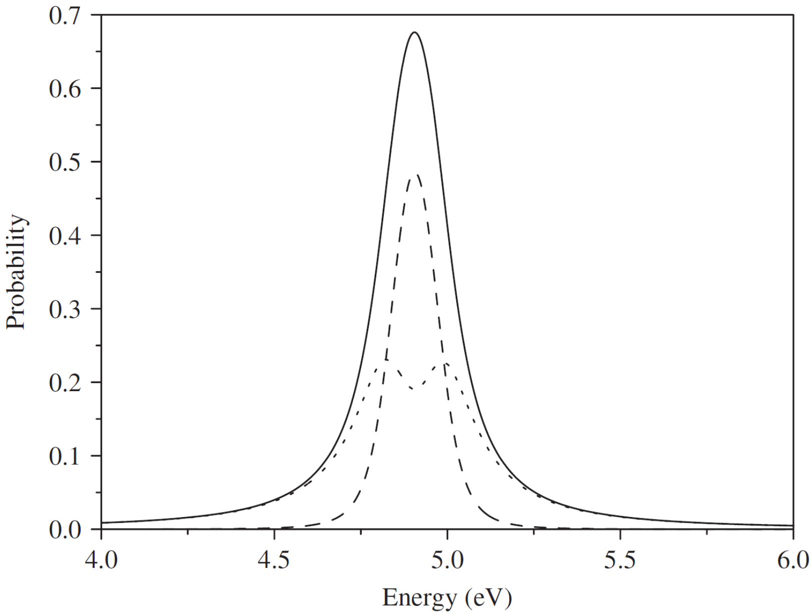

Figure 2.13: *Calculated transfer function with a secondary foil* 12.5 μm *thik. Continuous line is the transfer function of the foil out mode, dotted line is the transfer function of the foil in mode and the dashed line is their difference.*

Considering that the total cross section around the capture resonance is almost equal to the neutron capture cross section we can put $\sigma_T(E) \approx \sigma_y(E)$ obtaining:

$$T(E) \approx \left(1 - e^{-N\sigma_y(E)\,d}\right)^2 . \tag{2.13}$$

So with a very good approximation the final transfer function with the FCT is the square of the transfer function without the secondary foil. For a Gaussian shape of the transfer function we would obtain a FWHM that is smaller by a factor 0.71. Calculations shows that the real improvement of the resolution is about 0.74 and this effect gives rise to a loss of intensity of the resonance peak of only 10 % [85].

The improvement of the resolution is not the only effect of the FCT. In any neutron spectrometer there is a non negligible amount of background caused by other products of the spallation process or by the interaction of the neutron with the infrastructure of the experimental hall. Moreover in the present case YAP detectors are used, that reveal γ rays, a very important part of the natural background. On the other hand we can consider the background as a noise with a constant value in time. In that case the subtraction of the two spectra will also produce a complete background removal.

2.5 SEQUOIA

SEQUOIA is a fine resolution thermal - epithermal spectrometer located on the beamline 17 at the SNS of the Oak Ridge National Laboratory in Oak Ridge, Tennessee (USA). Figure 2.14 shows the overall layout of the spectrometer and points out major components many of which will be here described. In table 2.3 distances to major instrument components are given.

SEQUOIA is a direct geometry time-of-flight chopper spectrometer that can utilize incident neutron energies E_i ranging from 10 meV and 2 eV. The output of the moderator, ambient water poisoned with Gd, is shown in figure 2.15. The SEQUOIA spectrometer enables very high-resolution inelastic neutron scattering studies of magnetic excitations and fluctuations and lattice vibrations and has been also used to conduct forefront research on dynamical processes in materials. With its capability to acquire data quickly and relate them to three-dimensional momentum transfers, SEQUOIA applications span a wide cross-section of important research areas in condensed matter and materials.

2.5.1 Choppers

The energy selection on SEQUOIA is done by choppers, that are rotating particle velocity selectors. On SEQUOIA two choppers can be used in series, the T_0 chopper together with

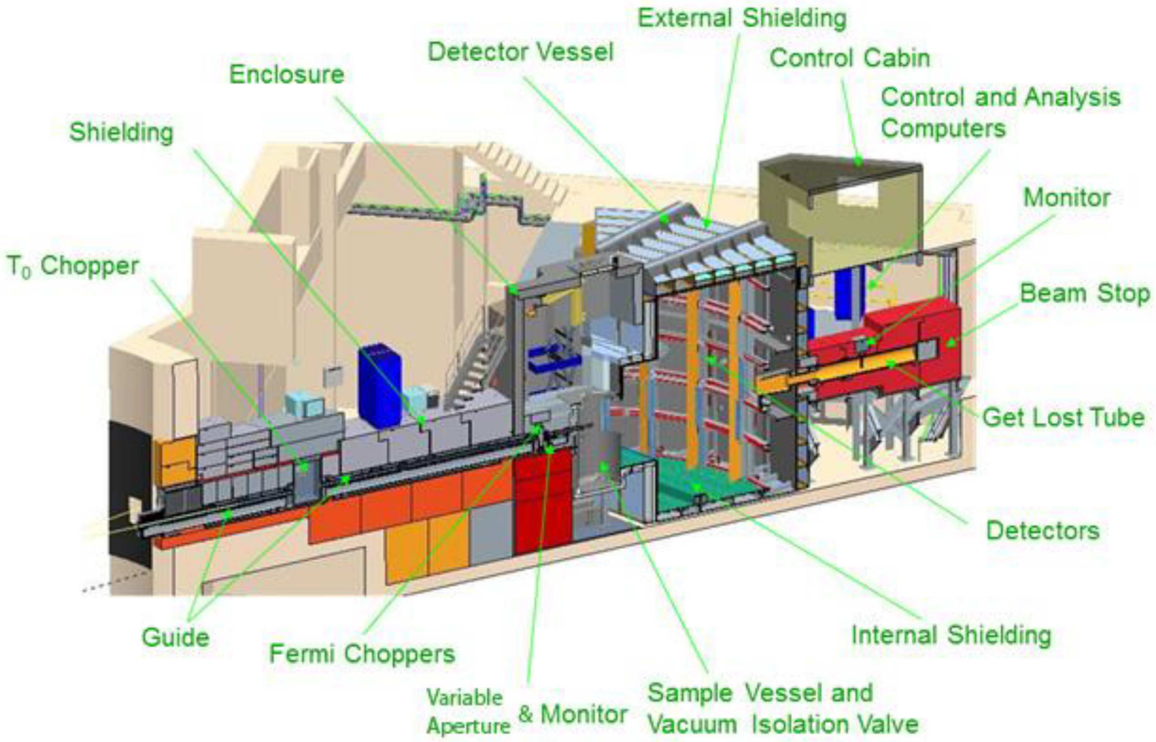

Figure 2.14: *Schematic view of the SEQUOIA spectrometer indicating all of the major instrument components.*

Description	Distance (m)
Moderator to T0 chopper	9.5
Moderator to Fermi chopper	18.2
Moderator to Monitor 1	18.2
Moderator to Sample	20.0
Sample to horizontal plane detector pixels	5.5
Moderator to Monitor 2	29.0

Table 2.3: *Distances to major instrument components.*

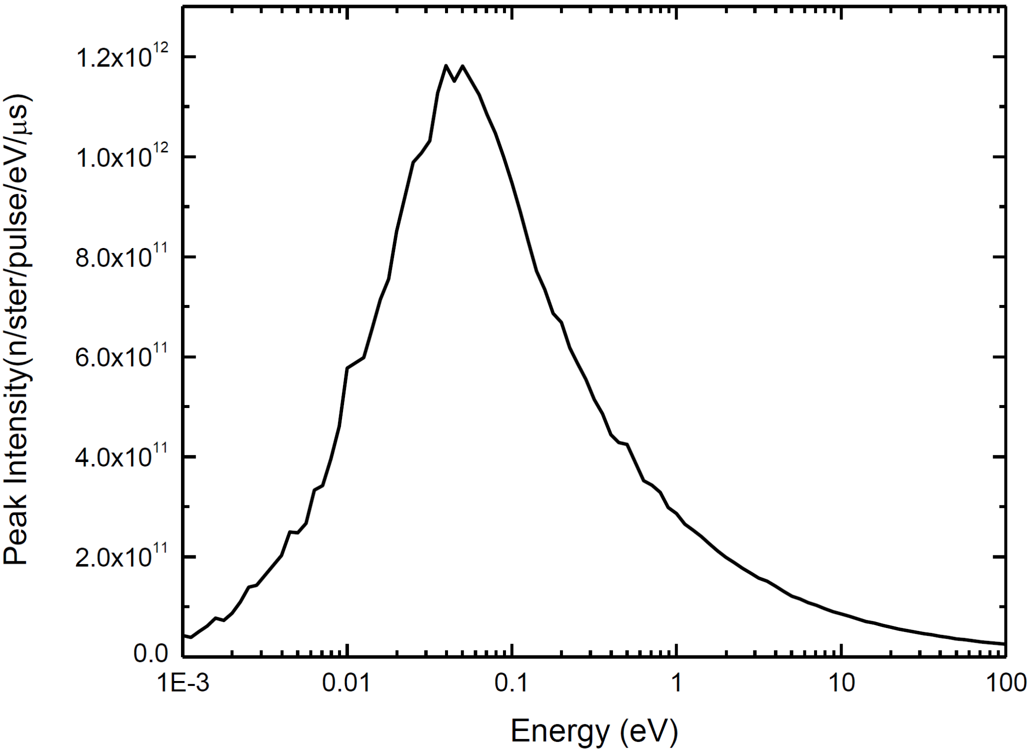

Figure 2.15: *Output of the moderator, as a function of energy, at the SEQUOIA spectrometer.*

the Fermi chopper 1 or 2. The Fermi Choppers are mounted on a translator table that can put either Fermi chopper 1 or 2 into the beam or neither (for white beam configuration).

The purpose of the T0 chopper, which is located at 9.861 m from the moderator, is to suppress the prompt pulse of fast neutrons produced when the proton beam strikes the target. This suppression is accomplished by having an approximately 0.20 m thick piece of the alloy Inconel X-718 in the beam when the proton pulse hits the target. The material works by scattering neutrons into the neighboring shielding. This piece of inconel must be out of the beam in sufficient time for the 0.01 - 2 eV neutrons to pass. It only turns counter clockwise and can operate at rotational speeds between 30 Hz and 180 Hz in multiples of 30 Hz. So the T0 chopper transmits a much wider bandwidth than the Fermi choppers.

The Fermi choppers are mounted 18.0085 m from the moderator. Its purpose is to select a monochromatic pulse of neutrons. A Fermi chopper is a series of closely spaced neutron-absorbing blades (slit package) held together by a rotor that spins about a vertical axis in the path of the beam. All slit packages are 100 mm in length. Each Fermi Chopper can be spun from 0 to 600 Hz in increments of 60 Hz. Only one Fermi chopper may be spinning at full speed at a time. Figure 2.16 and Figure 2.17 provide the resolution and transmission for the two Fermi choppers for the elastic peak.

2.5.2 Detectors

The final energy selection is performed with the TOF technique that has been previously described. In this way, knowing the position of each detectors we can determine all the kinematic of each revealed neutron.

The detector array on SEQUOIA is an assembly of 1.2 m long by 25 mm diameter Linear Position Sensitive Detectors (LPSDs). The array is formed by 1440 detectors grouped into packs of 8 and located on a vertical cylinder with a radius of $\approx 5.5\ m$ (which is the distance between the sample position and the detectors in the horizontal plane). The LPSDs are filled with ^3He at a pressure of 1.0 MPa. To reduce background there is no window between the sample and the detectors; the detectors are located inside a detector chamber that is evacuated to a high vacuum (below 10-6 atm) and is contiguous with the sample vessel.

An incoming neutron is converted through the nuclear reaction

$$n +^3 He \rightarrow^3 H +^1 H + 0.76\ MeV \tag{2.14}$$

into charged particles tritium (T or ^3H) and protium (p or ^1H) which then are detected by creating a charge cloud in the stopping surrounding gas. The electrons from the ionized gas are collected at an anode wire running down the center of the detector tube. This wire is at 1870 V above ground and has a high resistance so the proportion of charge seen at each

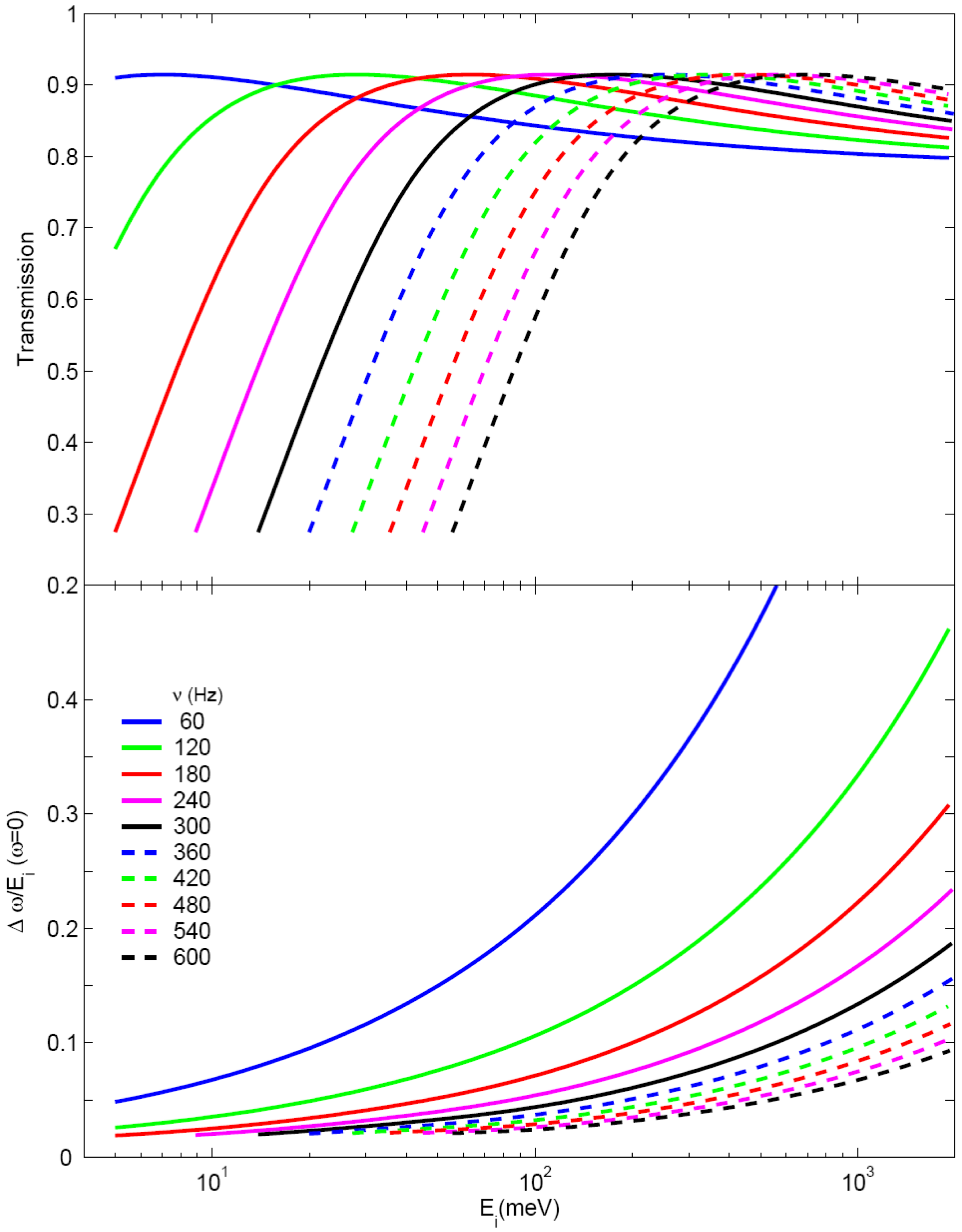

Figure 2.16: *Transmission coefficient through the slit package and elastic energy resolution for the Fermi chopper 1 as a function of the incoming neutrons energy, upper and lower panel, respectively.*

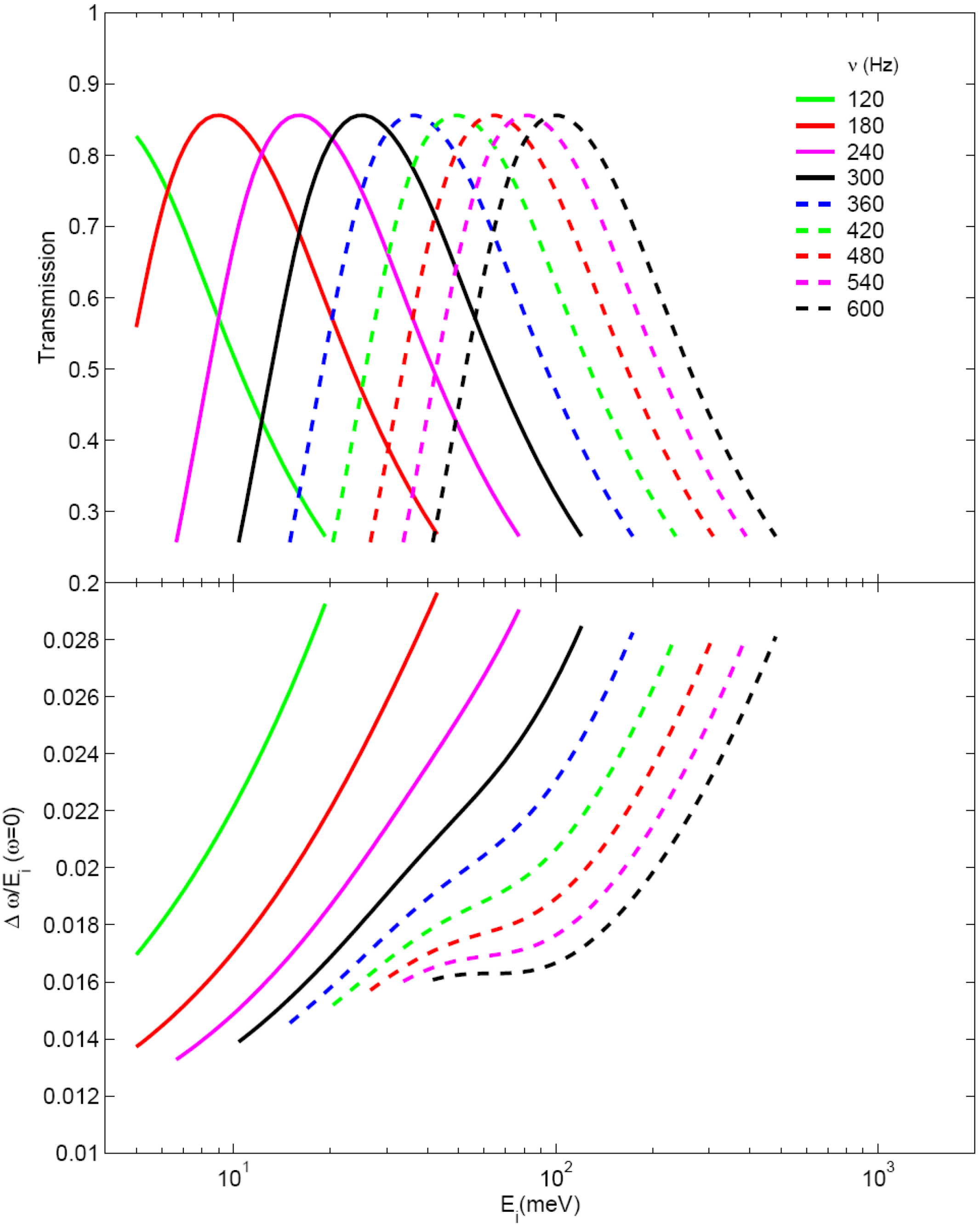

Figure 2.17: *Transmission coefficient through the slit package and elastic energy resolution for the Fermi chopper 2 as a function of the incoming neutrons energy, upper and lower panel, respectively.*

end allows one to determine the position of the neutron detection event. The length of the detectors is divided into 128 pixels of ≈ 10 mm length by the electronics. Each pixel subtends an angle of $\approx 0.26°$ perpendicular to the length of the tube and $\approx 0.16°$ along the length of the tube. Each pixel has a timing resolution of 1 μs and saturates at no less than 70,000 n/s. After saturation a tube is ready for measurement within 10 μs. Saturation is indicated by lack of response, even if the signal is increased. In extreme saturation cases the charge cloud grows up and down the tube and position sensitivity is lost as well.

The efficiency of a ^3He detector is not constant with the energy of the incoming neutron: it varies as $1/\sqrt{E}$. When an inelastic neutron experiment is performed one must take into account for the relative variation of the intensity of spectrum at different energy due to the energy dependence of the efficiency. For this purpose at the beginning of each experiment a V sample, irradiated with a white beam, is measured to calibrate the detectors response and to accordingly correct the data.

2.5.3 Monitors

There are two neutron beam monitors located along the direct beam, one located just downstream of the Fermi chopper and variable aperture and a second located farther downstream of the sample near the beamstop.

The positions of each monitor with respect to the moderator are 18.2331 m and 29.0033 m, respectively. If the upstream monitor has been removed an remounted, a new position is recorded.

These two monitors are primarily used to determine the speed of the incident neutrons, but can also be used to normalize the intensity. The detection media is ^3He, just as in the detectors. However they have a relatively low gas pressure to detect a small portion of neutrons without saturating. More specifically their detection efficiency is 10^{-6} for $E_i = 2$ eV of the neutrons. The detection area is 76.2 mm wide by 114.3 mm high and 12.7 mm deep. The gas is contained in an Al box. Both the incoming and outgoing windows are 1.3 mm thick.

Chapter 3

Data analysis: DINS on polycristalline ice

In the fist chapter the equations relating the cross section to the physical quantities of our interest have been derived. As already described, DINS allows us to extract momentum distribution and mean kinetic energy of protons in ice.

In that discussion an ideal situation has been analyzed: a neutron impinges on the sample, interacts once and then is revealed. In the real case one has to consider that the probability of a neutron to interact more than once and then to be revealed is not negligible. These kind of events, named *Multiple Scattering* (MS) events, give rise to a measured cross section that differs from that we want to examine to extract the $F(y)$ function and then the physical quantities to be studied. The multiple scattering is not the only contribution to the experimental data that we have to subtract: in the TOF spectra recoil peaks appears due to other masses of the sample (O of the water and Al of the can) and the instrumental resolution has to be considered as well.

The DINS data analysis is not trivial and require a particular attention to obtain reliable physical results. The following steps of the data analysis and reduction will be described in this chapter:

1. Background correction;

2. Subtraction of multiple scattering;

3. Subtraction of unwanted recoil peaks;

4. Rescaling of TOF data to the West variable y and normalization;

5. MC simulation for calculation of the instrumental resolution of each detectors.

This procedure is standard for a DINS experiment and permits to obtain the NCP for each detector $F_l(y, \vec{q})$. The routines for this analysis are also provided by the VESUVIO staff, however, new routines have been implemented in order to better control the data analysis. Matlab and Fortran have been used for the data analysis [81]. The important innovation in the DINS data analysis, introduced in this work regards the derivations of $\langle E_k \rangle$ and $n(p)$. In previous experiments the overall NCP $F(y)$ was expressed as a Gaussian times a polynomial expansion representing a complete basis in the 1-variable functions space. No physical model was used to obtain this expression and as a consequence the interpretation of the results was very difficult. We will use in this chapter a physical model that consists in writing the measured $n(p)$ in the spherical average of three Gaussian momentum distributions. In this way the anisotropy of the system can be easily pointed out. This is not the fist time the anisotropic Gaussian model is used to model the $n(p)$ [125], however, it is the first time that the parameters are derived a using prior knowledge from a recent and accurate simulation [126].

Furthermore another physical quantity has been derived: the mean force that is much more sensitive to the anisotropy of the system and it is computable directly from row $F(y)$ [3].

In this chapter we will describe in detail all the data analysis of the experiment on the polycristalline ice at T = 271 K, performed with the VESUVIO spectrometer.

3.1 Background correction

As discussed previously, the FCT should completely remove the background. However, the secondary foil could generate a background as well. This background arises from the different positions of the secondary foil with respect to the detectors. When the secondary foil removes a neutron from the beam, capturing it, it emits γ rays isotropically. This emission gives a contribution to the background and can be subtracted when the subtraction (between the foil in and foil out spectra) is performed. However, from the point of view of a single detector this background is not the same when the secondary foil moves from one position to another, because the solid angle subtended from a generic point of the foil to the detector changes. This effect was in fact evident, and absolutely not negligible, in the previous hardware setting of the spectrometer. The secondary foil was a unique big foil moving in such a way that the detectors above the horizontal plane passing through the sample was in the foil in condition while the detectors under such plane was not and vice versa. In November 2009, the hardware setting was changed to the present one, described in the previous chapter, and a routine for the correction of data taken before that time was provided by the VESUVIO staff.

The routine is still available, but this hardware setting strongly reduce the γ background so that any correction due to the background is negligible. We have to point out the fact that only 48 out of the 64 forward scattering detectors seem to work correctly. The remaining 16 are those mounted on one side of the angular range of detection. This let us think that a geometrical factor related to the background is responsible of this behavior but the complete motivation is unknown. For this reason we will only consider 48 detectors and we shall not attempt a correction of the background of the remaining 16.

3.2 Multiple scattering subtraction

A Monte Carlo (MC) simulation has been implemented to subtract the multiple scattering contribution. The simulation reproduces the scattering event with the atomic mass of the sample. The features of the simulation can be summarized as follows:

- A neutron is created with random incident energy;
- The incoming neutron can interact with the sample from 0 to 3 times;
- The final energy selection is simulated taking into account the transfer function obtained from the capture cross section of Au (see equation 2.12);
- The sample has no structure: the atomic masses in the sample (H, O, Al) are distributed randomly in the sample volume and are free particles;
- The momentum distribution of the atomic masses is Gaussian;
- Simulation takes into account the instrumental resolution;
- $1.5 * 10^9$ events are computed for each detector.

The simulation generates two spectra for each detector: a spectrum with the single scattering events and a spectrum with all the scattering events. The difference of this two spectra is then the multiple scattering contribution that has to be subtracted.

For each atomic mass the information needed are: number of atoms, mass, cross section and standard deviation of $J(y)$. As usual, the mass value determines the position of the recoil peak, the standard deviation its width and the cross section and the number of atoms its intensity. These parameters were adjusted until the simulation reproduces as best as possible the experimental data.

Only double and triple scattering events are accounted for. The sample is thin enough to yield a negligible contribution for higher order scattering events. For our purpose, even the triple scattering event could be neglected, but it has been considered because the additional computational time was negligible too.

As expected, the main contribution to the multiple scattering arises from the hydrogen atoms. The proton has a cross section that is ≈ 20 times the cross section of the oxygen and ≈ 50 times the Al. In figure 3.1 the MS subtraction for two spectra at 61° and 42° scattering angles is shown.

The same MC simulation has been used to calculate, for each scattering angle, the instrumental resolution. Instead of the atomic mass of the sample, the simulation has been done with an ideal sample composed by H atoms only, with the momenta set to zero. By doing so the width of the recoil peak we obtained, is entirely due to the instrumental resolution. The MC has been previously tested with calibrating measurements on a Pb sample, that produces a recoil peak whose width is entirely due to the instrumental resolution.

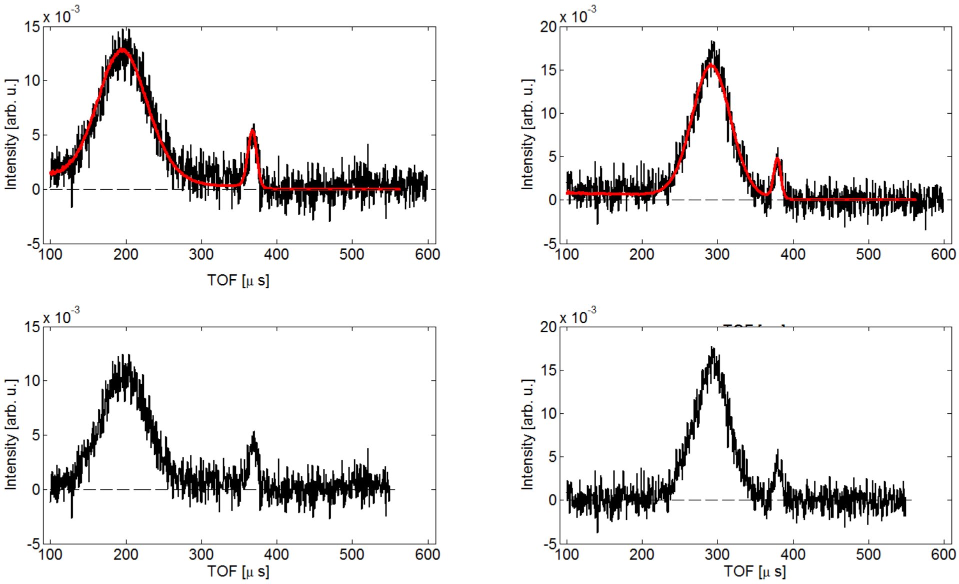

Figure 3.1: *Two experimental spectra corresponding to 61° and 42° scattering angles, left and right plots, before and after the MS subtraction, upper and lower plots, respectively. The black lines are the experimental data, the red lines are the simulations.*

3.3 Subtraction of O and Al recoil peaks

The next step in the data reduction is the subtraction of the O and Al recoil peaks to obtain TOF spectra in which only the hydrogen recoil appears. In this step, the features of DINS spectra are crucial because the recoil peaks are centered at different time of flights as a function of the mass. The *Al* and *O* peaks are well separated from the *H* peak. Only for smaller scattering angle the heavy masses peaks appear on the tail of the hydrogen but this does not prevent the subtraction.

Al and *O* peaks are superimposed and appear as a unique peak at all the scattering angles. For our purpose we can however treat them as a unique peak. A Fortran code has been implemented to fit this peak with a function that is the convolution of a Gaussian and a Lorentzian functions, i.e. a Voigt profile [127]:

$$V(x,\sigma,\gamma) = \int_{-\infty}^{+\infty} G(x',\sigma) L(x-x',\gamma) dx', \tag{3.1}$$

with

$$G(x,\sigma) = \frac{1}{\sqrt{2\pi}\sigma} \exp \frac{-x^2}{2\sigma^2} \tag{3.2}$$

and

$$L(x,\gamma) = \frac{\gamma}{\pi(x^2+\gamma^2)}. \tag{3.3}$$

The input parameters are the position of the peak and the range of calculation for the minimization are given by graphical input, with the use of a Matlab code, for each peak of each spectra (the hydrogen peak is fitted too, with the same fitting function, to distinguish it from the *Al-O* peak, when they are partially superimposed).

As an example, in figure 3.2 and 3.3 the result of the fit for two spectra, corresponding at 66° and 32° scattering angles, respectively, are reported.

3.4 y transform

So far in the dynamical structure factors only the hydrogen recoil peak appears. The relation that relates ω to y is that reported in chapter 1, the 1.67, that we report below:

$$y = \frac{M}{\hbar^2 q} \left(\hbar\omega - \hbar\omega_r\right). \tag{3.4}$$

The wave vector transfer, q, varies as a function of the time of flight of the neutron. If the final energy is fixed, the TOF is inversely proportional to the square root of initial energy ($t \propto 1/\sqrt{E}$) and the relation between q and ω is given by:

$$\frac{\hbar^2 q^2}{2m} = 2E_1 + \hbar\omega - 2\sqrt{E_1\left(E_1+\hbar\omega\right)} cos\vartheta \tag{3.5}$$

For each detector and for each TOF we have a different wave vector transfer that is larger, for shorter times of flight and larger scattering angles.

In figure 3.4 and 3.5 two $F_l(y,\vec{q})$ spectra for 45° and 60° scattering angles, are reported. In both of them we can see that the tail at positive y have larger error bars. This is a feature

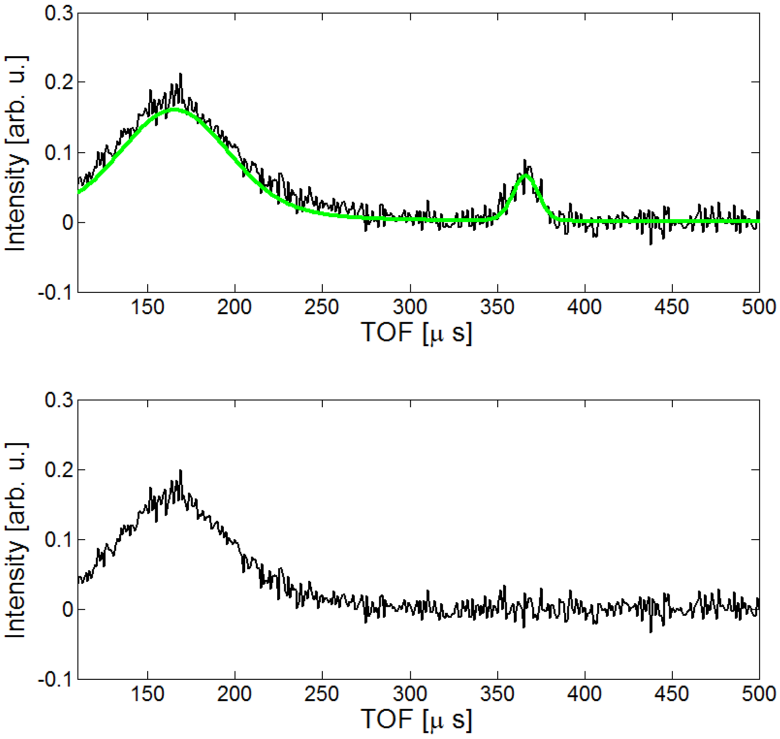

Figure 3.2: *Subtraction of Al-O recoil peak in a TOF spectrum at 66° scattering angle. Black and green lines are the experimental data and the fit, respectively.*

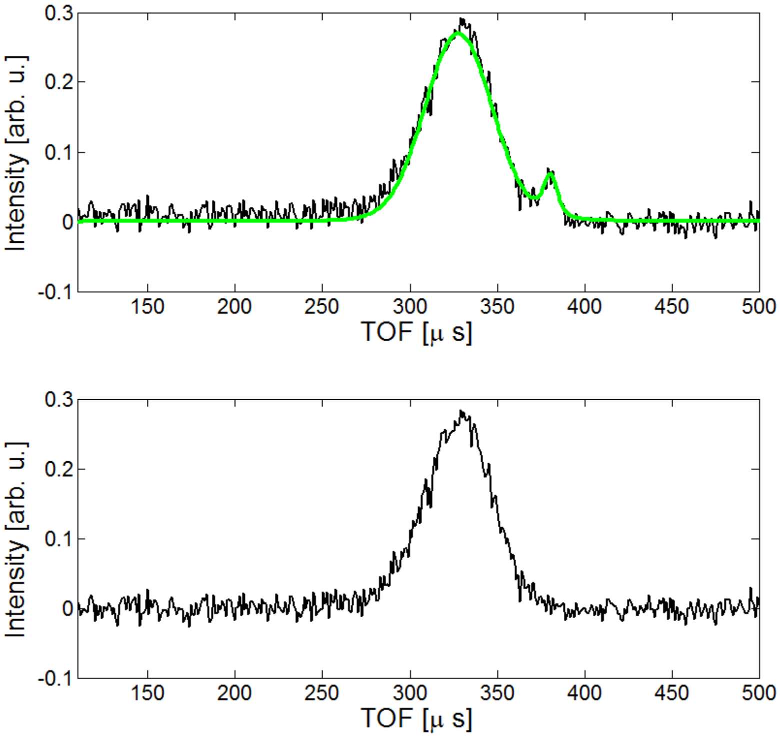

Figure 3.3: *Subtraction of Al-O recoil peak in a TOF spectrum at 32° scattering angle. Black and green lines are the experimental data and the fit, respectively. This is the lowest angle scattering at VESUVIO spectrometer. The H and Al+O recoil peaks are partially superimposed. As a consequence, a fit of the H peak is needed as well, to correctly subtract unwanted recoil peaks. Even at the lowest scattering angle the subtraction can be performed.*

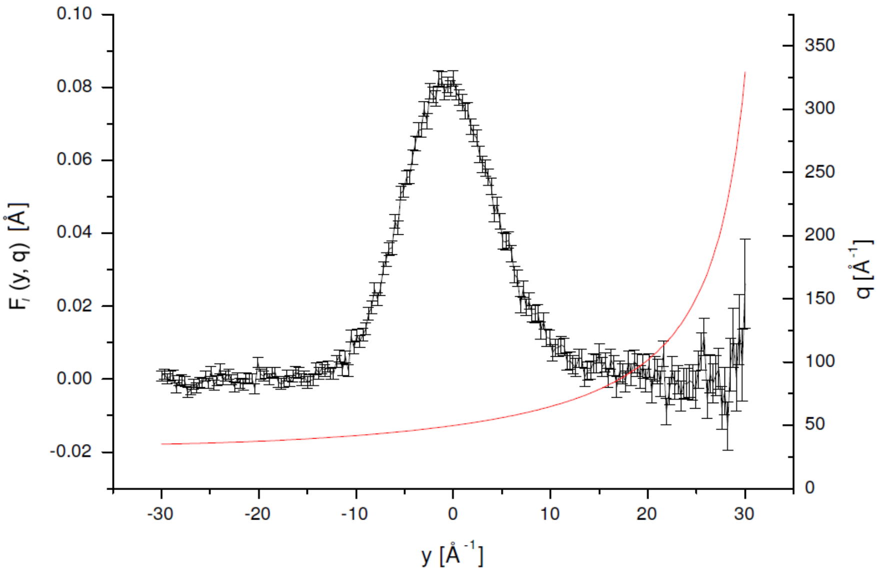

Figure 3.4: *NCP, black line with error bars and wave vector transfer, red line. The scattering angle is 45°.*

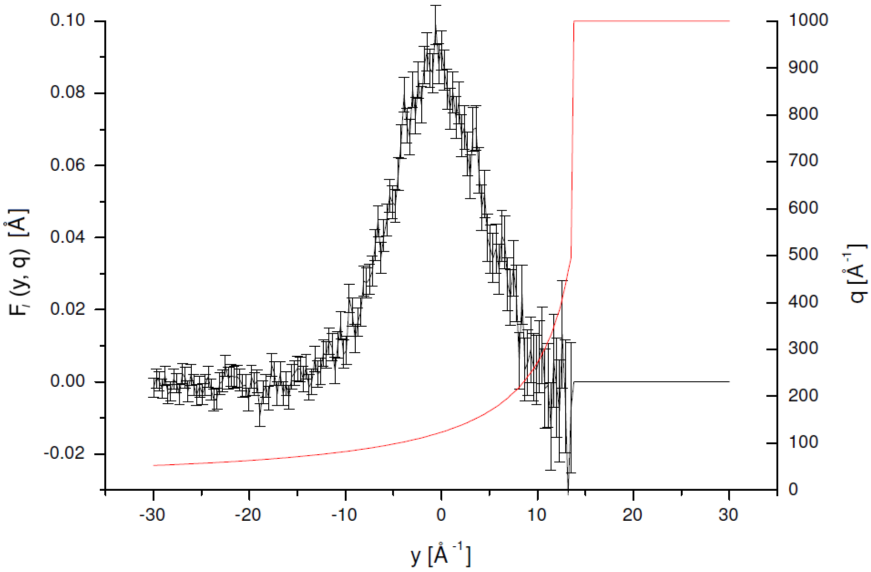

Figure 3.5: *NCP, black line with error bars and wave vector transfer, red line. The scattering angle is 68°. At this scattering angle the y spectrum is cut. Furthermore at large y values the noise is larger, as these values corresponds to very small TOF. For computational purpose, the y values out of the range are put equal to zero, with a huge error bar (not reported in this plot) and the q value equal to 1000* Å^{-1}.

of all the spectra and it is due to the fact that large positive y, correspond to short times of flight, where there are less counts, producing larger noise. Furthermore the 60° angle spectrum is cut, because such value of y corresponds to time of flight values smaller than 100 μs, that is the minimum value of the TOF range. This suggests that is not useful to have spectra at angle higher than 72° (for H recoil), despite the improvement of the impulse approximation as the exchanged wave vector increases.

In the cut spectra, the y values, that were not available, are set to zero with very large error bars and the exchanged wave vector to 1000 $\AA^{-1}$ for computational purpose.

The y transform must also be performed for the instrumental resolution calculated with the MC simulation. By doing so we obtain the instrumental resolution in the y space: $R_l(y, \vec{q})$, for each l^{th} detector.

3.5 Data Analysis

The experimental $F_l(y, \vec{q})$ have been normalized to unit area, following the zero-order sum rule for the dynamical incoherent structure factor [24].

The recoil peak of the H has a width that depends on the scattering angle. Instead, when the TOF data are transformed into the y space the $F_l(y, \vec{q})$ are an evaluation of the same physical quantity, and its q dependence is only related to the FSE and to the instrumental resolution. Figure 3.6 shows how the different $F_l(y, \vec{q})$ functions scale to collapse into a single detector averaged Compton profile.

The NCP $F_l(y, \vec{q})$ are affected by the instrumental resolution and by the FSE. The experimental NCP can then be expressed as:

$$F_l(y, \vec{q}) = [J_{IA}(y) + \Delta J_l(y, \vec{q})] \otimes R_l(y, \vec{q}), \tag{3.6}$$

where $J_{IA}(y)$ is the longitudinal momentum distribution, $\Delta J_l(y, \vec{q})$ are the q-dependent deviations from the IA (final state effects), and $R_l(y, \vec{q})$ is the fixed-angle instrumental resolution function. The angle-averaged $F_l(y, \vec{q})$, named $\overline{F}(y)$, is derived by calculating a simple average over the different detectors. This quantity, shown in figure 3.7, provides a graphical representation of the overall quality of the data.

The $J_{IA}(y)$ line shape as well as $n(p)$ and $\langle E_k \rangle$ have been calculated from the $F_l(y, \vec{q})$ spectra in three different ways:

- M0 model: the $\langle E_k \rangle$ value is obtained by numerical integration of $\overline{F}(y)y^2$;
- M1 model: a full analysis of the DINS line shape via simultaneous fitting of the individual $F_l(y, \vec{q})$ spectra with a model-independent line shape;

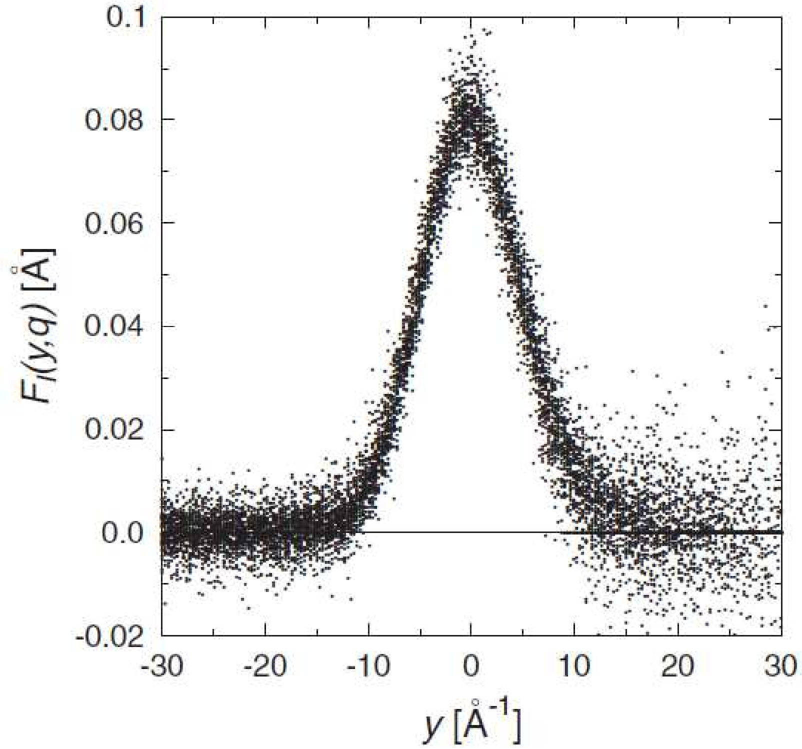

Figure 3.6: *Plot of all the NCP, $F_l(y,\vec{q})$, (markers with omitted error bars) from all detectors. The plot shows the collapse of the profiles at different angles, demonstrating that the scattering regime reached in the present experiment is well described within the IA. For the highest angles, the artificially imposed $F_l(y,\vec{q})$ are omitted for $y > y_{max}$.*

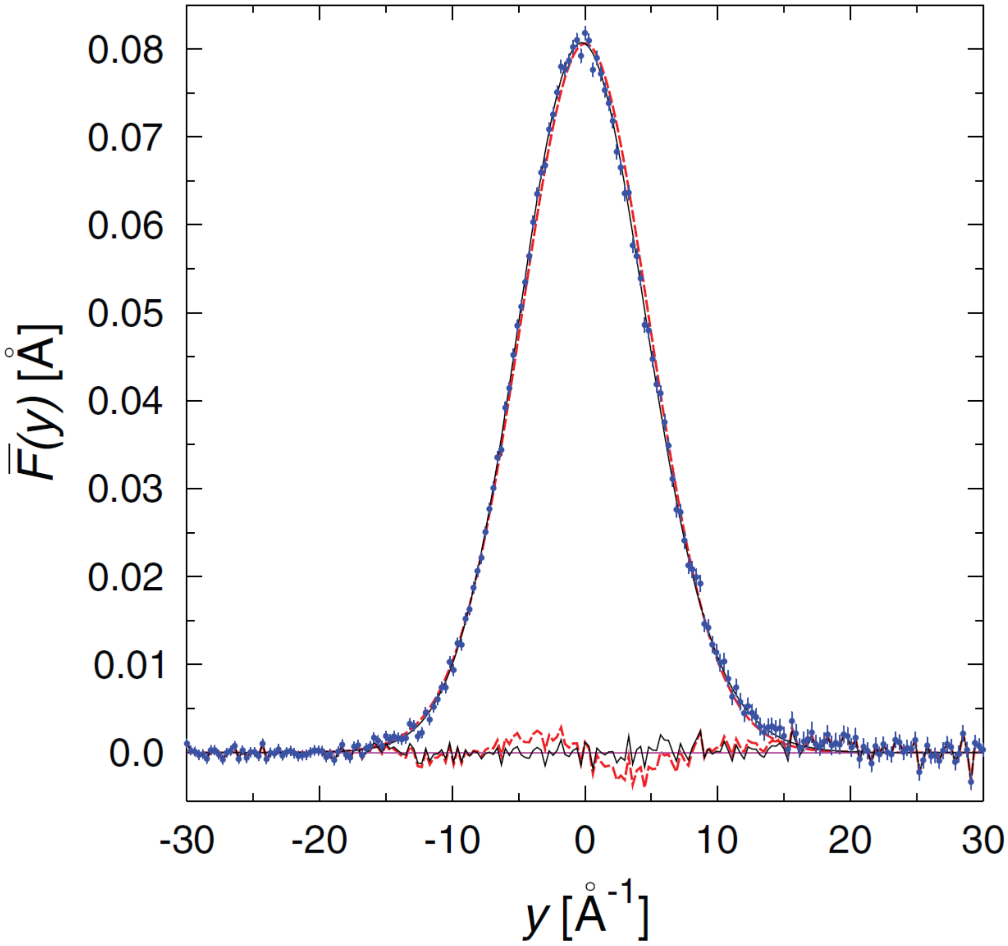

Figure 3.7: *Experimental Neutron Compton Profile for ice at* $T = 271$ *K averaged over the whole set of the scattering angles* ($\overline{F}(y) = \langle F_l(y, \vec{q}) \rangle_l$) *(blue dots with error bars). The angle-averaged best fit is reported as a black continuous line for the M1 model. If final state effects are not accounted for, the corresponding angle averaged best fit is reported as a red dashed line. The fits residuals are also reported.*

- M2 model: full analysis of the DINS line shape via simultaneous fitting of the individual $F_l(y,\vec{q})$ spectra with a three dimensional anisotropic Gaussian line shape derived from a quasi-harmonic model.

The numerical integration of $\overline{F}(y)y^2$ [128] provides a first order estimate of $\langle E_k\rangle$:

$$\int_{-\infty}^{+\infty} \overline{F}(y)y^2 = \sigma_F^{2*}. \tag{3.7}$$

The deconvolution of the instrumental resolution is obtained, in this framework, by calculating the $\overline{R}(y)$, i.e. the angle averaged resolution function, and then its second momentum as in the equation 3.7:

$$\int_{-\infty}^{+\infty} \overline{R}(y)y^2 = \sigma_R^2 \tag{3.8}$$

and subtracting the σ_R^2 value to σ_F^{2*}. σ_R^2 results 0.98 $\AA^{-2}$, yielding $\sigma^{2*} = \sigma_F^{2*}$ - $\sigma_R^2 = 27.0 \pm 2.7$ $\AA^{-2}$. The $\langle E_k\rangle^*$ results 169 ± 19 meV.

Furthermore one can obtain the momentum distribution $n^*(p)$ by a direct numerical derivation of $\overline{F}(y)$ (see the equation 1.72). In this case a direct deconvolution of the resolution is not possible. The derivation of a noisy experimental data is also a difficult task, because the main effect of the derivation is to increase the noise. We than perform a smoothing of the $\overline{F}(y)$ just to have a first raw estimate of the momentum distribution too.

In figure 3.8 $n^*(p)$ is reported as a function of $|p|$. The noise dominates for small p, but for larger values the agreement between the $n^*(p)$ and the best fit of $n(p)$ obtained with the M1 model is appreciable. It has to be pointed out that the continuous line in figure 3.8 does not contain the instrumental resolution and the final state effects contribution, while $n^*(p)$ does. The agreement among the two function shows the validity of the impulse approximation and the very high resolution of the VESUVIO spectrometer.

The two parametric methods of analysis involve the fitting of the $F_l(y,\vec{q})$ spectra with either model-independent or multivariate Gaussian functions, the latter corresponding to a harmonic picture of the effective proton potential. We will call this two methods M1 and M2, respectively. Only the M1 model is available on the instrument program suite. For M1, the model-independent form for $J_{IA}(y)$ is:

$$J_{IA}(y) = \frac{e^{-\frac{y^2}{2\sigma^2}}}{\sqrt{2\pi}\sigma}\left[1+\sum_{n=2}^{+\infty}\frac{c_n}{2^{2n}n!}H_{2n}\left(\frac{y}{\sqrt{2}\sigma}\right)\right], \tag{3.9}$$

a Gaussian function times a sum of Hermite polynomials. The momentum distribution can then be written as [129, 130]:

$$n(p) = \frac{e^{-\frac{p^2}{2\sigma^2}}}{(\sqrt{2\pi}\sigma)^3}\left[1+\sum_n c_n(-1)^n L_n^{\frac{1}{2}}\left(\frac{p^2}{2\sigma^2}\right)\right], \tag{3.10}$$

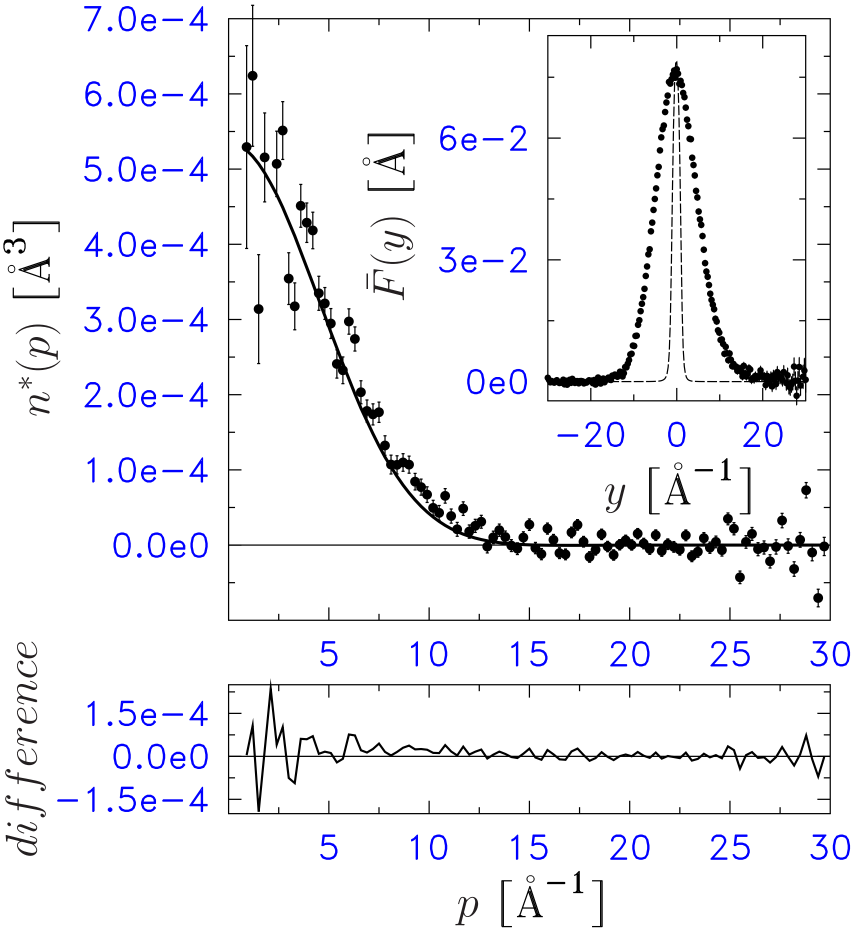

Figure 3.8: *Direct numerical determination of the proton momentum distribution $n^*(p)$ (points with error bars) and momentum distribution $n(p)$ derived by the M1 model (continuous line). The lower panel reports the difference between $n^*(p)$ and $n(p)$. The inset reports $\overline{F}(y)$ (points with error bars) and $\overline{R}(y)$ (dashed line). Except for very low p values, for which the factor $\frac{1}{y}$ of the equation 1.72 produces large noise, the agreement between $n^*(p)$ and $n(p)$ is very good. It is worth to note that the $n^*(p)$ has not been corrected for the instrumental resolution nor for the FSE. This is another evidence of the high performance of the VESUVIO spectrometer in DINS measurements.*

where $L_n^{\frac{1}{2}}$ are the generalized Laguerre polynomials.

The fitting parameters of the M1 model are the standard deviation σ and the coefficients of the Hermite polynomial. This form is very general (it is a complete basis of the 1-variable function space) and very convenient for the system we are analyzing, from a computational point of view: only the first term of the sum in the equation 3.9 is taken into account (the summation converges very quickly) and the $\langle E_k \rangle$ is directly related to σ and independent from the other fitting parameters. This model however may not facilitate the interpretation of the data as it does not allow us to separate the effects of the anharmonicity from those of the anisotropy.

In particular, in the case of ice, a recent PICPMD (Path Integral Car-Parrinello Molecular Dynamics) calculation [131, 126] shows that, within statistical errors, the momentum distribution of each individual proton is well approximated by a multivariate Gaussian distribution with three distinct frequencies ω_x, ω_y and ω_z.

These are associated to local principal axes that depend on the crystalline orientation of the molecule to which the proton belongs [101]. This constitutes an anisotropic quasi-harmonic model in which the effective frequencies ω_i account for the main effects of anharmonicity. Experiments access the total momentum distribution, i.e., the superposition of the distributions of all the protons in the sample. In polycrystalline samples a spherically averaged distribution originates in this way:

$$n(p) = \left\langle \frac{1}{\sqrt{8\pi^3}\sigma_z\sigma_y\sigma_x} \exp\left(-\frac{p_z^2}{2\sigma_z^2} - \frac{p_y^2}{2\sigma_y^2} - \frac{p_x^2}{2\sigma_x^2} \right) \right\rangle_\Omega . \tag{3.11}$$

Here $\langle ... \rangle \, \Omega$ denotes spherical average and the variances $\sigma^2_{i=x,y,z}$ are related to the principal frequencies by:

$$\hbar^2\sigma^2 = \frac{M\hbar\omega_i}{2}\left(\coth\frac{\beta\hbar\omega_i}{2}\right). \tag{3.12}$$

In the M2 model we are thus imposing a physical model to the momentum distribution following information deriving from PICPMD. In this model we have three fitting parameters: σ_x, σ_y and σ_z.

For finite q, the deviation from the IA can be accounted for by adding corrections, to first order in $1/q$. In both M1 and M2 the underlying model for $\Delta J_l(y, \vec{q})$ is based on the original framework proposed by Sears [24]. The experimental Compton profile is q-dependent and the following approximation is used:

$$J(y,q) = \left(1 - A_3(q)\frac{\partial^3}{\partial y^3}\right) J_{IA} = J(y) + \Delta J(y,q). \tag{3.13}$$

Here the leading form of $J_{IA}(y)$ is assumed to have a simple Gaussian shape, and introducing

$x = \frac{y}{\sqrt{2}\sigma}$, we have:

$$-\frac{\partial^3}{\partial y^3} J_{IA} = J_{IA} \frac{1}{\sigma^3 2^{3/2}} H_3 \left(\frac{y}{\sqrt{2}\omega} \right), \tag{3.14}$$

where $H_3(x) = 8x^3 - 12x$. Since $A_3(y)= \frac{m\nabla^2 V}{36\hbar^2 q}$ we obtain, for an isotropic harmonic potential

$$\Delta J(y,q) = \frac{e^{\frac{-y^2}{2\sigma^2}}}{\sqrt{2\pi}\sigma} \frac{M^2\omega^2}{12\hbar^2 q} \frac{1}{\sigma^3 2^{3/2}} H_3 \left(\frac{y}{\sqrt{2}\sigma} \right). \tag{3.15}$$

The q-independent factor $\frac{M^2\omega^2}{12\hbar^2} \frac{1}{\sigma^3 2^{3/2}}$, in $\Delta J(y,q)$ defines a positive parameter, c1:

$$\Delta J(y,q) = \frac{e^{\frac{-y^2}{2\sigma^2}}}{\sqrt{2\pi}\sigma} \frac{c1}{q} H_3 \left(\frac{y}{\sqrt{2}\sigma} \right). \tag{3.16}$$

This term is asymmetric and induces a modulation in $J_{IA}(y)$. The dependence on q and on the scattering angle can be appreciated in figure 3.10, where the apparent centroid of $F_l(y,\vec{q})$ at the lowest scattering angle is shifted to slightly negative y values, as well as in figure 3.7 , where the average over all detectors shows the *average* shift of the centroids due to the FSE [24]. Neglecting of final state effects results in poorer fits with larger residuals, with typical asymmetric shape. In addition, if the final state effects are not accounted for in the fitting, the kinetic energy derived, for example from M1, is reduced by approximately 5 meV. Figure 3.9 shows the modulation induced by FSE on a low angle detector spectrum.

Both M1 and M2 procedures rely on the minimization of:

$$\chi^2 = \sum_l \sum_i \frac{\left(F_l^{th}(y_i,q_i) - F_l(y_i,q_i)\right)^2}{\epsilon_{l,i}^e}, \tag{3.17}$$

where $F_l^{th}(y_i,q_i) = [J_{IA}(y) + \Delta J_l(y,\vec{q})] \otimes R_l(y,\vec{q})$. Here $J_{IA}(y) + \Delta J_l(y,\vec{q})$ is described by either M1 or M2 line shapes, the index l represents the detector index, the index i represents the y value at the i^{th} bin and $\epsilon_{l,i}$ is the uncertainty for each data point. The double sum over i and l reflects the relevant properties:

- $J(y)_{IA}$ is unique for all detectors;
- $\Delta J_l(y,\vec{q})$ varies across detectors due to the different q values accessed, but $c1$ is independent on q and is unique for all detectors;
- $R_l(y,\vec{q})$ varies across detectors, but can be extracted by calibration procedures.

Based on the above physical assumptions, we have carried out the fitting, using M1 and M2, minimizing the above global χ^2, as defined in 3.17 for all detectors simultaneously, to provide unique values (detector-independent) of σ, a_2, $c1$, σ_x, σ_y, σ_z. We have considered the global fitting as the preferred choice with respect to the fitting of individual detectors.

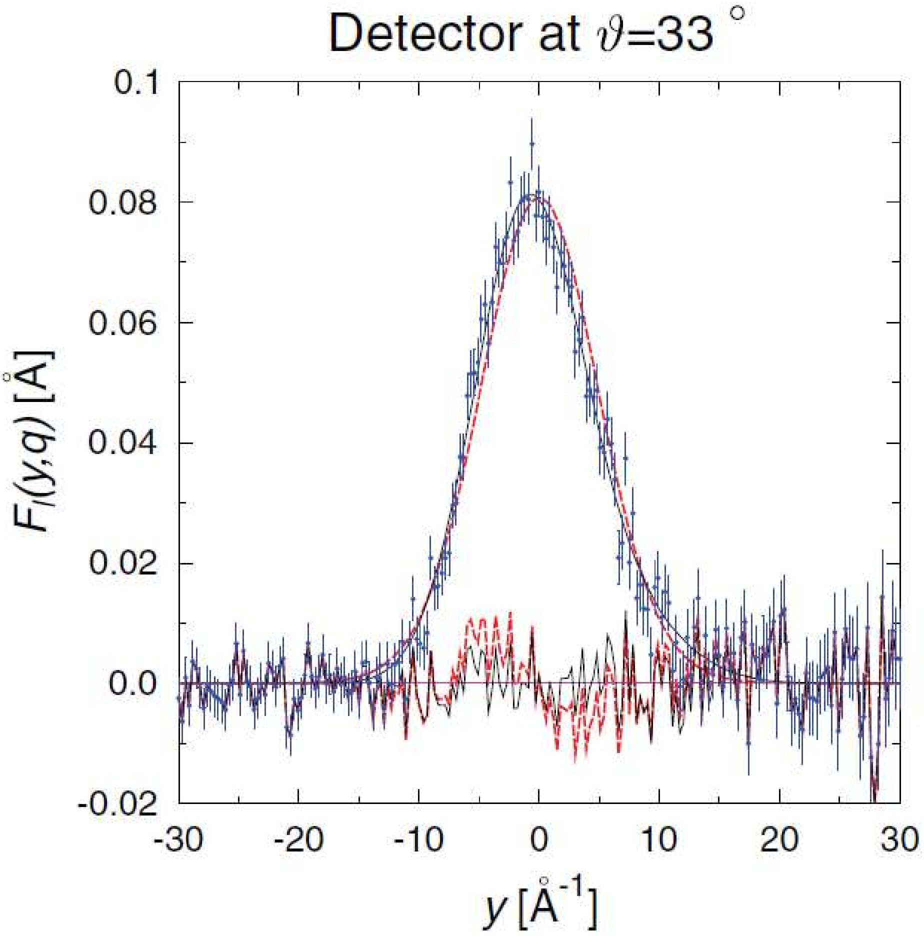

Figure 3.9: *Experimental Neutron Compton Profile,* $F_l(y,\vec{q})$*, at a scattering angle* $\theta = 33°$ *for ice at* T = *271 K (blue dots with error bars). The best fit using M1 with the inclusion of FSE is reported as a black continuous line, while if FSE are not included in M1 the best fit is shown as a red dashed line. The fits' residuals are also reported.*

The latter is generally used on VESUVIO to extract σ_l, a_{2l}, $c1_l$, etc., whose averages give the parameters σ, a_2, $c1$. However, the global fit has its basis on the invariance of $J(y)_{IA}$ and $c1$ across different detectors, while the individual fitting follows the approach of finding *l statistically independent* momentum distributions to be subsequently averaged. It is worth to be stressed that, since the χ^2 for individual detectors is weighted by the error bar, and the latter is poorly correlated with the noise present at high positive y, the results from individual detectors may be affected by the noise, since the latter is not accounted for by the χ^2. On the other hand the global fitting provides a more efficient way for noise cancellation. The fit with the M1 model has been carried out using a FORTRAN code which makes use of the MINUIT minimization routine, [132] while the fit with the M2 model has been carried out using a MATLAB code. Examples of the quality of fits for the M1 model are reported in figure 3.10.

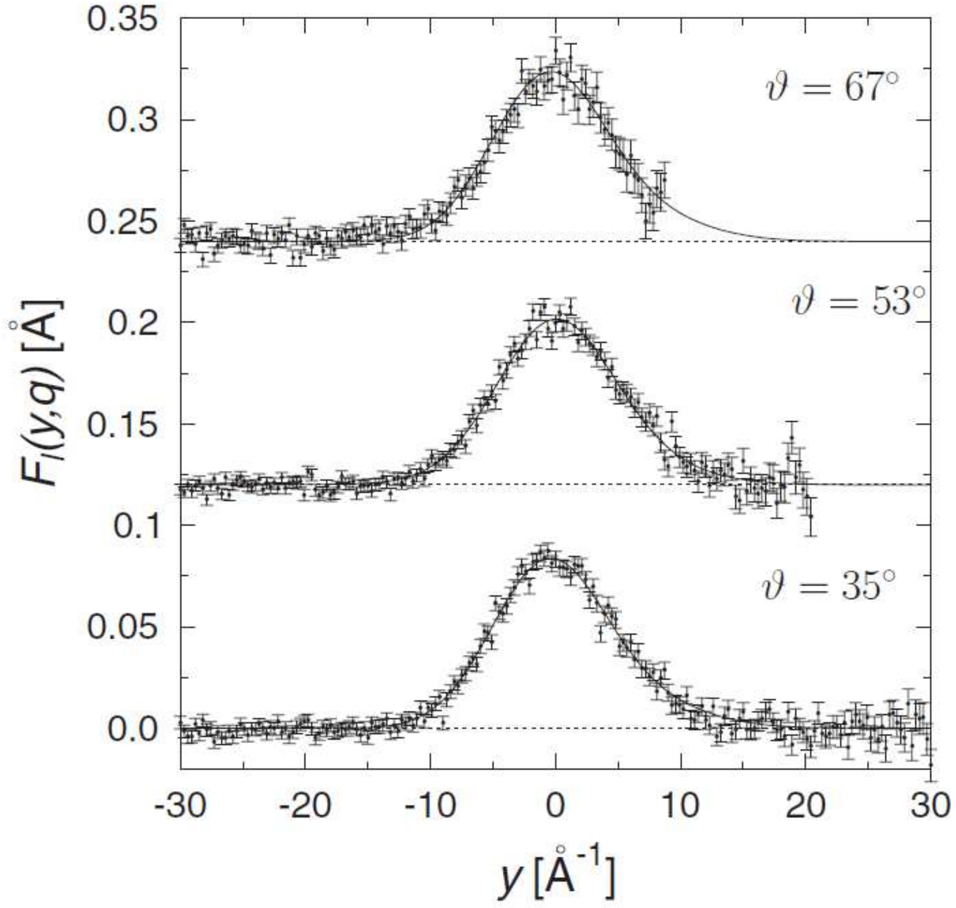

Figure 3.10: *Example of normalized NCP, $F_l(y,\vec{q})$, (markers with error bars), for three scattering angles, together with their best fits using the M1 model. Two of the spectra are shifted upwards for clarity. For the two highest angles, the artificially imposed $F_l(y,\vec{q}) = 0$ are omitted for $y > y_{max}$. The the apparent centroid of $F_l(y,\vec{q})$ at the lowest scattering angle is shifted to slightly negative y values, due to the FSE.*

Chapter 4

Data analysis: DINS on oriented single crystal ice

In this chapter we will describe the data analysis of the DINS experiment carried on an oriented ice sample. The sample is an ice film of 5 *mm* thickness onto a 0.5 *mm* thick-15 *mm* diameter platinum single crystal substrate.

The sample has been prepared by evaporating H_2O in a vacuum chamber. The initial base pressure of chamber was $\approx 6.5\times10^{-11}$ *mBar*. The *Pt* (111) crystal was cleaned via repeated Ar^+ sputter-anneal cycles, ($\approx$ 500 *eV* energy of the *Ar* ions with a drain current between 5 and 7 *A*) using anneal temperatures of 903 K to 923 K. The *Pt* crystal was also given repeated oxygen treatments to remove any carbon contamination. and cleanliness was verified by LEED.

Initially the ice layer was prepared by dosing approximately the first 100 layers of water via a molecular beam. The dose temperature used was 145 K with a dose time of 5 hours and the approximate dose rate was 0.33 layers min^{-1}. The crystal was then moved to the effusive dose position in order to increase the growth rate. The pressure of water in the chamber was steadily increased coupled with the dose temperature (up to 2×10^{-5} *mBar* and 167 K, respectively), to promote single ice crystal growth over nucleation.

From previous calibrations, the dose rate in these conditions was $\approx$ 90 layers s^{-1}. For a total deposition time of $\approx$ 36 hours ($\approx$ 129600 s) thus yield to $\approx 11.6\times10^6$ layers of water, corresponding to an ice film of $\approx$ 4.65 *mm* thick [133].

The data reduction of this experiment follows the same step described in the previous chapter, i.e. multiple scattering subtraction, heavy masses recoil peaks subtraction and y variable transformation of the TOF spectra. In this chapter we will then describe only the part that differs from the polycristalline ice experiment.

The *Pt* substrate has in fact many neutron resonances that appear in the time of flight spectra and are superimposed to the hydrogen recoil peak, so a careful subtraction of these peaks is needed.

Furthermore the geometry of the experiment and the features of the sample could allow us to extract directional informations with a constant q analysis of the Neutron Compton Profile.

In the present experiment as in the experiment described in the previous chapter, the data reduction procedure include only 48 detectors.

4.1 Subtraction of Pt capture resonances

On VESUVIO the neutron data recording is performed using the foil cycling acquisition procedure. This technique is mostly optimized for recording neutron scattering signals. In the presence of significant signal due to radiative resonance capture in the sample, Pt in this case, a residual contribution from the resonance capture is still present in the neutron TOF spectra and must be then accounted for. The neutron radiative capture cross section of Pt shows several resonances which can be seen as fingerprints in the time of flight spectra registered by the YAP detectors of VESUVIO. As for the gold analyzer foil (the primary foil) when a neutron has been captured by a Pt nucleus, it excites, and quickly decays emitting γ rays that are revealed by the YAP scintillators.

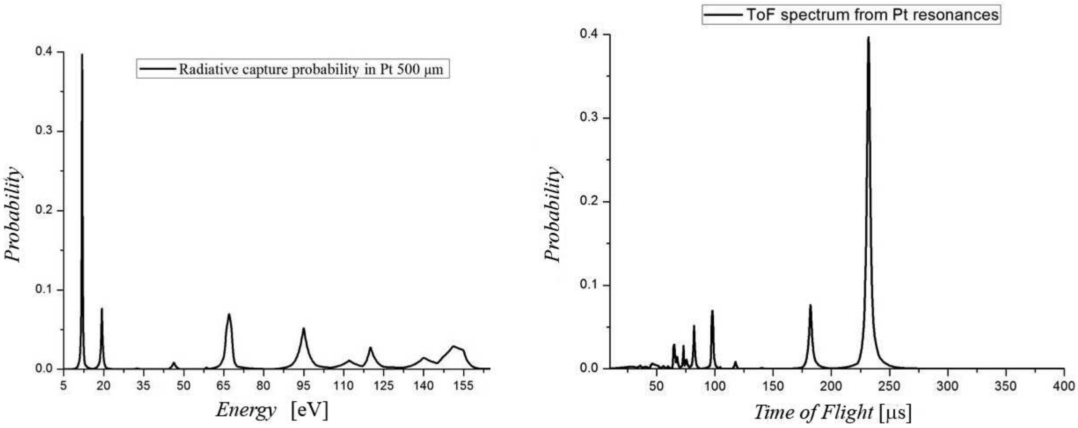

Figure 4.1: *Calculated and measured TOF Neutron Radiative capture interaction probability in 0.5 mm Pt as a function of energy, left panel and right panel, respectively.*

The interaction probability can be calculated from the radiative capture cross section of Pt (available on public databases, see for example Ref. [134]). Figure 4.1 shows the result of the analytical calculation of the interaction probability in the Pt thickness (500 μm) as a function of neutron energy (left panel) and neutron time of flight (right panel) over the primary flight path $L_0 = 11.055\ m$.

The Pt resonances are found at the same TOF positions for all the different detectors. The position in TOF of a photon produced at the sample position and revealed by the scintillators only depends on the energy value of the capture resonance. For a given resonance, a neutron is captured at a certain energy at the sample position, then a photon travels from the sample to the detectors covering a distance that depends on the detector position. The time that a photon takes to travel from the sample to the detectors is however negligible with respect to our time resolution, so the photons TOF are shrinked to the same TOF value.

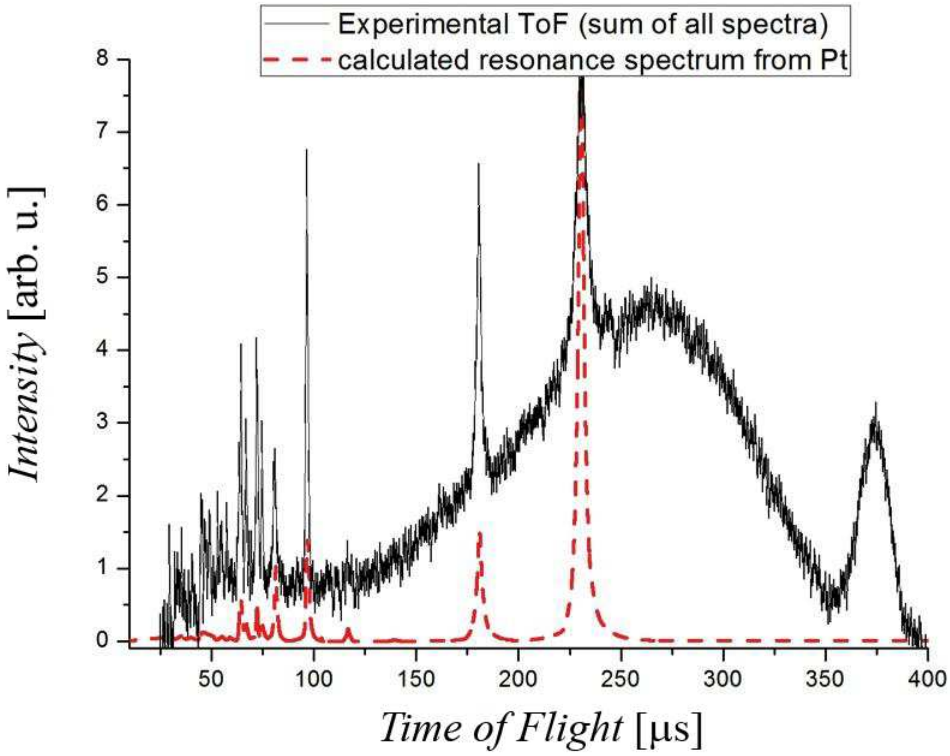

Figure 4.2: *Sum of all TOF DINS spectra of ice at T=130 K and $\alpha = 0°$ (black line). The red lines are the Pt resonances positions calculated using the radiative capture cross sections database.*

This simplifies the subtraction of the resonances and allows us to sum up all TOF data to better visualize the Pt resonances. The sum of all TOF spectra from the oriented ice film at T=130 K and $\alpha = 0°$ are shown in figure 4.2, where one can observe a very good agreement between the calculated and experimental Pt resonances, right panel of figure 4.1 and dotted red line of figure 4.2, respectively.

The lower intensity of the Pt resonances for the $\alpha = 30°$ orientation observed in figure 4.3

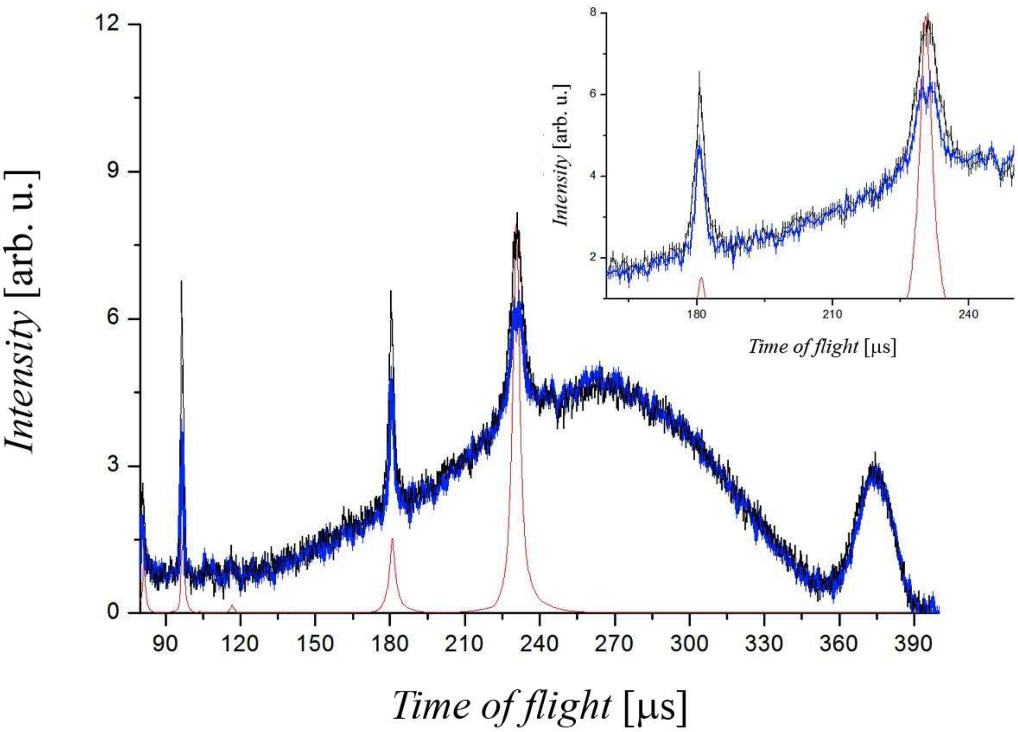

Figure 4.3: *Comparison between the sum of all TOF spectra of the oriented ice at* $\alpha = 0°$ *(black line) and* $\alpha = 30°$ *(blue line) orientations. The calculated Pt resonances positions in TOF are also shown as a red line. The inset shows the region from 160 to 250* μs *to better visualize the intensity of the Pt resonance peaks at the two orientations.*

and insert can be explained as follow. The statistical uncertainties of the neutrons counts is, for each value of TOF, the square root of the counts, as they follows the Poisson distribution [135]. This holds for counts in the foil in and out positions separately, so when the subtraction is performed the counts and the uncertainty become:

$$N_{out} - N_{in} \pm \sqrt{N_{out} + N_{in}}. \tag{4.1}$$

When a background source gives rise to a very large counts value, as the case of the *Pt* resonances, the subtraction of the spectra yields to a large relative error. As a consequence the removal of the background in the FCT is far from complete. Analyzing the singles TOF spectra it arises that the residual contributions from the resonance capture in the sample result as positive and negative dips in the TOF spectra. In figure 4.4 some dips are clearly observed as a fingerprint of the radiative resonance capture in the sample. This feature accounts for the lack of intensity observed in figure 4.3 and insert.

The residual contribution from radiative resonance capture has been subtracted in the TOF spectra for each detector by fitting Voigt functions to each resonance peak, as the subtraction of peaks from the heavy mass atoms recoil discussed in the previous chapter. Figure 4.5 shows two examples of TOF data before and after the resonances subtraction.

The remaining part of the data reduction follows exactly the same steps described in chapter 3 for DINS on polycrystalline ice. In figure 4.6 the $\bar{F}(y) =< F_l(y, \vec{q}) >_l$ are reported for $\alpha = 0°$ and $\alpha = 30°$.

After the measurements for the two values of α, the ice film has been removed from the *Pt* substrate and the same measurement, for $\alpha = 0°$ were repeated with only the ice in the beam. This measurement will be used to check for the reliability of the resonance subtraction procedure.

4.2 Constant $\hat{q}$ analysis

As discussed in chapter 1, DINS allow us to measure the momentum distribution along a direction identified by the wave vector transfer. For isotropic samples as liquids, or polycrystalline solids, the momentum distribution is averaged over the whole solid angle. If the sample has a defined geometry however directional information could be extracted.

All the kinematics of the scattering is known, so for each TOF value or equivalently for each y value of each $F_l(y, \vec{q})$ the modulus and the direction of $\vec{q}$ is known.

Let us call c the axis of growth of the ice crystal and α the angle between c and the incident beam direction. As described before, a measurement has been done for $\alpha = 0°$ and $30°$. Let us define β as the angle formed by c and $\vec{q}$. We can scan the whole set of $F_l(y, \vec{q})$

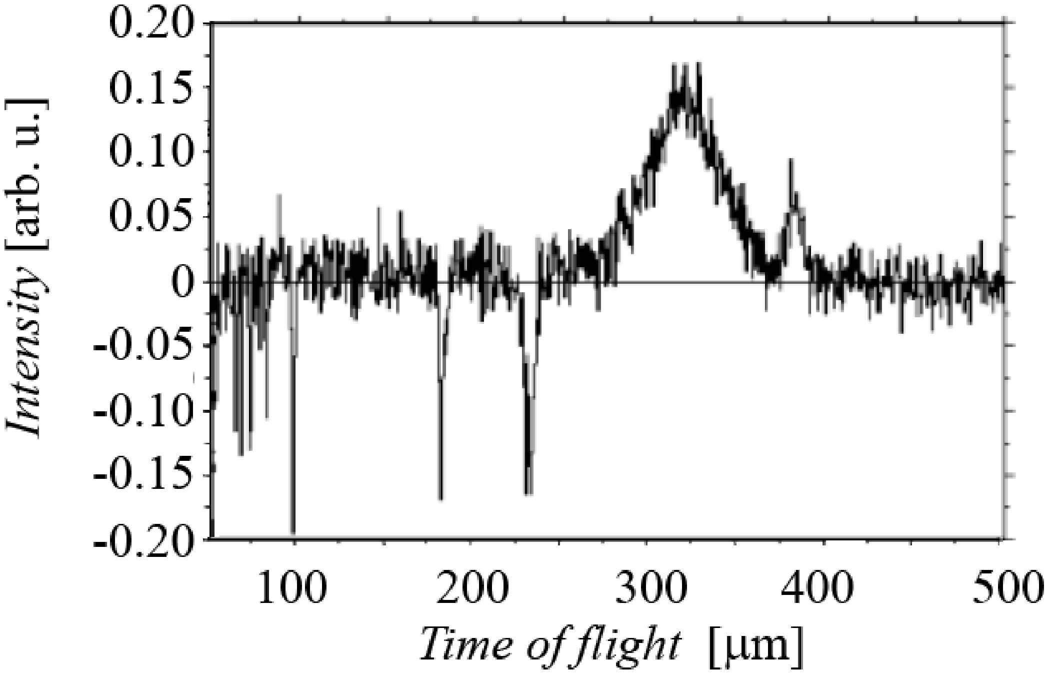

Figure 4.4: *A TOF spectrum from Pt+Ice. In principle the Pt resonances, and all resonances in general, should be eliminated upon the subtraction of the foil in and foil out spectra. However, the statistical uncertainties of the difference of two large counts, has a large relative error. As a result the intensities of the resonances in the TOF spectra are spread over a wide range of values. In particular a resonance can appears as a sharp peak (as in the sum of all detectors) or as a dip, as in this spectrum.*

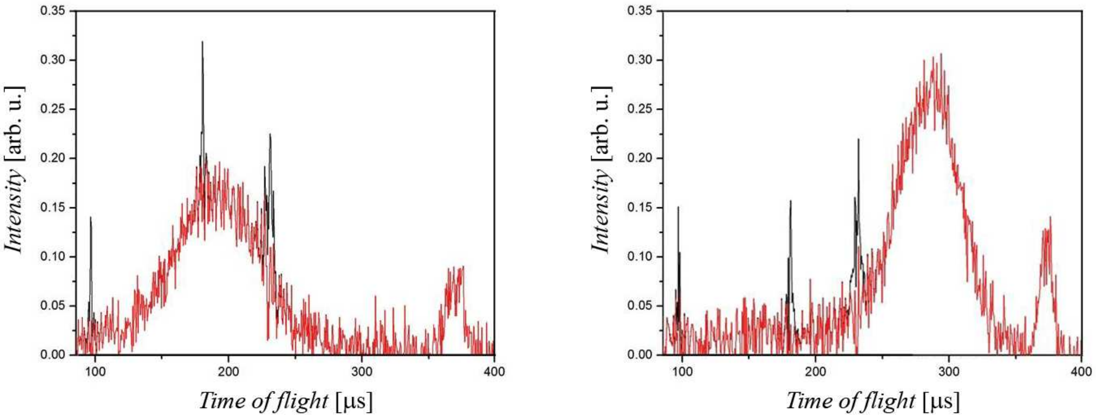

Figure 4.5: *Examples of TOF DINS data at low (θ = 34°) and high (θ = 65°) scattering angle before (black line) and after subtraction of the main Pt resonances.*

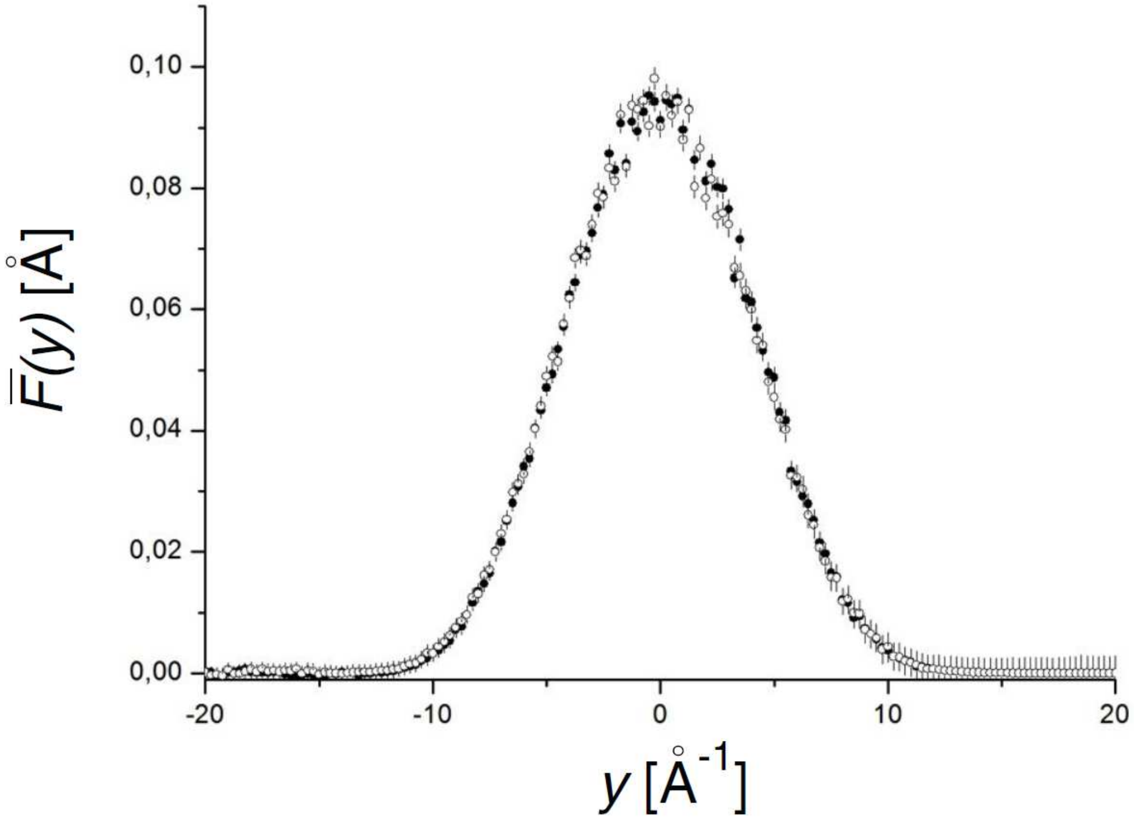

Figure 4.6: *Experimental angle averaged NCP, $\bar{F}(y)$, for the T= 130 K ice film sample at α = 0°(open dots) and α = 30° (full dots).*

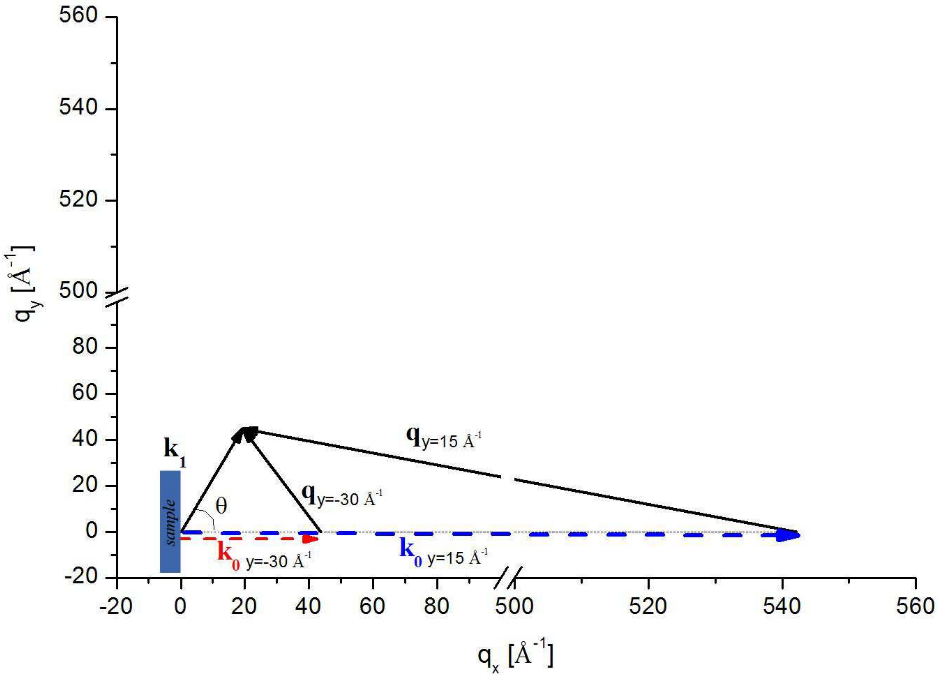

Figure 4.7: *Kinematics of DINS scattering for* $\theta = 65°$ *in the longitudinal* y *range* -30 Å^{-1} $<$ $y <$ 15 Å^{-1} *corresponding to initial neutron wave vectors range* 44 Å^{-1} $< k_0 <$ 543 Å^{-1} *and a fixed value of* $k_1 =$ 48.6 Å^{-1} . *In the figure the scattering wave vector* $\vec{q}$ *is plotted for the extreme values of* y= -30 Å^{-1} *and* y = 15 Å^{-1}.

looking for the y and l values that correspond at a certain value of the angle β (i.e. the $\vec{q}$ direction with respect to the c axis).

It is important to emphasize that in picking up data points at constant $\hat{q}$, the whole set of data at $\alpha = 0°$ and 30° is used, because for a fixed l and y we have different values of β.

In figures 4.7, 4.8 and 4.9 the kinematic of the scattering events is shown. The values of the β angles chosen are: 130°, 150° and 180°. For these tree angles we have enough data points to reconstruct the $F(y, q, \hat{q} = constant)$. The range of the selected angles are 10° around each β value.

In figures 4.10, 4.11 and 4.12 the Neutron Compton Profiles are shown for $\beta = 130°$, 150° and 180 °. It appears clear from these plots, that values of β larger than 180° and smaller than 130° would not have an NCP in a reasonable range of y. The fits are done with the Gauss-Hermite fitting function [136].

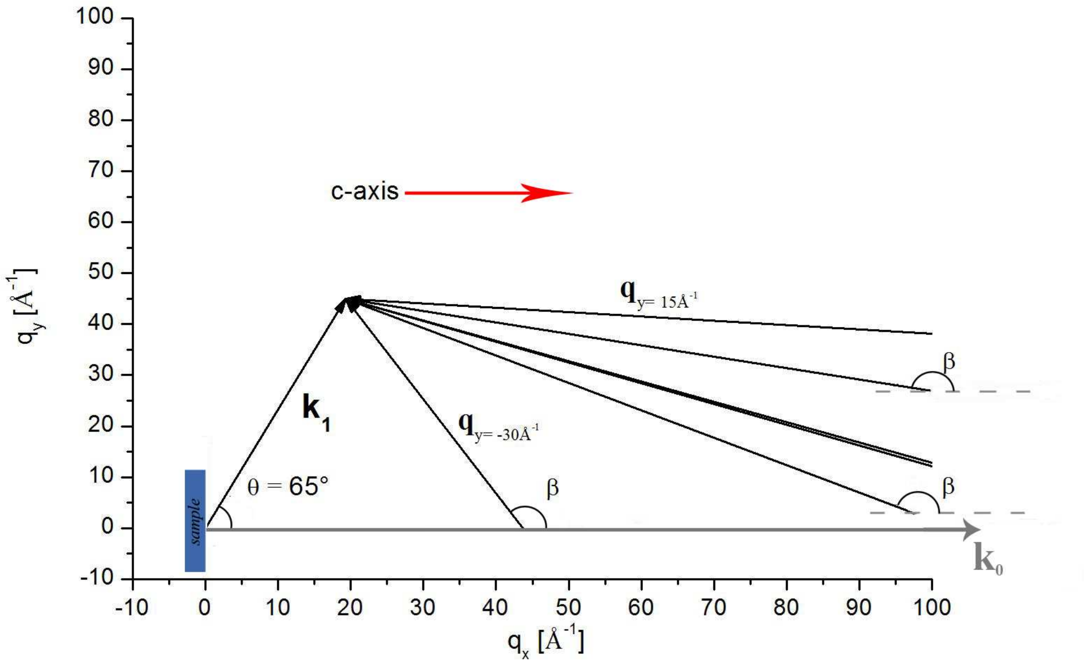

Figure 4.8: *Kinematics of DINS scattering and* $\vec{q}$ *orientations with respect to the sample c-axis (red arrow) or* $\alpha = 0°$ *at* $\theta = 65°$ *scattering angle. In the figure the scattering wave vector transfer* $\vec{q}$ *is plotted for the extreme values* y = -30 Å^{-1} *and* y = 15 Å^{-1} *and for few intermediate values. The direction of* $\vec{q}$ *with respect to the c direction is indicated by the angle* β*. For larger q values* β *approach 180°. Values of* $\beta < 120°$ *are unaccessible. This sample orientation allow us to sample the NCP for* $120° < \beta < 180°$*.*

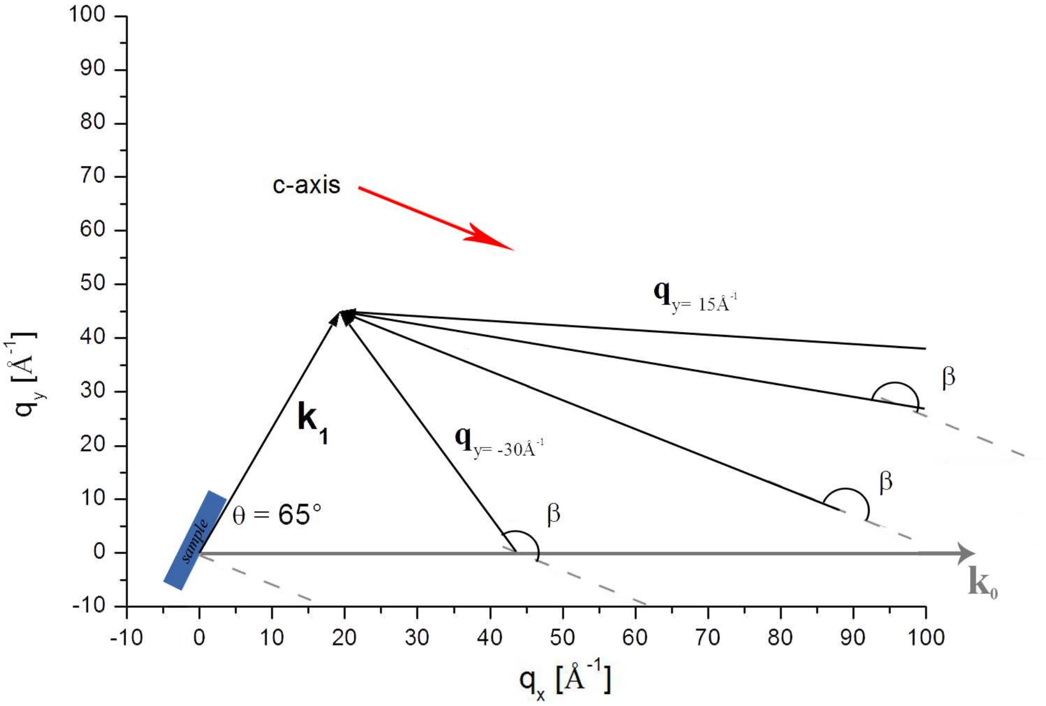

Figure 4.9: *Kinematics of DINS scattering and $\vec{q}$ orientations with respect to the sample c-axis (purple arrow) or $\alpha = 30°$ at $\theta = 65°$ scattering angle. In the figure the scattering wave vector trnsfer $\vec{q}$ is plotted for the extreme values y = -30 Å^{-1} and y = 15 Å^{-1} and for few intermediate values. The direction of $\vec{q}$ with respect to the c direction is indicated by the angle β. The sample orientation at $\alpha = 30°$ allow us to reach larger value of β. This sample orientation allow us to sample the NCP for $150° < \beta < 210°$.*

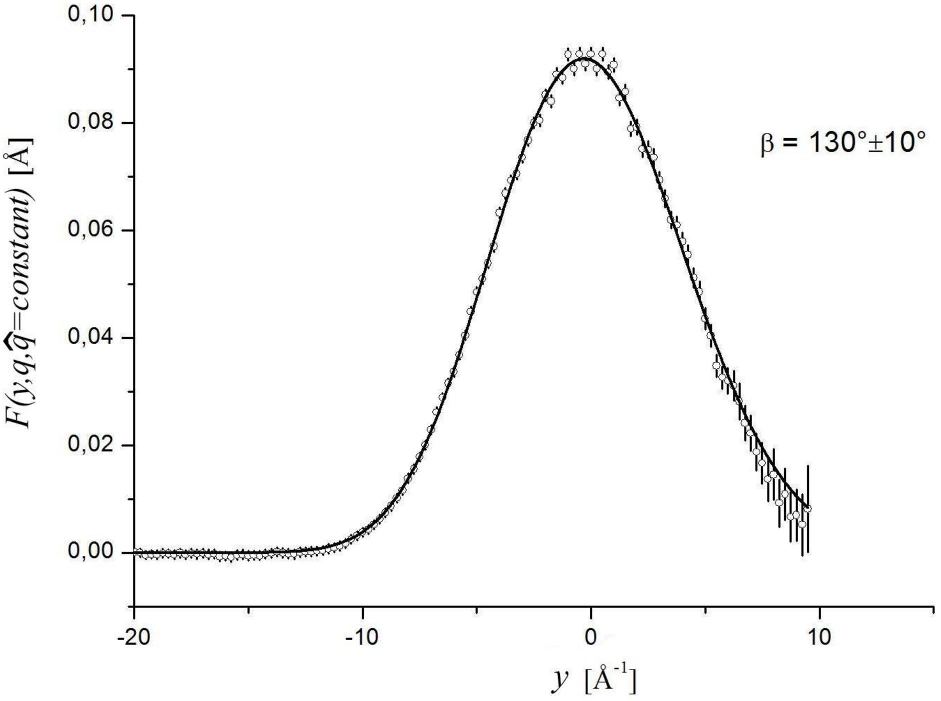

Figure 4.10: *Experimental Neutron Compton Profile for* β = *130 °± 10° and its corresponding best fit.*

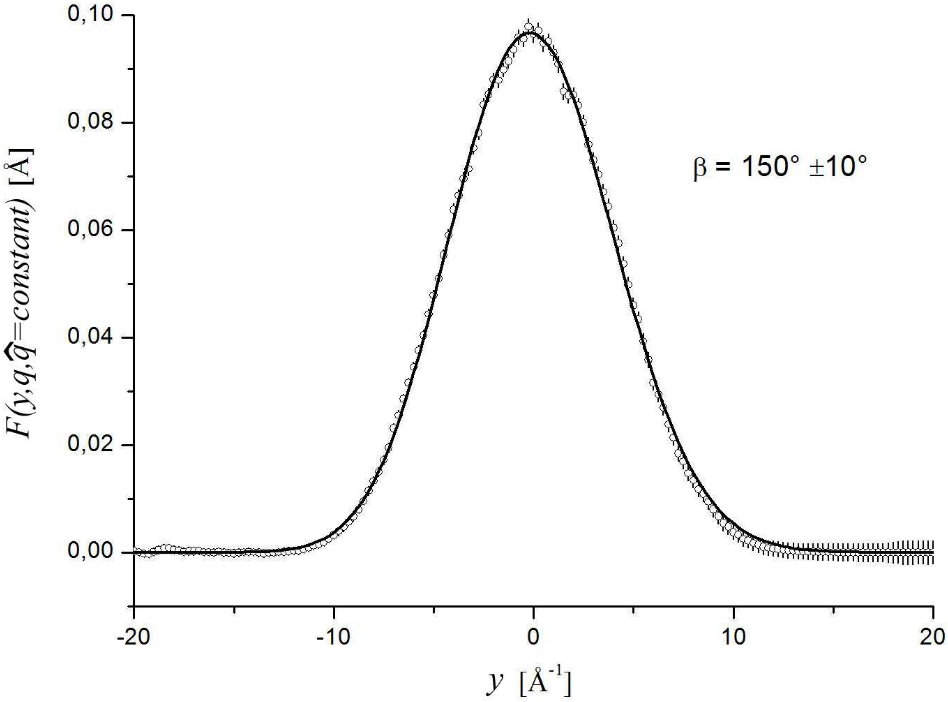

Figure 4.11: *Experimental Neutron Compton Profile for* β = *150* °± *10*° *and its corresponding best fit.*

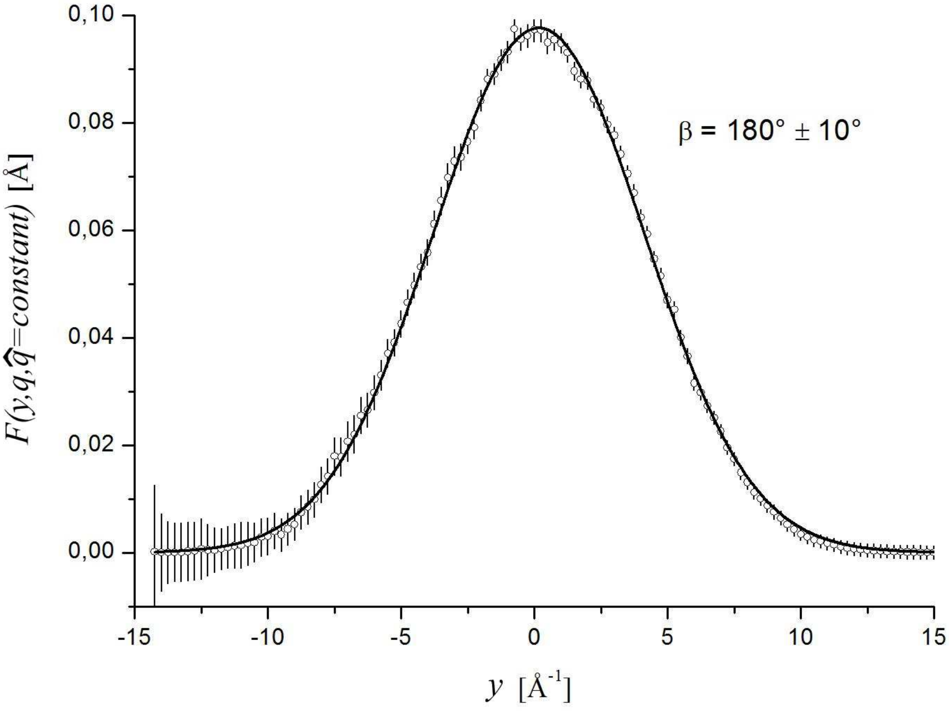

Figure 4.12: *Experimental Neutron Compton Profile for* β *= 180 °± 10° and its corresponding best fit.*

Chapter 5

Data analysis: INS on water and ice

The INS measurements have been carried out at the SNS of Oak Ridge National Laboratories by using the SEQUOIA spectrometer. In particular we measured polycristalline ice Ih at T=271 K, to have a direct comparison with previous experiments and simulations [96, 99], and water at several temperatures from super-cooled water at T= 269 K to room temperature (T= 296 K). The incident energy was fixed to $E_i = 600\ meV$, being the best compromise to access to the whole excitation spectrum and to have the best energy resolution.

We used an Al can for all the measurements. The internal cavity of the can is a disc (5 cm diameter and 0.1 cm wide, see figure 5.1) with a Teflon coating to prevent the nucleation of water below for temperatures slightly below the freezing temperature (T= 273.15 K).

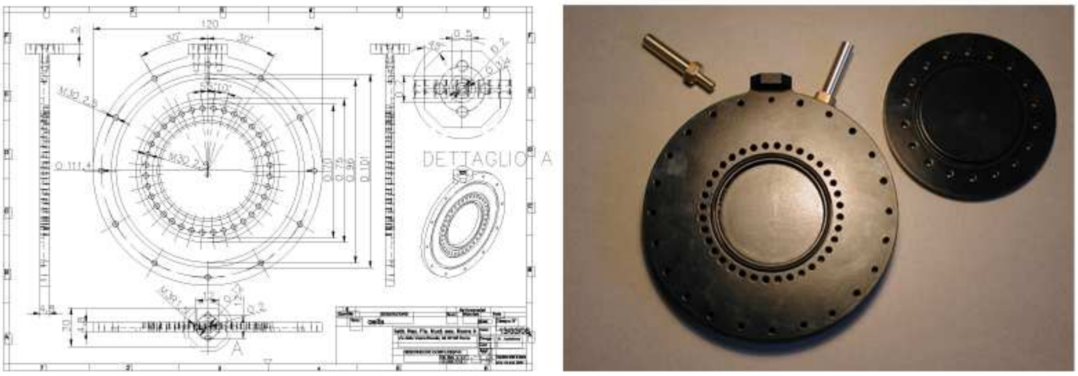

Figure 5.1: *Schematic and picture of the cell.*

The standard software routines available on SEQUOIA allowed us to extract the single $S_\theta(q, E)$ spectra as a function of the energy loss E (q is a function of E and θ) at fixed θ from a data matrix in the (q,E) plane, as reported in figure 5.2. We obtain absolute scattering functions by means of a standard background subtraction and normalization from the scattered intensities of the sample, empty container and vanadium [98] to correct the intensity for the different efficiency of ^3He detectors at different energies and for the factor $\frac{k_f}{k_i}$.

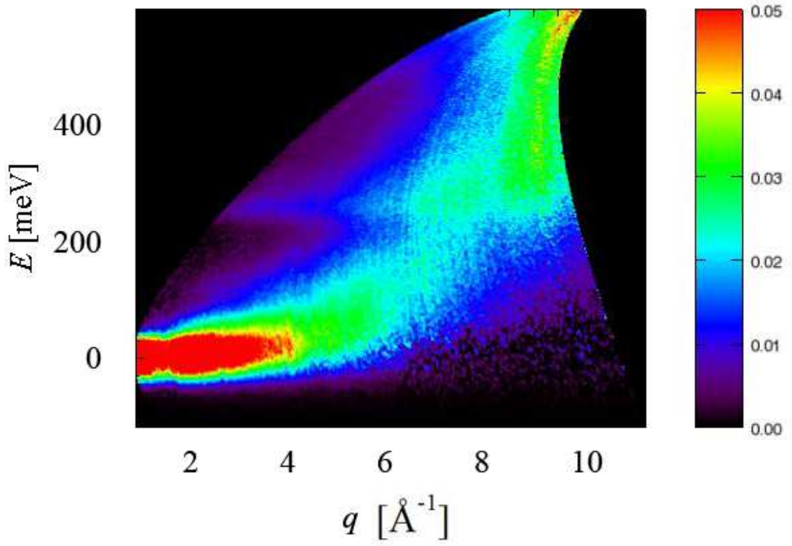

Figure 5.2: *Contour plot in the (q,E) plane, showing the kinematic range explored by the SEQUOIA spectrometer with an incident neutron energy of 600 meV. The bar on the right indicates the intensity values.*

Our data sets are composed of spectra at different scattering angles ranging from 4° up to 56° with an increment of 2°. The energy range varies from -200 to 550 meV with an energy bin of 2 meV. In the present case, scattering angles up to 20° are considered. We will focus mainly on the excitation of the stretching mode. No attempt for multiphonon correction has been made: this contribution is negligible for $q = 0$ and in this study we will reconstruct the density of states in the limit for $q \to 0$.

The analysis will be performed in three steps:

- Multiple Scattering (MS) subtraction;
- Calculation of the Density Of States (DOS);
- Extraction of other physical quantities from the DOS.

5.1 Multiple scattering subtraction

The MS is evaluated by the simple model described in Ref. [96] and [99]. According to that model the MS is described as a double scattering process, neglecting higher order scattering, where a neutron enters into the sample (a slab), suffers a 90° scattering, travels inside the sample, undergoes another 90° scattering and emerges from the sample. This method has the advantage to give a very simple evaluation of the MS, as it can be modeled by a convolution of two Gaussian functions each of which represents a single scattering event. The MS lineshape is then a Gaussian with the parameters defined by the experimental setup (i.e the incident energy defines the center of the Gaussian, and the recoil peak defines its variance). The drawback is that this method is limited to small scattering angles.

The center of the Gaussian function that describes the behavior of the MS is given by the model and it is $2E_i = 1200\ meV$. The standard deviation σ should be measured by detecting neutrons at a scattering angle equal to 90°. The resulting spectra is a Gaussian that is supposed to be self-convoluted to obtain σ. However SEQUOIA does not have access at such high scattering angles so the σ has been evaluated by a fitting procedure.

The fit is done by considering the tails of the spectrum in which no peaks are expected, minimizing the function:

$$\chi^2 = \sum_i \frac{|S(q, E_i) - G(E)|^2}{\epsilon_i^2} , \tag{5.1}$$

where $G(E) = Ae^{-\frac{(E-E_i)^2}{2\sigma^2}}$, with σ as the free fitting parameter and ϵ_i as the uncertainties of $S(q, E_i)$.

The absolute intensity A of the $G(E)$ depends on the normalization of the $S(q, E)$ and on the ratio between the intensities of single and double scattering.

This quantity is available by a formula first proposed by Sears [100] and yields, for the geometry and kinematics of our experiment, to a double scattering with an intensity that is 20% of the total intensity. Then A has been kept fixed in the fit. In figure 5.3 a plot of the experimental data for ice at T= 271 K and for the smallest scattering angles ($\theta = 4°$) is reported together with the evaluation of MS obtained.

The MS is not expected to be phase or temperature dependent. Furthermore the MS can be considered constant for small scattering angles, i. e. for angles up to 20°. Indeed, the model used to evaluate the MS is known to work well only for small scattering angles, so we used $G(E)$ of figure 5.3 to subtract the multiple scattering at all the temperatures and at all the scattering angles up to 20°.

A more rigorous treatment of the MS subtraction would be required if one wanted to use

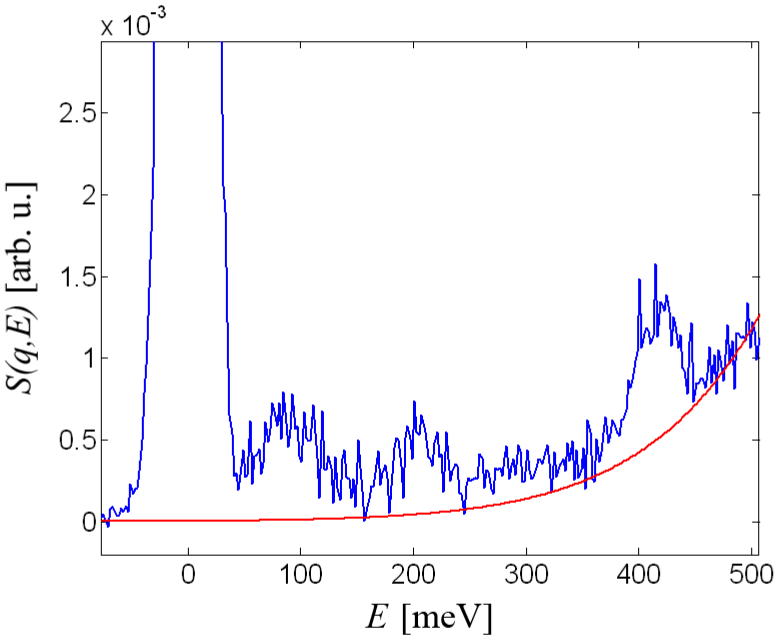

Figure 5.3: *Experimental dynamical structure factor for a scattering angle $\theta = 4°$ (blue line) and MS (red line) calculated with the constraint of 20% of MS.*

data at all the scattering angles and in the whole energy range. In that case a MC simulation should be performed to have a more extensive multiple scattering evaluation.

However, our goal here is to extract the density of the states of the stretching mode so that we only need a subset of energies and θ ranging from 350 meV to 550 meV and from 4° to 20°. In this scattering region the MS subtraction results accurate enough, confirming one of the most important features of INS measurements.

In figure 5.6 is reported a Monte Carlo simulation of the contribution of the multiple scattering for liquid H_2O obtained from a model density of states [138]. As we can see the multiple scattering is expected to have a monotonous behavior in the energy region of our interest justifying the evaluation of the multiple scattering with a Gaussian function.

5.2 Calculation of the density of the states

The INS is a powerful method for determining the Density Of vibrational States (DOS), or frequency distribution function $g(\omega)$ of crystals and amorphous solids [139]. The most serious difficulties arise from the MS subtraction, described in the previous section and from the determination of the separate contribution of different modes, when they overlap. Fortunately, the vibrational modes of H_2O are well separated in energy. In particular the stretching mode,

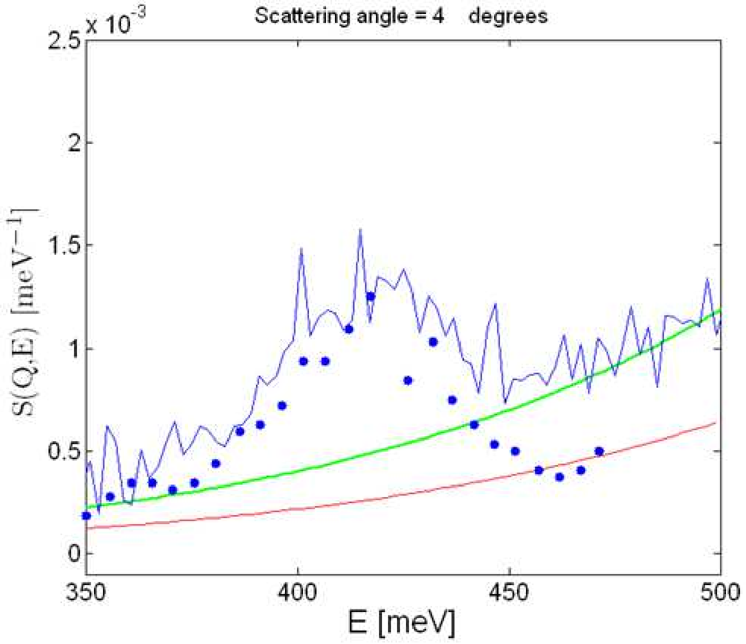

Figure 5.4: *Experimental dynamical structure factor measured in the present experiment (blue line) and from Ref. [96]. The calculated MS fraction of the present data (green line) is the 20 % of the total scattering, while in the data from Ref. [96] (red line) it is the 28%. However, the red line is smaller than the green line: this is a consequence of the incident neutron energy that is 600 meV in the present experiment and 800 meV in that of Ref. [96].*

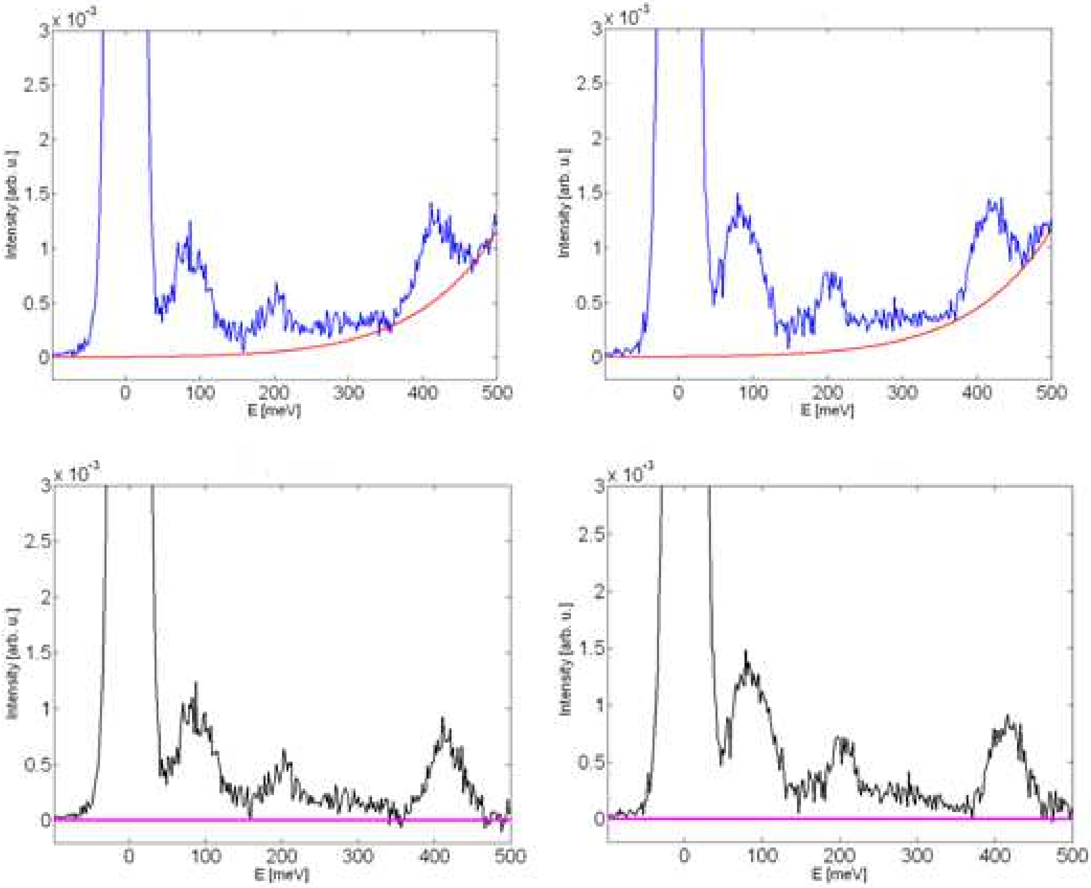

Figure 5.5: *Example of MS subtraction for two spectra recordered on ice at T=271 K, at* $\theta = 6^\circ$ *(left column) and* 8° *(right column) before and after the subtraction.*

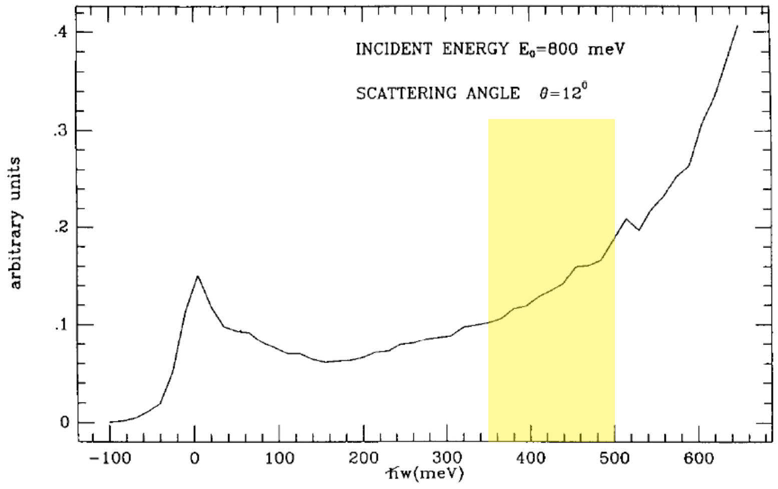

Figure 5.6: *Multiple scattering calculation from Ref. [137]. The shaded area corresponds to the energy range of our interest.*

appearing for ice at E $\approx$ 420 meV, with a width of $\approx$ 80 meV is well separated from the bending mode at $\approx$ 200 meV and a width of $\approx$ 50 meV.

The DOS is obtained as the limit for low q of the function $\frac{S(q,\omega)}{q^2}$, where the dynamical structure factor is corrected for the Debye-Waller factors and other constants. We define the function Γ by the following relation [140]:

$$S(q,\omega) = \frac{1}{k} q^2 \Gamma(q,\omega)\,, \tag{5.2}$$

where:

$$k = \left[\frac{2m\hbar\omega}{e^{-2W}} \frac{4\pi}{\sigma} \frac{1}{n(\omega)+1}\right]\,, \tag{5.3}$$

where $n(\omega)$ is the Bose population factor ($\approx$ 1 for T= 271 K) and e^{-2W} is the Debye-Waller factor. The latter is not far from unity and is estimated considering the mean displacement $< u^2 >$ of the hydrogen to be 0.072 $\mathring{A}^2$. $g(\omega)$ is then calculated as the limit:

$$\lim_{q\to 0} \Gamma(q,\omega) = \lim_{q\to 0} \frac{S(q,\omega)}{q^2} = g(\omega)\,, \tag{5.4}$$

where $\Gamma(q,\omega)$ is expressed as:

$$\Gamma(q,\omega) = g(\omega) + \alpha q^2\,. \tag{5.5}$$

The DOS is calculated considering for each energy value the intensity and the exchanged wave vector q. Then, for each energy, the intensity is reported as a function of q^2. This data set is fitted to the equation 5.5, where $g(\omega)$ and α are the parameters of the linear fit. So for each energy value, we obtain a value of $g(\omega)$ which allow us to reconstruct the DOS as a function of the energy. The data have been rebinned with an energy bin of 6 meV while the raw data have an energy bin of 2 meV. This choice is the best compromise between the energy resolution that is 12-14 meV, in the range 350 - 500 meV of energy loss, and the noise. Figure 5.7 reports $\Gamma(q, \omega)$ for four values of the energy, each of which is plotted as function of q^2.

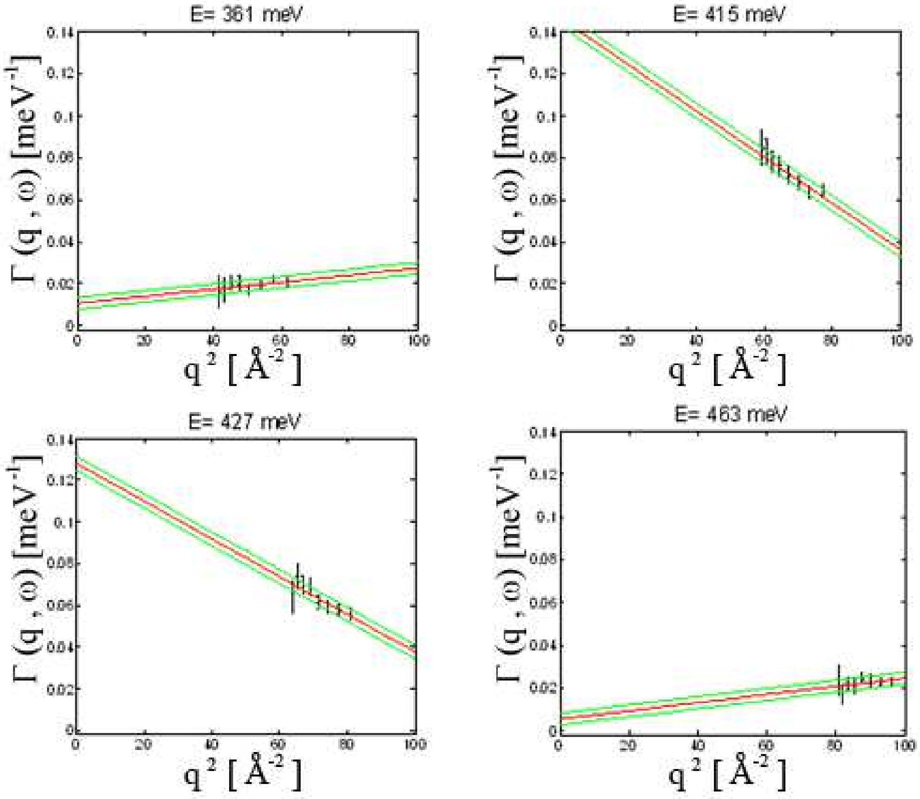

Figure 5.7: $\Gamma(q, \omega)$ *plotted as a function of* q^2 *for some energies. The red line is the least squares linear fit, while the green lines represent the uncertianties of* $g(\omega)$.

The DOS of the stretching mode is then obtained in the energy range from 350 and 480 meV for ice at T = 271 K, and reported in figure 5.8. The integral area of this data is 8.7 ± 0.5 that is very close to the expected value, considering n = 8 stretching modes in a unit cell of ice. In this figure the experimental resolution of the instrument is also reported as a green line.

In order to extract a DOS not altered by the instrumental resolution, the latter should be deconvoluted from the DOS. This can be done considering that the resolution:

- is not q dependent;

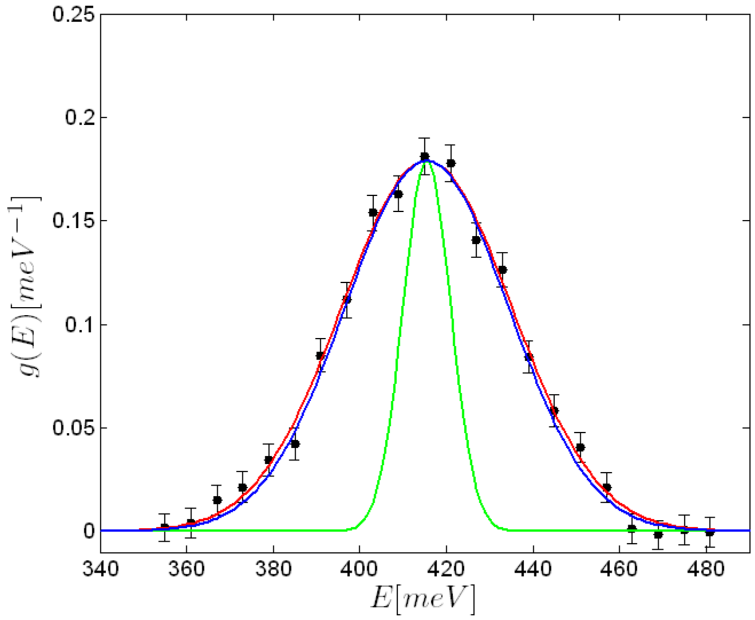

Figure 5.8: *DOS of Ice Ih, black dots with error bars. The red line is the best fit of the data to a Gaussian function, the green line is the instrumental resolution and the blue line is the de-convoluted Gaussian.*

- has a Gaussian behavior;
- is almost constant in the energy range, ranging from 12 to 14 meV.

We do not want to make any assumption on the line shape of the DOS but, in order to have an easy way to calculate the contribution of the instrumental resolution, we can consider that in a first approximation the $O - H$ stretching is harmonic with a Gaussian DOS (the deconvolution of two Gaussian being a Gaussian with a variance that is the difference between the variances). Under these assumptions, a fit to the experimental DOS with a Gaussian has been performed. In figure 5.8 the fit and the result of the deconvolution are reported, as red and blue lines, respectively. It is clearly seen that the instrumental resolution does not change the DOS in a substantial way. The value of the integral area of the DOS and the fact that the peak associated to the stretching mode is much larger than the instrumental resolution suggest indeed that the expected instrumental resolution is very small. Following this procedure the DOS has been calculated at all the temperatures of the experiment.

The Density of states allows us to calculate some other physical quantities. The mean kinetic energy can be found with the following formula:

$$\langle E_K \rangle = \frac{3\hbar}{4} \int_0^{+\infty} \omega g(\omega) \coth \frac{\hbar\omega}{2k_B T} d\omega \,. \tag{5.6}$$

The mean kinetic energy can be expressed as $\langle E_k \rangle = \frac{3}{2} k_B T^*$, where T^* is the effective temperature, first defined by Keer in 1973 [141], as an evaluation of the importance of the zero point motion. In his work he treated the case of liquid Ne, an intermediate system between the He (a quantum system) and the Ar (well described by the classical physic). He found that for a system in which the quantum corrections to the classical values are small, these correction may be obtained by a perturbation calculation in which $\hbar$ is treated as a small quantity. When the correction to order of $\hbar^2$ are incorporated into the momentum distribution function, it still remains a Gaussian function of the momentum, but the temperature parameter T of the classical formula is replaced by the effective temperature $T^* > T$.

T^* is related to the DOS as follows:

$$T^* = \int_0^{+\infty} \omega g(\omega) \coth \frac{\hbar \omega}{2 k_B T} d\omega \, . \tag{5.7}$$

With T^* we can express the harmonic-isotropic momentum distribution as:

$$n(p) = \frac{1}{(2\pi m k_B T^*)^{\frac{3}{2}}} e^{-\frac{p^2}{2 m k_B T^*}} \tag{5.8}$$

In the equations 5.6, 5.7 and 5.8 the harmonic approximation is implicit, because the DOS is defined for harmonic crystals. Furthermore the correct normalization of the $g(\omega)$ is required in all the energy range. The calculation of this quantities thus implies the knowledge of the DOS for ω from 0 to infinite.

The procedure used for the calculation of the DOS can be extended without effort to the entire spectral range. However, as described above, we did not perform a multiple scattering subtraction that can be considered reliable for all energies. Anyway, we can consider the idea of calculating the DOS in the entire spectrum, using the latter only to impose the normalization to unit area and then calculate the $\langle E_k \rangle$ only for the stretching region.

Chapter 6

Results and Conclusions

In this chapter the results of the three experiments will be exposed. In the first section all the experimental results will be shown and commented. In the section that follows we will draw conclusion putting together all the results of the different experiment and then, based on the physical results, the possible future works will be discussed.

6.1 Results

The proton momentum distribution and mean kinetic energy have been measured for ice Ih and Ic, at T=271 K and T=130 K respectively. Vibrational spectra have been also measured for ice Ih at T=271 K and for water at the following temperature: 269, 271 (supercooled water), 273, 275, 276, 278, 280, 285, 290, 296, K.

6.1.1 Proton momentum distribution and mean kinetic energy of ice Ih

Proton momentum distribution in Ice Ih, at T= 271 K, has been obtained from DINS data recordered with the VESUVIO spectrometer. The momentum distribution is related to the NCP via the relation 3.10 shown in chapter 2 that we recall for the sake of simplicity:

$$n(p) = \frac{e^{-\frac{p^2}{2\sigma^2}}}{(\sqrt{2\pi}\sigma)^3}\left[1+\sum_n c_n(-1)^n L_n^{\frac{1}{2}}\left(\frac{p^2}{2\sigma^2}\right)\right] \tag{6.1}$$

The radial $4\pi p^2 n(p)$, where $n(p)$ is obtained with the equation 6.1 (M1 model), is shown in figure 6.1, plotted as blue line.

The M2 model, with $n(p)$ described by the momentum distribution of equation 3.11:

$$n(p) = \left\langle \frac{1}{\sqrt{8\pi^3}\sigma_z\sigma_y\sigma_x} \exp\left(-\frac{p_z^2}{2\sigma_z^2}-\frac{p_y^2}{2\sigma_y^2}-\frac{p_x^2}{2\sigma_x^2}\right)\right\rangle_\Omega \tag{6.2}$$

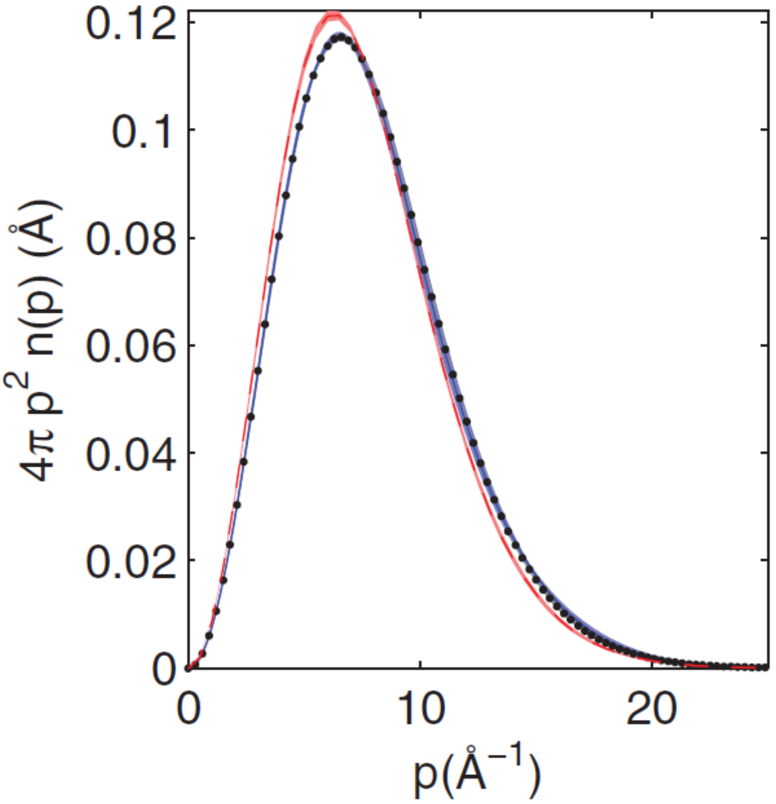

Figure 6.1: *Experimental radial momentum distribution for ice at 271 K obtained using model M1 (blue solid line), M2 (black dots) and PICPMD for ice at 269K (red dashed line) with error bars. Errors on the radial momentum distribution, for both M1 and M2, are very small: they are determined from the parameters covariance matrix calculated by the fitting codes.*

is instead represented by the black dots. In this figure is also reported the radial proton momentum distribution obtained by the PICPMD. The M2 model fits to the experimental data just as well as the M1 model, confirming that the added bias does not worsen in any way the quality of the fit. The values of the fitting parameters of the M1 and M2 model, and the PICPMD frequencies are reported in table 6.1.

Model	σ $[\AA^{-1}]$	a_2	ω_z $[cm^{-1}]$	ω_x $[cm^{-1}]$	ω_y $[cm^{-1}]$	$\langle E_k \rangle$ $[meV]$
M1	4.99 ± 0.03	0.10 ± 0.01	-	-	-	156 ± 2
M2	-	-	2795 ± 95	1230 ± 110	920 ± 80	154 ± 2
PICPMD	-	-	2640 ± 60	1160 ± 25	775 ± 20	143 ± 2

Table 6.1: *Values of the fitting parameters used in M1 and M2 model. PICPMD frequencies are reported for comparison. The relation among the fitting parameter σ_i of the M2 model and the ω_i is reported in the equation 6.3.*

In the case of the spherically averaged multivariate Gaussian, or M2 model, there is, however, a difficulty since optimization gives nearly degenerate σ_x and σ_y values leaving the error bars on the effective frequencies poorly defined. This reflects the presence of too many fitting parameters for the information content of the (spherically averaged) data set. Indeed the difficulty would disappear by adopting a model with only two distinct parameters (σ_z and $\sigma_t = \sigma_x = \sigma_x$ in the transverse direction) as done in a previous study [84], but this would not be an accurate description of the physics. Rather than following this approach, in the M2 model we retain three distinct σ_i and eliminate the degeneracy by adding a weighting term in the least square fit of the experimental Compton profiles, to minimize the deviation of the fitted σ_i from their PICPMD counterparts. The magnitude of the weighting term reflects the assumed physical ranges for the σ_i or equivalently, the ω_i.

However, σ_x and σ_y should be distinct from each other, as they reflect distinct averaged information on the bending and the libration frequencies of the vibrational spectrum. Such anisotropic behavior in the spherical momentum distribution is largely suppressed by the spherical averaging operation. Thus to obtain distinct σ_x and σ_y values from the spherically averaged momentum distribution, a significantly higher resolution would be needed than those currently available with state-of-the-art facilities and instrumentation. Although in the future it will be possible to reach the required resolution, at present the only way to acquire directional information from experiments on macroscopically isotropic samples such as polycrystalline ice, is to use prior knowledge on the distribution in the fitting procedure. In this respect, PICPMD simulations are a reliable source of theoretical knowledge, since

- they predict momentum distributions in good agreement with experiment;

- they are a parameter-free approach in which the only physical approximation is associated to the adopted electronic density functional.

Values of the PICPMD frequencies are taken from [101] and are reported in table 6.3. The corresponding σ_i values are given by the relation:

$$\hbar^2\sigma_i^2 = \frac{M\hbar\omega_i}{2}\coth\frac{\hbar\omega_i}{2k_BT}, \tag{6.3}$$

that yields $(\sigma_z)^{PI} = 6.28$ $\AA^{-1}$, $(\sigma_x)^{PI}= 4.18$ $\AA^{-1}$, and $(\sigma_y)^{PI}= 3.46$ $\AA^{-1}$.

Assuming that the deviation of the actual σ_k^2 from $(\sigma_k^2)^{PI}$ follows a Gaussian probability distribution with standard deviation $\Delta\sigma_i^2$, one has a probability to find a certain σ_k^2 value that is:

$$P(\sigma_k^2) \propto e^{\frac{[\sigma_k^2-(\sigma_k^2)^{PI}]}{2(\Delta\sigma_k^2)^2}}. \tag{6.4}$$

$\Delta\sigma_i^2$ reflects the the uncertainty of σ_i^2, which depends on the likelihood interval suggested by physics and the experimental resolution. In our fit we take $\Delta\sigma_z^2 = 3.0$ $\AA^{-2}$, $\Delta\sigma_y^2 = 1.5$ $\AA^{-2}$ and $\Delta\sigma_x^2 = 1.2$ $\AA^{-2}$.

These values correspond to the following 70 % confidence intervals for the principal frequencies ω_k:

$$\begin{aligned} \omega_z &\in [2430, 2830]cm^{-1}, \\ \omega_y &\in [1060, 1265]cm^{-1}, \\ \omega_x &\in [680, 860]cm^{-1}. \end{aligned} \tag{6.5}$$

The assumed distribution for σ_k^2 6.4 is used as prior information in the maximum likelihood method [142], yielding a modified objective function to be minimized:

$$\chi^2(\sigma_x^2, \sigma_y^2, \sigma_z^2) = \sum_l\sum_i \frac{\left(F_l^{th}(y_i, q_i) - F_l(y_i, q_i))\right)^2}{\epsilon_{l,i}^2} + \sum_{k=x,y,z}\frac{\left[\sigma_k^2 - (\sigma_k^2)^{PI}\right]^2}{2(\Delta\sigma_k^2)^2}. \tag{6.6}$$

The results of this fit are shown in table 6.3. The relatively large error bars reflect the estimates for the physical range made in the fit.

The blue shifts of the experimental frequencies relative to their PICPMD counterparts suggest that the experimental $n(p)$ should be slightly more spread out than its theoretical counterpart, an outcome that is entirely borne out by the plot of the PICPMD radial momentum distribution reported in figure 6.1.

Interestingly, the comparison between PICPMD and the present more accurate experiment reverses the trend observed in the comparison with the previous experiment of Ref. [84]: the proton is now more localized in the experiment than in the calculation, consistently with the delocalization error of common density functional theory approximations [143]. Indeed, as pointed out in the introduction, the momentum distribution derived in [84] should not be considered reliable due to lack of data reduction.

The effect can be quantified in terms of $\langle E_k \rangle$, which is $156 \pm 2\ meV$ with the M1 fit and $154 \pm 2\ meV$ with the M2 fit, as opposed to $143 \pm 2\ meV$ in PICPMD. The relative lack of sensitivity of the spherical momentum distribution to the anisotropy of a system characterized by three distinct quasi-harmonic frequencies confirms a recent theoretical study [3], in which a more sensitive quantity named mean force was proposed. For a macroscopically isotropic system, the latter is a function of the radial displacement x. The mean force is defined as:

$$f(x) = (-\log n(x))' - \frac{Mx}{\beta\hbar^2}. \tag{6.7}$$

Here $n(x)$ is the spherical end-to-end distribution, i.e., the Fourier transform of $n(p)$ (equation 6.2), while the second term is the free particle contribution which is independent on the environment; $f(x)$ can be directly related to the experimental $\bar{J}_{IA}(y)$ data obtained after correcting the NCP data $\bar{F}(y)$ for the final state effects $\Delta J(y,q)$. The corresponding expression is [3]:

$$f(x) = -\frac{Mx}{\beta\hbar^2} + \frac{\int_0^{+\infty} dy y \sin xy/\hbar \bar{J}_{IA}(y)}{\hbar \int_0^{+\infty} dy \cos xy/\hbar \bar{J}_{IA}(y)}. \tag{6.8}$$

The mean forces extracted from $\bar{J}_{IA}(y)$, from M2, and from PICPMD data are plotted in figure 6.2.

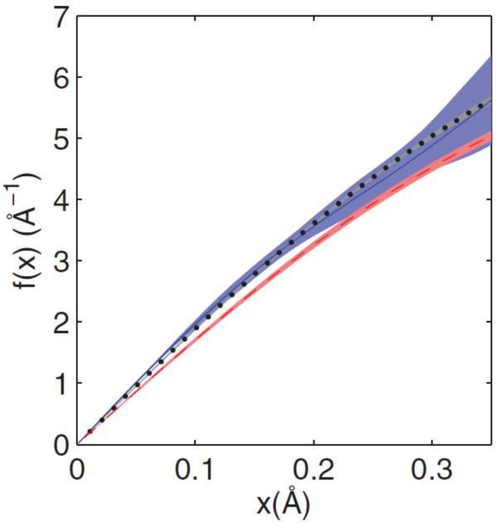

Figure 6.2: *Mean force, with error bars, calculated directly from the experimental asymptotic Compton profile, $\bar{J}_{IA}(y)$ (blue solid line), M2 (black dots), and PICPMD data (red dashed line).*

The three mean forces have good correspondence and $f(x)$ extracted from the raw experimental data is particularly close to that of the M2 model, indicating that the quantum state of the proton in ice is well represented by quasi-harmonic anisotropic motion. Notice that the error bars of $f(x)$ increase systematically with the displacement x, reflecting a progressively larger statistical uncertainty as the tail of the end-to-end distribution is approached; $f(x)$ is related to the derivative of the Fourier transform of the NCP, and therefore, at large x, becomes sensitive to its highest frequency components, i.e., to the noise. The effect becomes so pronounced in the raw $f(x)$ that we truncate the plot at 0.35 $\AA$. The $\langle E_k \rangle$ estimated, in a fourth, non parametric way, from the raw $f(x)$ is $156 \pm 9\ meV$. The error bar of this estimate is larger than that from M1 or M2, since the raw mean force constitutes a model independent, nonparametric approach. To accurately resolve the anisotropic frequencies without resorting to a model dependent approach, the counting statistics in the experiment, i.e., the uncertainty of the raw $f(x)$ should be comparable to that of the M2 model in figure 6.2.

All these results can also be found in Ref. [144].

M2 model applied to DINS data recordered on water

In two previous works [81, 82], DINS measurements on water at various temperatures has been performed. In both experiments data were analyzed only using the M1 model, well reproducing the experimental data. Fitting these data using the M2 model can give further information on the role of anharmonicity with respect to the anisotropy of the momentum distribution.

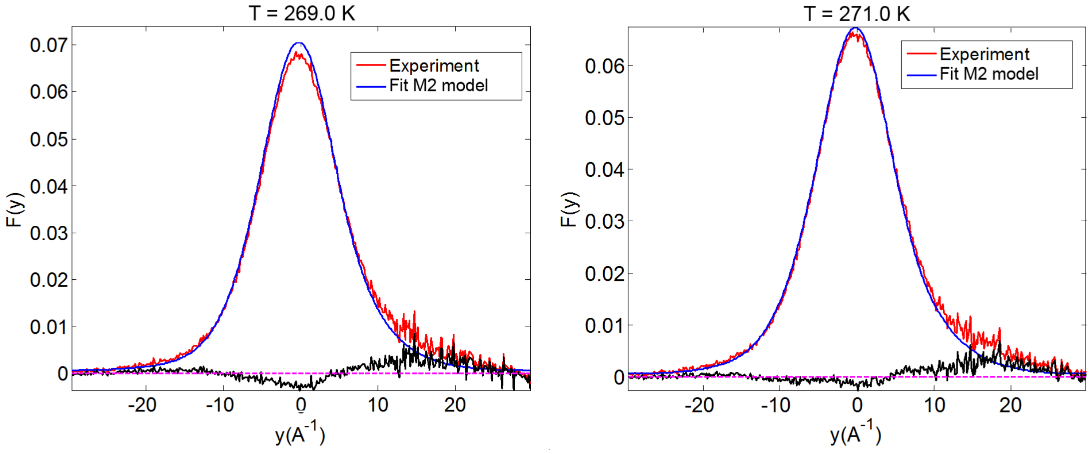

Figure 6.3: *Angle averaged NCP, $\bar{F}(y)$, and its best fit using M2 model for supercooled water, at T= 269 and 271 K. The fits cannot reproduce satisfactory the experimental data, indicating a large anharmonic contribution.*

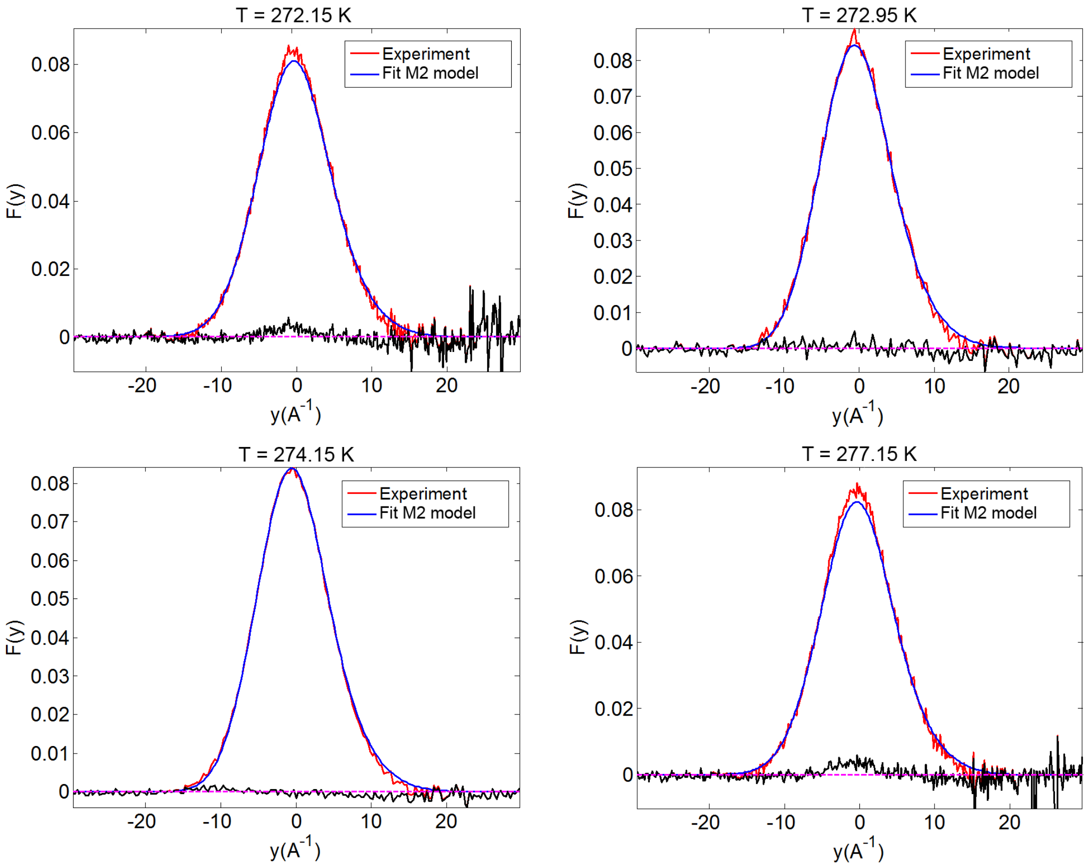

Figure 6.4: *Angle averaged NCP, $\bar{F}(y)$, and its best fit using M2 model for water. The fit residuals indicate that an anharmonic contribution is still present and non negligible for T = 272.15 K (supercooled phase) and T =277.15 K (the temperature of maximum density of water). Data at T= 272.95 K and 274.15 K are well represented by an harmonic-anisotropic model.*

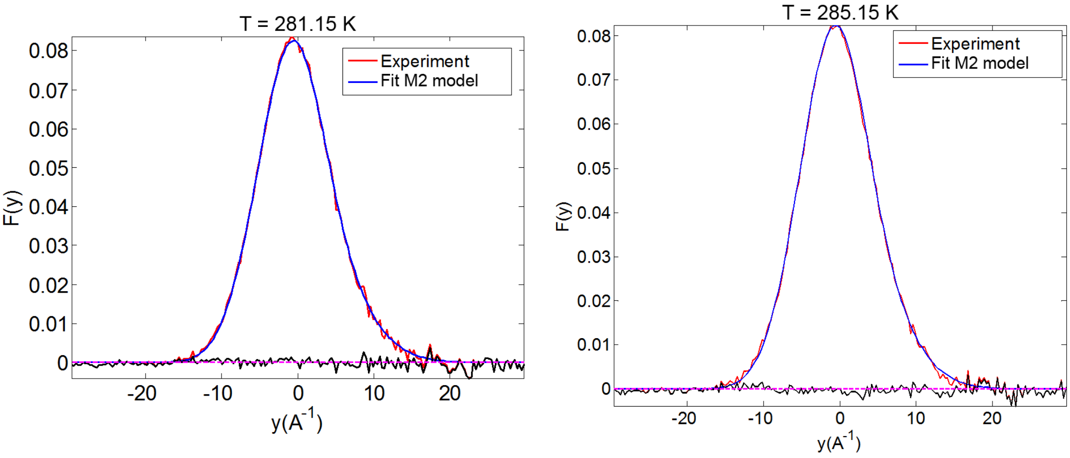

Figure 6.5: *Angle averaged NCP, $\bar{F}(y)$, and its best fit using M2 model for water. The proton momentum distribution of water near the room temperature is well represented by an harmonic anisotropic model.*

In figures 6.3, 6.4 and 6.5, the best fit using the M2 model compared to the experimental $\bar{F}(y)$ is shown for all available temperatures. We must point out that the fit with three different σ_i as free parameters can be done only in the case of a prior knowledge on these parameters as in the case of ice Ih. In performing these fits we did not try to make any guess on the prior, instead we used the same of the ice, in the assumption that the principal frequencies of water do not vary dramatically from those of ice. Anyway, for this reason, this part of the data analysis should be considered reliable only in a qualitative way.

As a result anharmonicity effects seem to be not negligible for the supercooled water and for water at the temperature of maximum density, T = 277.15 K, while the water around room temperature can be well represented by an harmonic anisotropic model. The behavior of the $\langle E_k \rangle$ as a function of the temperature is still preserved, only a rigid shift of the $\langle E_k \rangle$ value is evident towards smaller values for the stable water and towards larger values for supercooled water, with the relative maximum at T=277.15 K and the absolute maximum at T=271 K, as shown in figure 6.6.

6.1.2 Proton momentum distribution and mean kinetic energy in ice Ic

Proton momentum distribution in Ice Ic at T= 130 K, has been obtained from DINS data recordered on the VESUVIO spectrometer. The NCP of the oriented ice sample at $\alpha = 0°$ is reported in figure 6.7, together with the NCP of the polycrystalline ice. In this case remarkable differences between the two spectra can be observed.

Each experimental NCP was fitted simultaneously in the y-space, with the M1 paramet-

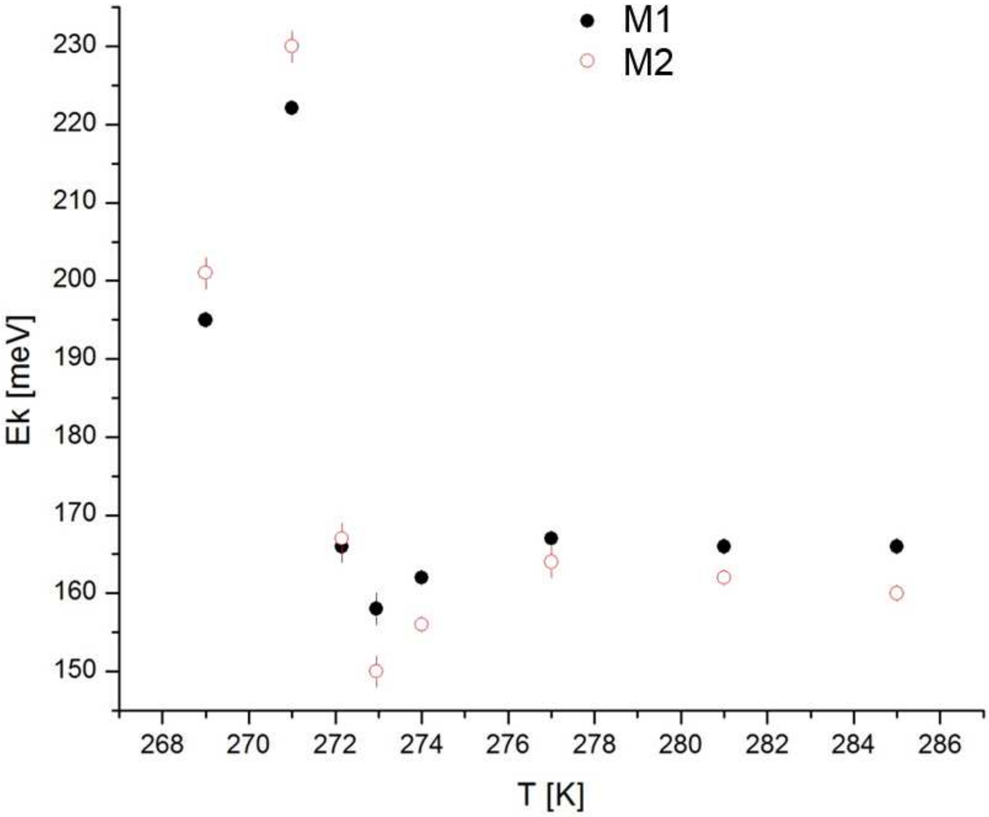

Figure 6.6: *Mean kinetic energy of the proton, $\langle E_k \rangle$ for liquid water as a function of the temperature. Values obtained with M1 and M2 model are compared. The M2 model underestimates the $\langle E_k \rangle$ for the temperatures at which the system is well described by an anisotropic harmonic model. Instead, when the M2 model fails, the $\langle E_k \rangle$ is overestimated with respect to the M1 model. This effect can be explained as follows: if the tail of the momentum distribution does not go to zero as a Gaussian distribution, the M2 model yields larger σ_i values, corresponding to a larger $\langle E_k \rangle$.*

ric model, to determine the mean kinetic energy $\langle E_k \rangle$, without taking into account the $\hat{q}$ orientation respect to the sample orientation. The resulting value of $\langle E_k \rangle$ are listed in table 6.2. For both orientations the experimental NCP data sets, recorded with the left and right detectors, have been fitted separately.

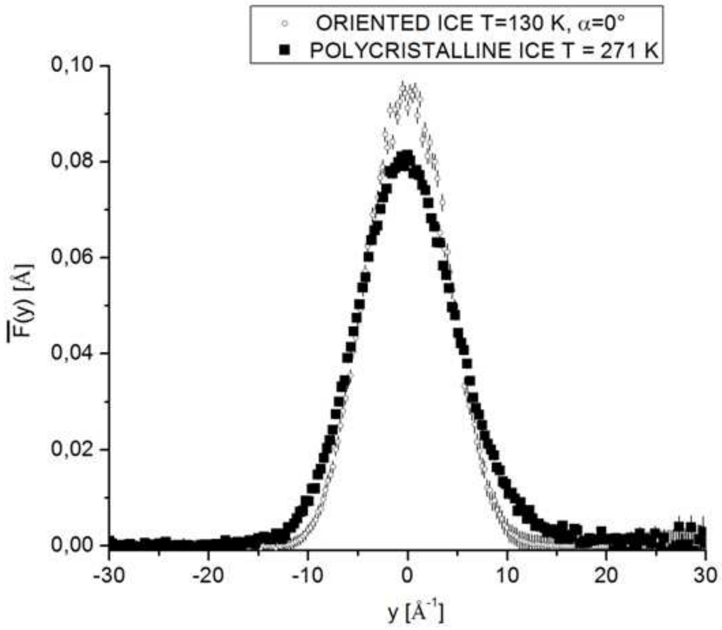

Figure 6.7: *Comparison between angle-averaged NCP, $\bar{F}(y)$, for polycrystalline ice at T = 271 K (full squares) and oriented ice for $\alpha = 0°$ orientation (open circles).*

The $\langle E_k \rangle$ values are considerably lower than the zero point kinetic energy of the proton of ice Ih. The concept of the zero point kinetic energy arises from the ground state of an harmonic oscillator, that is not equal to zero, but it has an energy equal to $\frac{1}{2}\hbar\omega$ [145]. In general a DINS measurement at T very close to zero yields the zero point kinetic energy of the target particle. In the case of the proton in ice and water, the $\langle E_k \rangle$ is almost completely due to its zero point motion, due to its small mass, as measured by Reiter [146] for polycristalline ice Ih at T= 5 K, yielding $\langle E_k \rangle = 142\ meV$. In that work the authors also performed a DINS experiment for H_2O in nanotubes at T = 5 K, finding $\langle E_k \rangle = 104\ meV$.

The simultaneous fit of all the spectra yield a momentum distribution that can be considered very close to spherically averaged distribution as the case of a liquid or a polycristalline sample. In fact, not only we are probing the $n(p)$ in a wide range of direction, considering the angular range of detection, but also the different orientations of the H_2O molecules in a monocrystalline sample with respect to the incoming neutrons, gives rise to a momentum probed along different directions. This is indeed confirmed by the $\langle E_k \rangle$ values obtained from

T $[K]$	Sample	α [degrees]	Detectors	$\langle E_k \rangle$ $[meV]$
271	Polycrystal	-	All	156 ± 2
130	Oriented Ice	0	All	101 ± 1
130	Oriented Ice	30	All	100 ± 1
130	Oriented Ice	0	Left side only	99 ± 2
130	Oriented Ice	0	Right side only	103 ± 3
130	Oriented Ice	30	Left side only	98 ± 1
130	Oriented Ice	30	Right side only	102 ± 1
130	Oriented Ice no Pt	0	All	105 ± 1

Table 6.2: *Mean proton kinetic energy for oriented and polycrystalline ice, obtained with the M1 model.*

measurements at different α values.

We gather that the small structural differences between the Ice Ic and the ice Ih produce a large discrepancy between their proton $\langle E_k \rangle$. Even if this result was unexpected, it should not considered to much surprising. Indeed the same phenomenology, not only can be found in the case the ice Ih in nanotube, but also in the case of the supercooled water previously described. The $\langle E_k \rangle$ of the supercooled water has an excess with respect to water above 0 °C that is $\approx$ 50% of the kinetic energy in the stable phase. Neutron diffraction measurements [147] of supercooled water showed a very tiny difference between the peaks of the radial $O-O$ distribution of the water at T = 269 K and T = 289 K: the maxima of these peaks were found to be at 2.70 and 2.76 $\mathring{A}$, respectively. Despite this little discrepancy the proton momentum distribution of water changes dramatically. We still do not have enough information to establish a direct and quantitative correlation among structural discrepancies and the $\langle E_k \rangle$ behavior, but it could be useful to remark this parallelism in different phases of water.

Finally, the measurement of the sample without the Pt substrate yields a slightly larger value of $\langle E_k \rangle$. This allows us to conclude that the presence of the Pt substrate does not alter dramatically the measurements.

The statement according to which we are probing the momentum distribution only along a single direction is not strictly correct. We are in fact probing the momentum distribution in a set of directions describing a cone. The aperture of this cone is inversely proportional to the exchanged wave vector: as explained in chapter 4, the larger is the q the closer to the c-axis is the probed direction. The constant $\hat{q}$ analysis of the data at $\alpha = 0°$ and 30° give the results reported in the table 6.3, where β is the angle between $\hat{q}$ and the c-axis.

The constant q direction analysis seems to give a kind of $\langle E_k \rangle$ distribution as a function

β [degree]	$\langle E_k \rangle$ $[meV]$
130 ± 10	105 ± 1
150 ± 10	99 ± 1
180 ± 10	94 ± 1

Table 6.3: *Mean kinetic energy of proton, $\langle E_k \rangle$, calculated from the momentum distribution probed along the direction forming an angle β with the c-axis.*

of β. Thus moving from a wave vector direction parallel to the c axis towards a direction perpendicular to it the mean kinetic energy of the proton increases. However, to obtain these three values we had to select our data point with an interval of $\beta = 20°$. This requirement has been imposed by the need to have a suitable number of points of $F(y)$.

These data have also been analyzed with the harmonic M2 model of $n(p)$ and the resulting values of $\langle E_k \rangle$ are reported in the table 6.4. Fitting the data with 2 or 3 harmonic components yielded degenerate values and, as a consequence, very large error bars. The data can instead be fitted with only one component giving $\langle E_k \rangle$ values compatible with the previous fit. The resulting proton momentum distribution is thus harmonic and isotropic. In figure 6.8 the experimental NCP is reported for α=0°.

α [degree]	σ $[\AA^{-1}]$	$\langle E_k \rangle$ $[meV]$
0	4.02 ± 0.02	100 ± 1
30	4.00 ± 0.02	99 ± 1

Table 6.4: *Mean kinetic energy of the proton for $\alpha = 0°$ and 30° resulting from the M2 model.*

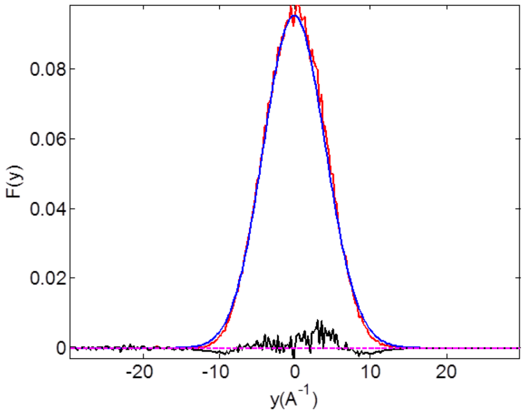

Figure 6.8: *Angle averaged NCP, $\bar{F}(y)$, for $\alpha = 0°$ (red line), its corresponding best fit (blue line), using the M2 model, and their difference (black line).*

6.1.3 Vibrational spectroscopy

Vibrational spectra of a sample of pure H_2O in the liquid stable phase at T = 275, 276, 278, 280, 285, 290 and 296 K, in the liquid metastable phase (supercooled water) at T = 269, 271 and 273 K and in solid phase (ice Ih) at T = 271 K have been obtained from measurement at SEQUOIA spectrometer with an incident neutron energy of 600 meV.

It is useful to show the raw spectra for some of these temperatures (for the three different phases in which H_2O has been measured). As described in chapter 5, the MS has been evaluated from ice at T=271 K and subtracted for spectra at all other temperatures. So the MS correction is the same for all spectra.

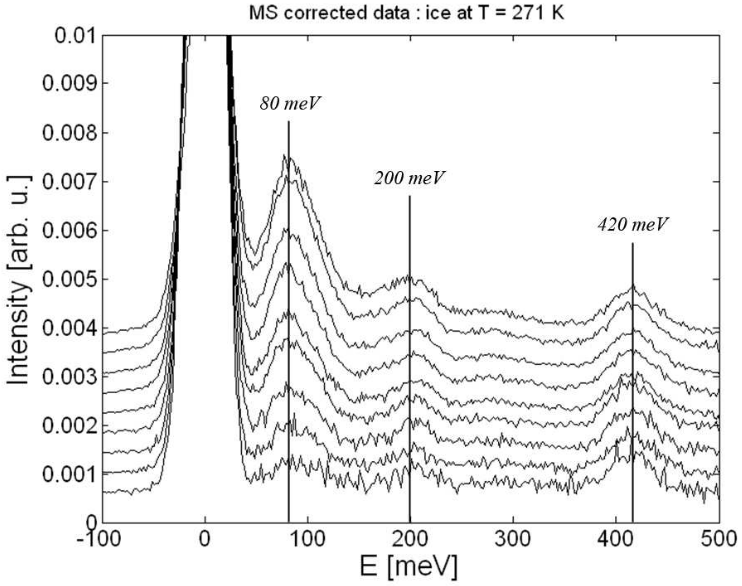

Figure 6.9: *Raw data corrected for the multiple scattering: ice at T = 271 K. Each line represents a scattering angle, from 4° to 20° (with an increment of 2°), from bottom to up. The vertical lines are an estimation of the vibrational energies of the ice. They result to be* E_{lib} *= 80 ± 10,* E_{ben} *=200 ± 10 and* E_{str} *420 = ± 10.*

In figures 6.9, 6.10 and 6.11 the vibrational spectra of ice at T = 271 K, supercooled water at T = 271 K and water at room temperature, respectively, are shown. In these figures are also indicated the approximate values of the three peaks corresponding to the H_2O vibrational modes. The uncertainties of these values are estimated to be around 10 meV. A comparison among the values in different phases shows that the principal frequencies do not vary within the range of investigated temperatures for liquid water. Instead, the principal frequencies of ice appear at lower energies. A direct comparison among the frequency values can be done with the results obtained from DINS and PICPMD. Frequencies are reported in table 6.5 in

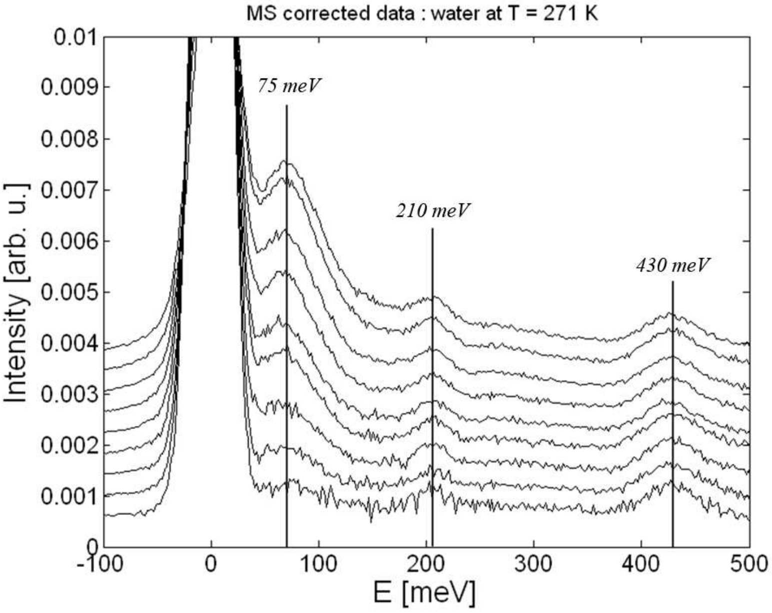

Figure 6.10: *Raw data corrected for the multiple scattering: water at* $T = 271$ *K. Each line represents a scattering angle, from* 4° *to* 20° *(with an increment of* 2°*), from bottom to up. The vertical lines are an estimation of the vibrational energies of the ice. They result to be* $E_{lib} = 75 \pm 10$, $E_{ben} = 210 \pm 10$ *and* $E_{str}\ 430 = \pm 10$.

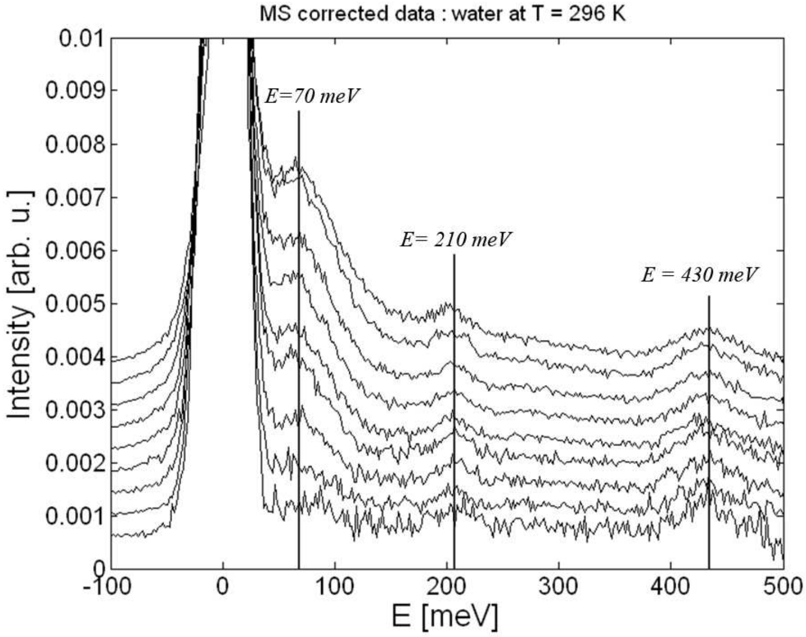

Figure 6.11: *Raw data corrected for the multiple scattering: water at T = 296 K. Each line represents a scattering angle, from 4° to 20° (with an increment of 2°), from bottom to up. The vertical lines are an estimation of the vibrational energies of the ice. They result to be* E_{lib} *= 70 ± 10,* E_{ben} *=210 ± 10 and* E_{lib} *430 = ± 10.*

cm^{-1} unit.

	ω_z $[cm^{-1}]$	ω_x $[cm^{-1}]$	ω_y $[cm^{-1}]$
INS	3390 ± 80	1610 ± 80	640 ± 80
DINS	2795 ± 95	1230 ± 110	930 ± 80
PICPMD	2640 ± 60	1160 ± 25	775 ± 25

Table 6.5: *Principal frequencies of ice Ih*

The INS frequencies are not consistent with DINS and PICPMD ones. This is because PICPMD values are calculated taking into account the fact that the principal frequencies are obtained as the combined contribution of modes and they are the effective frequencies of a quasi-harmonic model. For example ω_x has two contributions that are ≈ 50 % bending and 50 % libration and ω_z is not completely due to the stretching (even if it is ≈ 97 % due to the stretching motion). The DINS values are indeed been obtained from prior knowledge of the PICPMD frequencies.

The most interesting feature arising from figures 6.10 and 6.11 is that the vibrational spectrum of water does not change appreciably passing through the supercooled to stable phase up to the room temperature. This is a surprising result because, as previously stressed, the dynamical behavior of the supercooled water is very different with respect to that of the water above the melting point.

In figure 6.12 the raw data difference of water at T=271 K and at room temperature is reported. As we can see no appreciable discrepancy arises among the spectra, except for some features at low energy. We want to emphasize that, in the stretching region, the vibrational spectrum at these two temperatures does not change. This comparison can be made among all other temperatures with the same conclusions. Here we decide to report the comparison of water at T=271 K and room temperature because they present the major differences for what concerns the momentum distribution. Instead, small discrepancies appear if we sum up all the spectra at all the angles, also considering angles above 20°.

In figure 6.13 we sum up, for each temperature, the spectra at all the available angles, from 4° to 54°. These are raw data, apart for the standard corrections available on SEQUOIA spectrometer, reported in an energy range around the stretching region. We are looking for discrepancies, in the vibrational spectra around the stretching peak, among supercooled and room temperature water, because it has been proposed that the different behavior of the proton along the stretching is due to a variation of the potential, passing through the metastable phase to the stable one. This effect could allow the tunneling of the protons between two minima of a double well potential [81, 82]. The different behavior of the supercooled water spectra with respect to water at room temperature cannot however explain the large

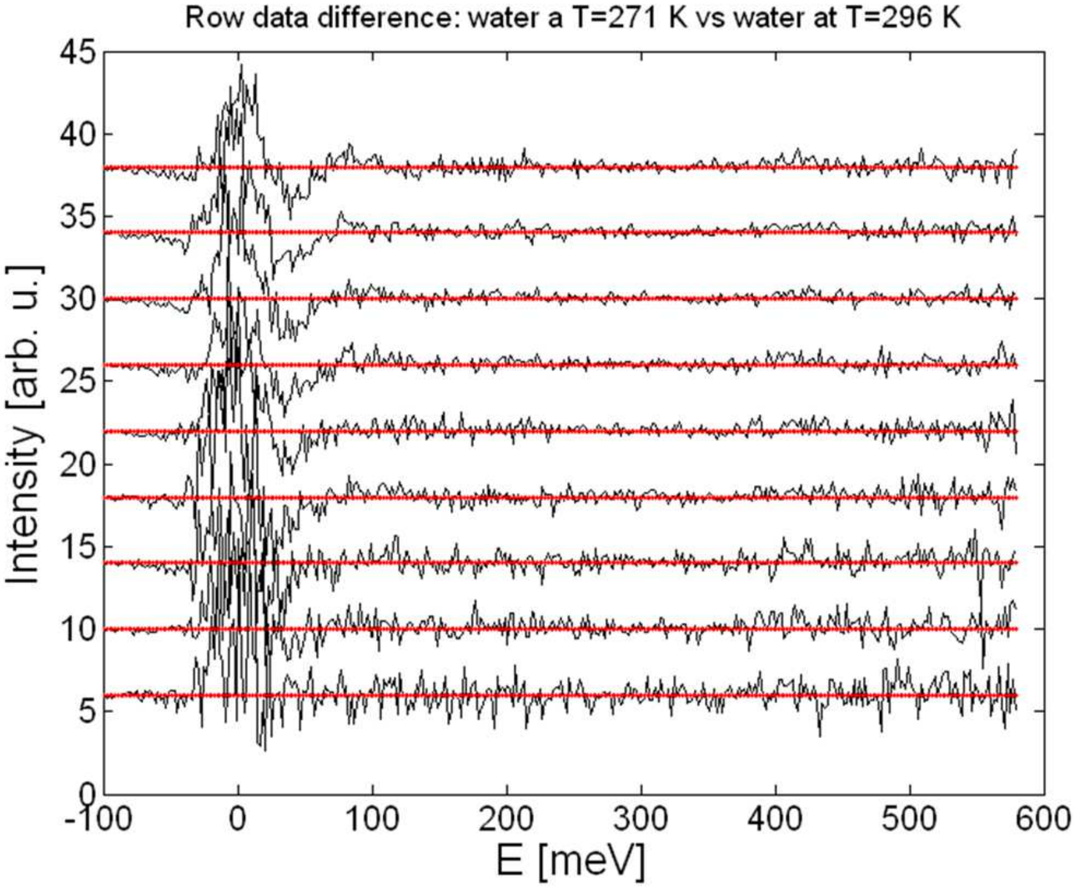

Figure 6.12: *Difference between raw data for water at room temperature and supercooled water at scattering angles from 4° to 20° (from bottom). It is clear that the vibrational spectrum of water does not vary passing through* $T = 271$ *K to 296 K. Small differences arise for very low energy loss values, but these discrepancy cannot account for the difference between the supercooled water and the water at room temperature momentum distributions.*

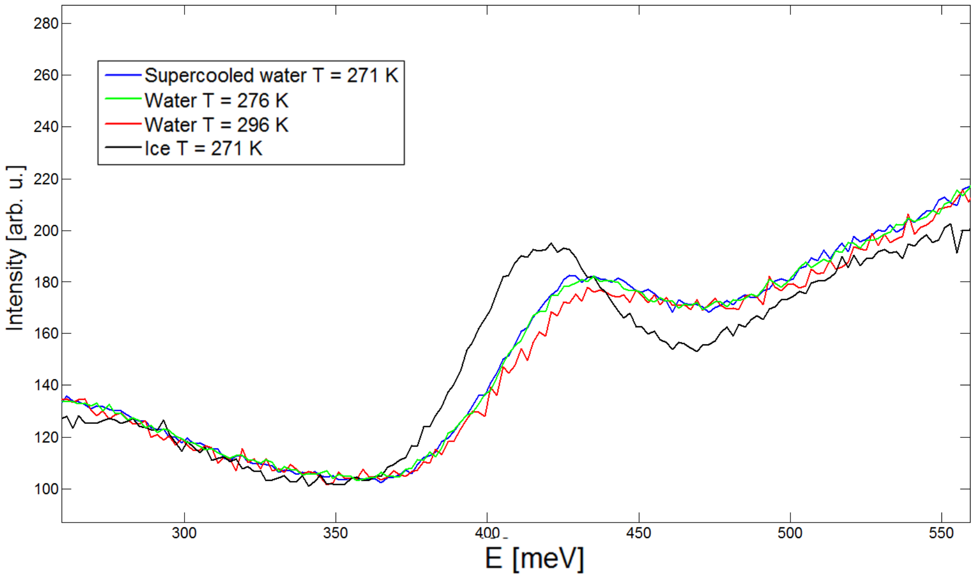

Figure 6.13: *Summation of data at scattering angle from 4° to 54°, for ice, water and supercooled water, around the stretching peak. If we sum up all the data we are much more sensible to any difference among the vibrational spectra. In this plot a tiny difference in the stretching region of the vibrational spectrum between water at* T *= 271 K and 296 K is visible.*

difference among momentum distributions and no clear evidence of any modification of the stretching mode can be seen.

The density of states has also been extracted from these spectra for all temperatures in the stretching region, i.e. E from 350 to 480 meV for ice and from 350 to 500 meV for water. The spectra have been normalized to unity in this energy range: this normalization should give a DOS with an integral that is the total number of stretching modes n, considering 4 molecules in a unit cell. The expected value is n =8, for ice Ih.

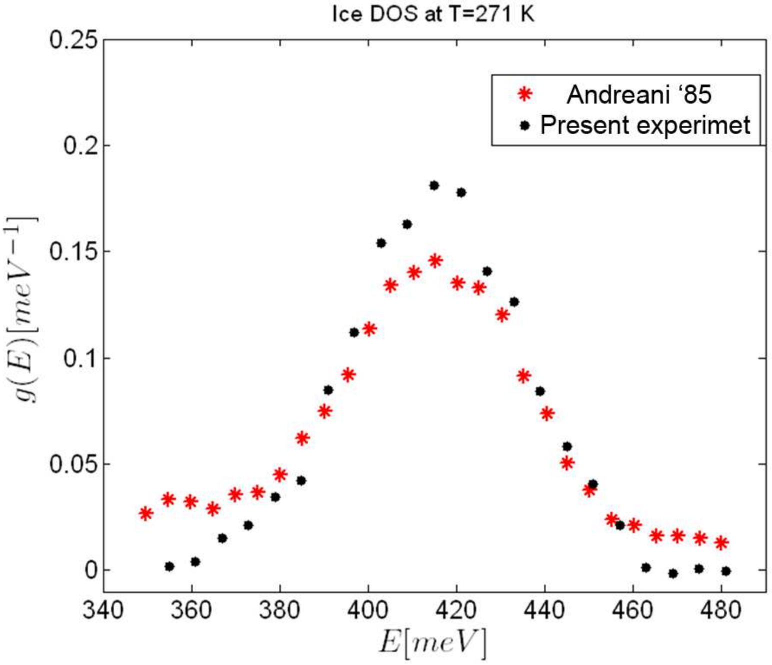

Figure 6.14: *Density of states for ice Ih at T = 271 K. The result of the present experiment is reported with black dots, the result of Ref. [96] is reported as red asterisk. The energy bin is 6 meV in both cases. The line shape of the DOS from Ref. [96] is larger than the DOS of the present experiment: this is due to the smaller energy resolution of SEQUOIA. The larger intensity of the tails of the former could be due to a not reliable MS subtraction. In this respect a fit of the MS lineshape represents an improvement with respect to the simple model described in Ref. [96].*

In figure 6.14 the DOS for ice Ih at T=271 K is reported together with the DOS calculated in Ref. [96] for comparison. The higher resolution of the present experiment results in as a DOS that is sharper with respect to the previous experiment. As expected, both distributions are centered at approximately the same energy value E = 417 and (415.5 ± 0.5) meV for Ref. [96] and present data, respectively. The integral area of this data is 8.7 ± 0.5 that is very close to the expected value.

The DOS of water has been obtained in the same way as that of the ice. In figure 6.15 is reported the DOS of ice compared with the DOS of the supercooled water at T=271 K. It is visible that the spectrum associated to the the supercooled water DOS is broader and it is peaked at E=425 meV.

As we saw in the raw data, and as expected after considering that the raw vibrational spectra for water do not change appreciably in the whole temperature range, we obtain several equivalent DOS. In figure 6.16 we can see that the $g(E)$ for water are comparable among each other within the error bars (the latter are not reported in figure 6.16, but are all of the same order of magnitude as in figure 6.15 and 6.17).

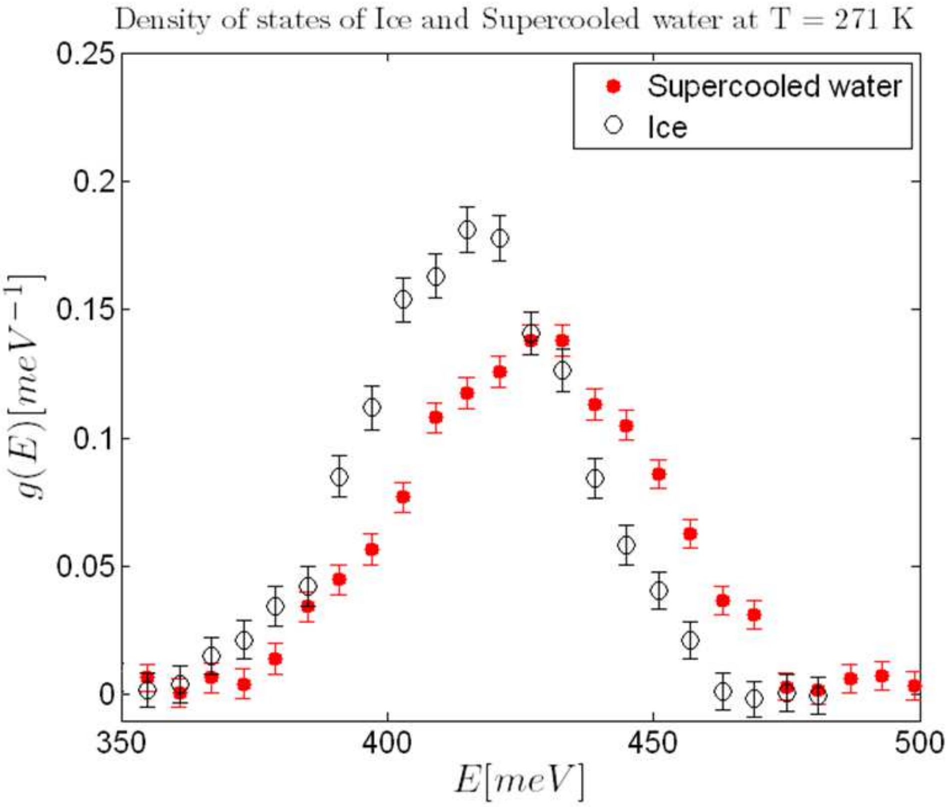

Figure 6.15: *Comparison of the DOS of supercooled water and ice Ih at T = 271 K, with error bars. As expected the DOS of ice is shifted at lower energy (its maximum being at 415.5 ± 0.5 meV) with respect to that of the supercooled water (425.5 ± 0.5 meV).*

If the density of states is known for all energies it is possible to calculate the mean kinetic energy assuming the motion to be harmonic for all the modes. The relation between the $\langle E_k \rangle$ and $g(E)$ is shown in the equation 5.6. The same equation with the integral going from

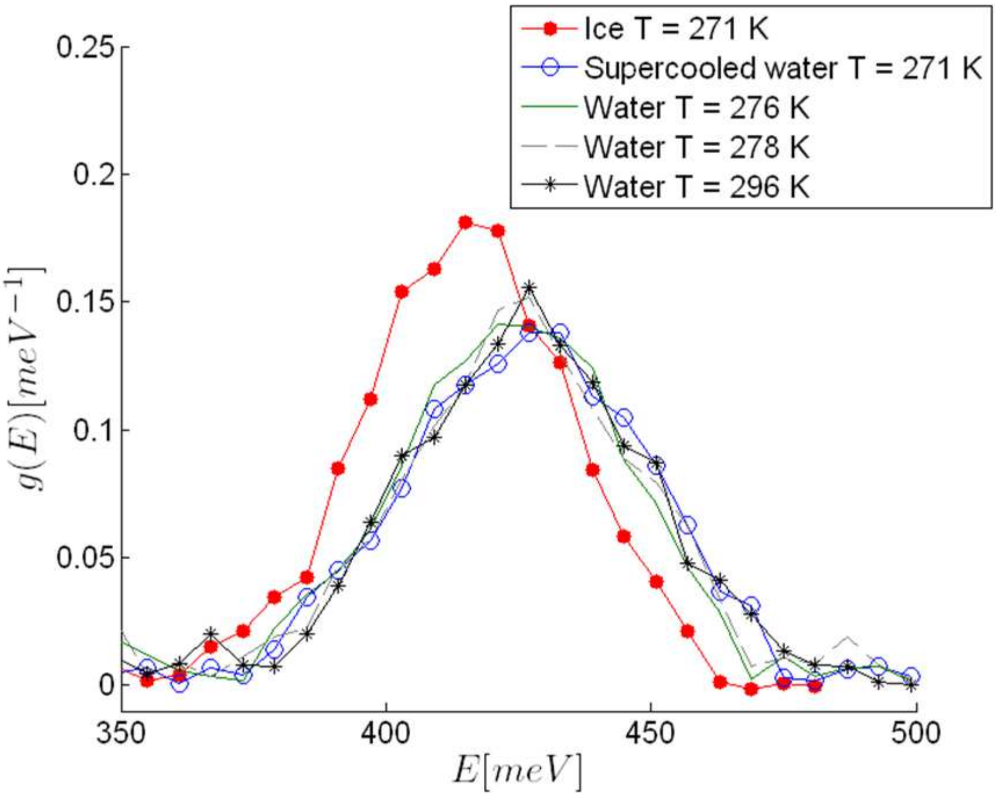

Figure 6.16: *Comparison among DOS of the supercooled water and ice at* $T = 271$ *K and stable water at temperatures: 276, 278, and 296 K. As expected from the vibrational spectra no appreciable change of the DOS is observed for water as the temperature is varied.*

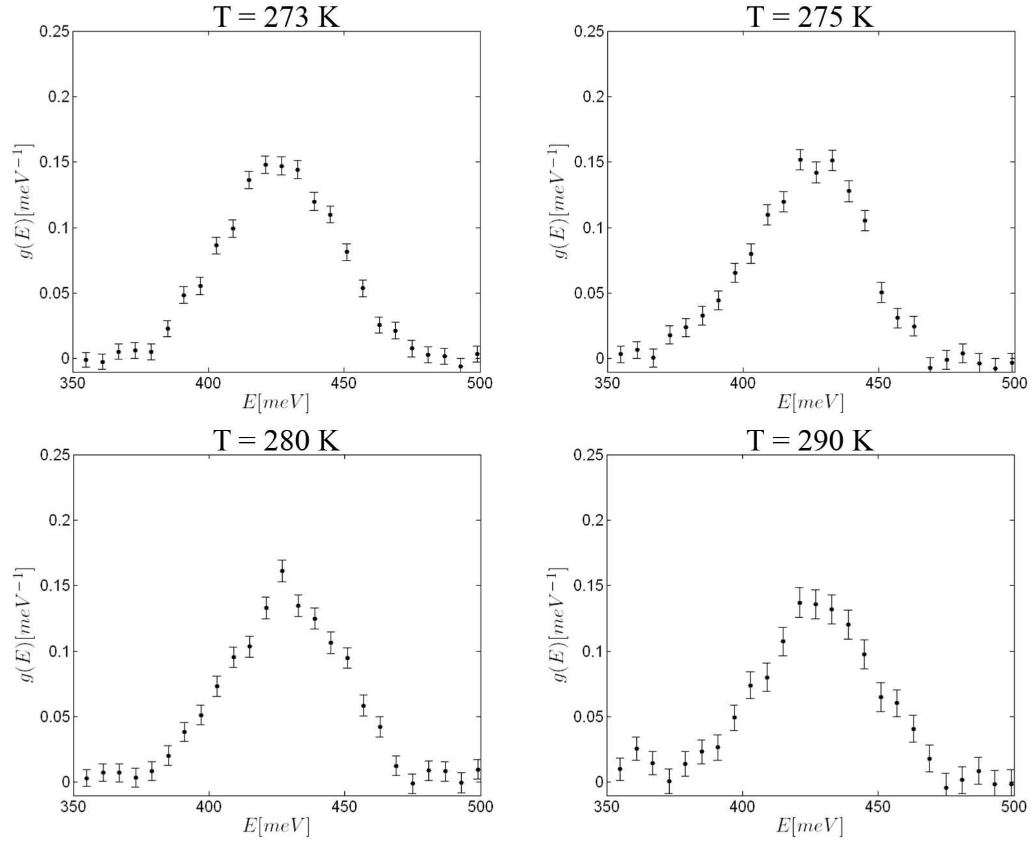

Figure 6.17: *DOS with error bars for water at T = 273, 275, 280 and 290 K.*

E=350 to 500 meV gives the contribution to the mean kinetic energy of the stretching mode:

$$\langle E_K \rangle_{Str} = \frac{3}{4} \int_{350}^{500} E g(\frac{E}{\hbar}) \coth \frac{E}{2k_B T} d(\frac{E}{\hbar}) \,, \tag{6.9}$$

where the integral variable has been changed from ω to E.

However, careful attention must be paid to the normalization condition. The equations 5.6 and 6.9 holds if the sum rule:

$$\int_0^{+\infty} g(\omega) d\omega = \int_0^{+\infty} \frac{1}{\hbar} g(E) dE = 1 \,. \tag{6.10}$$

is satisfied. This equation is the direct consequence of the fact that the density of states is a distribution function.

The procedure for the extraction of the DOS can be extended to the whole spectrum, we can then use these data to impose the correct normalization to the $g(E)$. However, in doing so we are introducing uncontrollable uncertainties due to the MS subtraction methods that is expected to work fine only in the stretching region. If we make the assumption that the MS is almost constant through the spectra at various temperatures we cannot extract reliable numbers, but we can compare results among them to have a numerical parameter to plot: we can then look for correlation between this numerical parameter (i.e. the $\langle E_K \rangle_{Str}$) and the temperature.

In figure 6.19 $\langle E_K \rangle_{Str}$ is reported as a function of the temperature, showing that there is no correlation between the mean proton kinetic energy and the temperature: the behavior is almost constant. It is worth noting that the 6.19 $\langle E_K \rangle_{Str}$ for ice is 85 ± 4 meV, in good agreement with the PICPMD value of 82 meV.

6.2 Conclusions

A DINS measurement on a polycrystalline ice Ih has been done at VESUVIO spectrometer at ISIS. New data analysis tools have been introduced for DINS measurements.

The direct numerical determination of the momentum distribution can be used to unambiguously identify nuclear quantum effects, the chemical environment, and the anisotropic-harmonic or anharmonic character of atomic motions in condensed systems. The numerical integration proposed in this work is intended to be part of a set of non-parametric determinations of the momentum distributions [144, 148, 149, 3], that can be used synergistically with the parametric fitting analysis, broadening the capabilities of the deep inelastic neutron scattering technique. Moreover, the direct numerical determination of $n(p)$ can be applied to the recent studies of heavier mass systems, such as lithium, oxygen, etc. [150, 151], that aim at assessing the magnitude of nuclear quantum fluctuations in any condensed matter system.

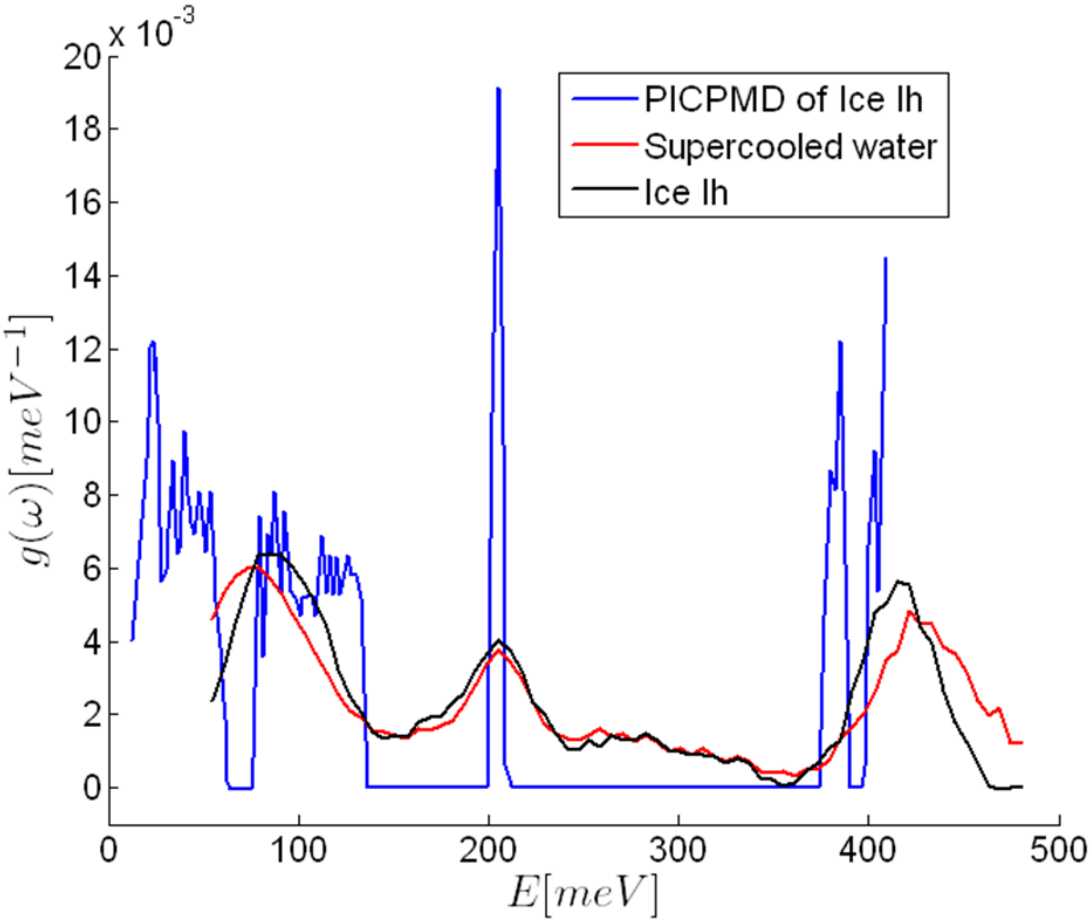

Figure 6.18: *Density of states for ice and supercooled water at T = 271 K and PICPMD for all energies.*

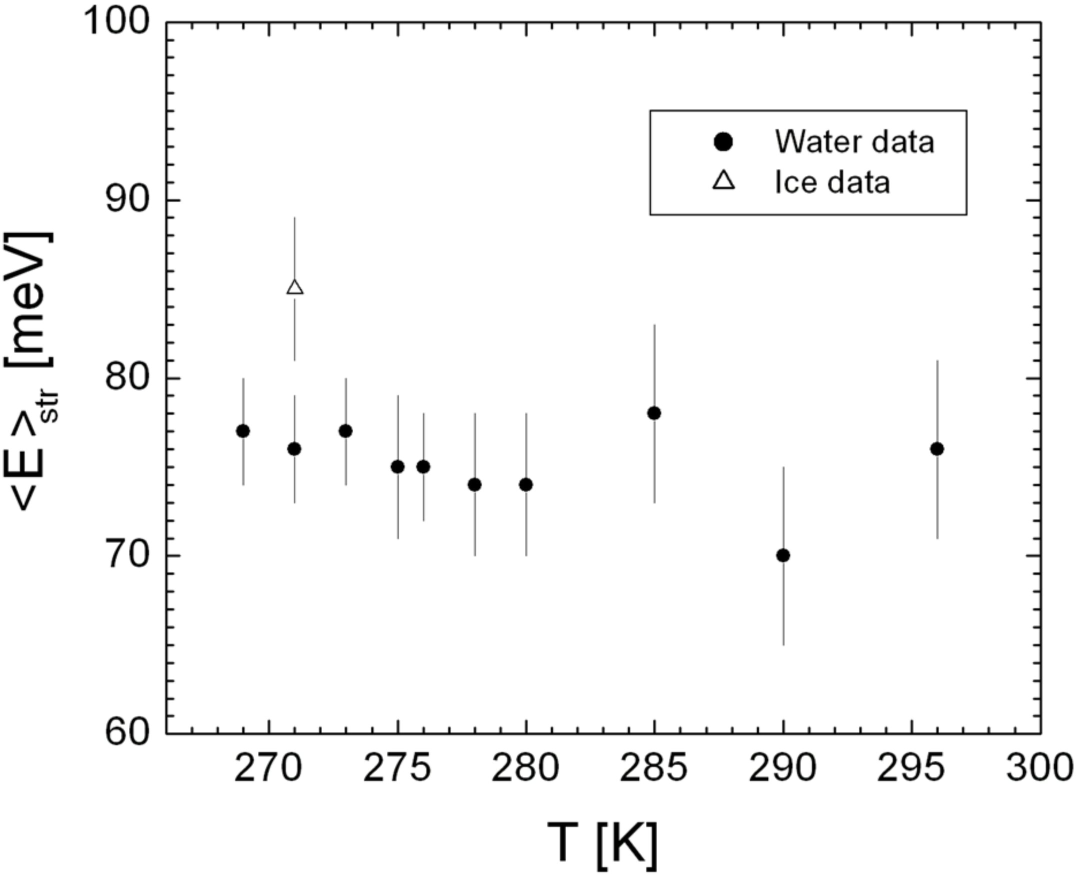

Figure 6.19: $\langle E_K \rangle_{Str}$ *as a function of the temperature, calculated by the equation 6.9.*

In contrast, the parametric models M1 and M2 yield to a smooth momentum distribution that must be related to the features of the model. The M1 line shape for example can fit to any momentum distribution, providing enough Hermite polynomials. However, the interpretation of the data would be difficult in terms of anisotropy and anharmonicity. The M2 model can only be applied for harmonic anisotropic momentum distribution. By putting together the information extracted from the models one conclusion can be drawn on the nature of the sample under analysis. In particular ice Ih at T=271 K results to have an harmonic anisotropic momentum distribution.

This work illustrates how the theoretical and experimental determination of the momentum distribution in a benchmark system like polycrystalline ice can directly access the physical mechanisms describing quantum state of the proton . We have successfully extracted the dominant features of the microscopic directional momentum distribution from an experiment on a macroscopically isotropic sample. Moreover, we have measured with high precision the non-trivial quantum excess kinetic energy, an observable that can be used as a quantitative benchmark for electronic density functionals employed in the description of hydrogen bonded systems in *ab initio* numerical simulations. An accurate measurement of the kinetic energy is in fact the most direct experimental probe of the spatial localization/delocalization of the proton, and can contribute to the development of better theoretical descriptions of water and hydrogen bonded systems in general. This study can be further used to investigate the role of nuclear quantum effects in a variety of hydrogen bonded systems.

Carrying out the same analysis on previous water data, it results that momentum distribution of supercooled water, showing a secondary peak at high momentum, cannot be described as an anisotropic model only: proton potential in these cases come out to have a not negligible anharmoic part. The same considerations holds for water at T = 277.15 K, the maximun density temperature for liquid water. Water around the melting point and near room temperature behaves as an harmonic anisotropic system.

A set of DINS measurements on a monocrystalline ice Ic on a Pt substrate has been carried out at VESUVIO spectrometer at T = 130 K. This experiment can be seen as the experimental way of extracting directional information from DINS, a complementary approach with respect to the polycristalline ice Ih.

We obtained an unexpected $\langle E_k \rangle$ value, that is smaller than the measured zero point kinetic energy of ice Ih. We infer from this experience and from that of the supercooled water that H-bonded systems could give rise to drastic change of the momentum distribution upon very small structural alterations. Although this experiment was planned for a directional analysis of ice we found an unexpected but very important result.

The constant $\hat{q}$ analysis yielded energy values decreasing as $\hat{q}$ approaches the $c-axis$.

All the momentum distributions are well represented by an harmonic isotropic model.

The huge excess of $\langle E_k \rangle$ in water, especially in the supercooled regime, was described in terms of a proton that can coherently tunnel among two wells of a double wells potential along the H-bond. This hypothesis should have as a consequence an evolution of the vibrational spectrum around the stretching region as a function of the temperature.

An INS experiment on pure H_2O has then been carried out on SEQUOIA spectrometer at the Oak Ridge National Laboratory in a range of temperature from 269 to 296 K for liquid water and 271 K for ice.

A model for the multiple scattering subtraction was used to correct the data. This simple model, used in Ref. [96], has been improved by fitting the dynamical structure factor tail. This made possible the extraction of the vibrational density of states for ice and water for all the investigated temperatures.

A clear picture arises from these measurements: the stretching mode does not change appreciably in passing from supercooled to room temperature water. For ice we found results in agreement with previous works.

6.3 Future developments

The data analysis developed for DINS measurement can be applied to any physical system for which a DINS measurement is reliable.

The combination between statistical data analysis and prior knowledge deriving from theoretical studies, or simulations, is a very powerful tool to determine the effective anisotropy or anharmonicity of a potential. This study can then pave the way for future works in this direction.

At present, the DINS measurement on ice Ic does not lead to a clear picture of the physics of such system. The constant $\hat{q}$ analysis, in particular requires more $\hat{q}$ values for a reliable analysis. The present analysis shows only three values, each of which contains a set of β varying over 20°. This is equivalent to sum up many contribution coming from, for example, $\hat{q}$ from 140° to 160° for the β value of 150°. Choosing a smaller interval of $\hat{q}$ would produce, with the present data, NCP with few data points, and as a consequence with a poor statistic and a very low reliability of the results. Instead, it would be desirable to have much more $\langle E_k \rangle$ as a function of $\hat{q}$. This can be obtained with new DINS measurement on the same system with different orientations of the $c - axis$. Furthermore the low value of zero point energy of the ice Ic rises the interest on measuring the same quantity for all the crystalline phases of ice.

The most important approximation done for the data analysis of the INS measurements is the subtraction of the multiple scattering. This procedure works well under certain conditions but limits the quantity of information that can be extracted from these data.

A MC simulation for the evaluation of the multiple scattering, for example, should be feasible. Many papers can be found in the literature on this topic. Once the multiple scattering is subtracted reliably in the whole spectrum the DOS can be extracted for all the spectra. In this way the also the total $\langle E_k \rangle$ will be available from the INS data.

Bibliography

[1] A list of the water anomalies is available on the web site http://www.lsbu.ac.uk/water/anmlies.html.

[2] The behavior of thermodynamical quantity of many fluids are available on the web site http://webbook.nist.gov/chemistry/fluid/.

[3] L. Lin, J. A. Morrone, R. Car, and M. Parrinello. Displaced Path Integral Formulation for the Momentum Distribution of Quantum Particles. *Physical Review Letters*, 105(11):110602, September 2010.

[4] W. S. Benedict, N. Gailar, and E. K. Plyler. Rotation-Vibration Spectra of Deuterated Water Vapor. *Journal of Chemical Physics*, 24:1139–1165, June 1956.

[5] S. A. Clough, Y. Beers, G. P. Klein, and L. S. Rothman. Dipole moment of water from Stark measurements of H_2O HDO, and D_2O. *Journal of Chemical Physics*, 59:2254–2259, September 1973.

[6] S. S. Xantheas and T. H. Dunning, Jr. Ab initio studies of cyclic water clusters $(H_2O)_n$, n=1-6. I. Optimal structures and vibrational spectra. *Journal of Chemical Physics*, 99:8774–8792, December 1993.

[7] W. M. Latimer and W. H. Rodebush. Polarity and ionization from the standpoint of the lewis theory of valence. *Journal of the American Chemical Society*, 42(7):1419–1433, 1920.

[8] P. Silvestroni. *Fondamenti di chimica.* Masson, 1997.

[9] F. H. Stillinger. Water Revisited. *Science*, 209:451–457, July 1980.

[10] V.F. Petrenko and R.W. Whitworth. *Physics of Ice.* Oxford University Press, New York, 1999.

[11] G. Tammann. *Annalen der Physik*, 2:1–31, 1900.

[12] L. Pauling. *Journal of the American Chemical Society*, 57:2680, 1935.

[13] U. Nakaya. *Snow crystals - natural and artificial.* Harvard University Press, Cambridge, 1954.

[14] T. Kobayashi. *Phylosophical Magazine*, 6:1363–70, 1961.

[15] F. Liu, I. Baker, G. Yao, and M. Dudley. Dislocations and grain boundaries in polycrystalline ice: a preliminary study by synchrotron X-ray topography. *Journal of Materials Science*, 27:2719–2725, 1992.

[16] U. Nakaya. *Mechanical proprieties of single crystal of ice. Part I Geometry of deformation.* Us Army Snow Ice and Permafrost Research Estabilishment Research Report no. 28, 1958.

[17] G. Turner. The manufacture of large samples of monocrystalline ice under microcomputer control. *Journal of Crystal Growth*, 80:463–464, February 1987.

[18] C. A. Knight. A simple technique for growing large, optically "perfect" ice crystals. *Journal of Glaciology*, 42:585–587, 1996.

[19] V. F. Petrenko, N. N. Khusnatdinov, V. V. Petrenko, and O. V. Nickolayev. Study of the Structure and Electrical Properties of the Liquid-Like Layer on Ice/Air, Ice/Solid and Ice/Liquid Interfaces. In *APS March Meeting Abstracts*, page 109, March 1996.

[20] M. Oguro. *Lattice defects in ice single crystals.* Hokkaido University Press, Sapporo, 1988.

[21] M. Ohtomo, S. Ahmad, and R. W. Whitworth. A technique for the growth of high quality single crystals of ice. *Journal de Physique Colloques*, 48:C1–595–C1–598, 1987.

[22] G. E. Jauncey. Quantum Theory of the Unmodified Spectrum Line in the Compton Effect. *Physical Review*, 25:314–321, March 1925.

[23] J. W. Du Mond. Compton Modified Line Structure and its Relation to the Electron Theory of Solid Bodies. *Physical Review*, 33:643–658, May 1929.

[24] V. F. Sears. Scaling and final-state interactions in deep-inelastic neutron scattering. *Physical Review B*, 30:44–51, July 1984.

[25] G. K. Ivanov and Y. S. Sayasov. Theory of the Vibrational Excitation of a Molecule in the Impulse Approximation. *Soviet Physics Doklady*, 9:171–+, August 1964.

[26] P. C. Hohenberg and P. M. Platzman. High-Energy Neutron Scattering from Liquid He^4. *Physical Review*, 152:198–200, December 1966.

[27] O. K. Harling. High-Momentum-Transfer Neutron-Liquid-Helium Scattering bose Condensation. *Physical Review Letters*, 24:1046–1048, May 1970.

[28] H. A. Mook. Neutron-Scattering Study of the Momentum Distribution of ^{4}He. *Physical Review Letters*, 32:1167–1170, May 1974.

[29] H. A. Mook. Density Dependence of the Momentum Distribution for ^{4}He. *Physical Review Letters*, 51:1454–1456, October 1983.

[30] P. Martel, E. C. Svensson, A. D. B. Woods, V. F. Sears, and R. A. Cowley. Neutron scattering from superfluid helium at large momentum transfers. *Journal of Low Temperature Physics*, 23:285–301, May 1976.

[31] V. F. Sears, E. C. Svensson, P. Martel, and A. D. B. Woods. Neutron-Scattering Determination of the Momentum Distribution and the Condensate Fraction in Liquid ^{4}He. *Physical Review Letters*, 49:279–282, July 1982.

[32] S. Ikeda and N. Watanabe. Neutron scattering from superfluid ^{4}He at very large momentum transfer. *Physics Letters A*, 121:34–38, March 1987.

[33] T. R. Sosnick, W. M. Snow, P. E. Sokol, and R. N. Silver. Momentum distributions in liquid ^{4}He. *EPL (Europhysics Letters)*, 9:707, August 1989.

[34] T. R. Sosnick, W. M. Snow, and P. E. Sokol. Deep-inelastic neutron scattering from liquid ^{4}He. *Physical Review B*, 41:11185–11202, June 1990.

[35] T. R. Sosnick, W. M. Snow, R. N. Silver, and P. E. Sokol. Deviations from the impulse approximation in liquid ^{4}He: An experimental test at Q=23 $Å^{-1}$. *Physical Review B*, 43:216–228, January 1991.

[36] C. Andreani, G. Baciocco, R. S. Holt, and J. Mayers. Resolution in deep inelastic neutron scattering using pulsed neutron sources. *Nuclear Instruments and Methods in Physics Research A*, 276:297–305, March 1989.

[37] P. Postorino, F. Fillaux, J. Mayers, J. Tomkinson, and R. S. Holt. The anisotropy of the proton momentum distribution in $KHCO_3$: A deep inelastic neutron scattering study. *Journal of Chemical Physics*, 94:4411–4415, March 1991.

[38] F. Fillaux, A. Lautié, R. Papoular, S. M. Bennington, and J. Tomkinson. Free proton dynamics in coal. *Physica B Condensed Matter*, 213:631–633, February 1995.

[39] A. C. Evans, D. N. Timms, J. Mayers, and S. M. Bennington. Neutron-scattering study of the impulse approximation in ZrH_2. *Physical Review B*, 53:3023–3031, February 1996.

[40] A. L. Fielding, D. N. Timms, A. C. Evans, and J. Mayers. Final-state effects in neutron Compton scattering measurements on zirconium deuteride and beryllium. *Journal of Physics Condensed Matter*, 8:7205–7219, September 1996.

[41] D. Nemirovsky, R. Moreh, K. H. Andersen, and J. Mayers. Study of the momentum distribution of a Zn single crystal using neutron Compton scattering. *Journal of Physics Condensed Matter*, 12:4293–4302, May 2000.

[42] P. H. C. Mitchell, D. A. Green, E. Payen, and A. C. Evans. *Journal of the Chemical Society, Faraday Transactions*, 91:4467, January 1995.

[43] M. Mayers J. Gray, E.M.A. Kemali and J. Noreland. . *Journal of Alloys and Compounds*, 253:291, January 1997.

[44] F. J. Bermejo, F. J. Mompeán, A. Srinivasan, J. Mayers, and A. C. Evans. Deep inelastic neutron scattering as a tool for the investigation of glassy dynamics. *Physics Letters A*, 189:333–339, June 1994.

[45] J. Dawidowski, F. J. Bermejo, L. F. Barquín, P. Gorria, J. M. Barandiarán, A. C. Evans, and J. Mayers. Short-time dynamics on a metallic glass as probed by deep inelastic neutron scattering. *Physics Letters A*, 214:59–64, February 1996.

[46] C. Andreani, A. Filabozzi, M. Nardone, F. P. Ricci, and J. Mayers. Quantum and classical behavior of single-particle dynamics in dense liquid ^{4}He. *Physical Review B*, 50:12744–12746, November 1994.

[47] J. Mayers, T. M. Burke, and R. J. Newport. Neutron Compton scattering from amorphous hydrogenated carbon. *Journal of Physics Condensed Matter*, 6:641–658, January 1994.

[48] C. A. Chatzidimitriou-Dreismann, T. Abdul Redah, R. M. F. Streffer, and J. Mayers. Anomalous deep inelastic neutron scattering from liquid h_2o-d_2o: Evidence of nuclear quantum entanglement. *Physical Review Letters*, 79:2839–2842, Oct 1997.

[49] M. Celli, M. Zoppi, and J. Mayers. Kinetic energy of ^{4}He along the T=6.1 K isotherm. *Physical Review B*, 58:242–247, July 1998.

[50] U. Bafile, M. Zoppi, F. Barocchi, R. Magli, and J. Mayers. Density evolution of the kinetic energy of fluid and solid ^{4}He at T=6.1 K. *Physical Review B*, 54:11969–11972, November 1996.

[51] D. Nemirovsky, R. Moreh, K. H. Andersen, and J. Mayers. Anomalous kinetic energies of adsorbed ^{4}He on active carbon fibre (ACF). *Journal of Physics Condensed Matter*, 11:6653–6660, September 1999.

[52] D. Nemirovsky. Kinetic energy of neon atoms adsorbed on activated carbon. *Surface Science*, 526:282–290, March 2003.

[53] C. Andreani, D. Colognesi, J. Mayers, G. F. Reiter, and R. Senesi. Measurement of momentum distribution of lightatoms and molecules in condensed matter systems using inelastic neutron scattering. *Advances in Physics*, 54:377–469, 2005.

[54] L. Tisza. Transport Phenomena in Helium II. *Nature*, 141:913, May 1938.

[55] E. L. Andronikashvili and Y. G. Mamaladze. *Rotation of helium II in Progress in Low Temperature Physics V.* C.J. Gorter, ed., Amsterdam, 1967.

[56] A. Miller, D. Pines, and P. Nozières. Elementary Excitations in Liquid Helium. *Physical Review*, 127:1452–1464, September 1962.

[57] R. A. Cowley and A. D. Woods. Neutron Scattering from Liquid Helium at High Energies. *Physical Review Letters*, 21:787–789, September 1968.

[58] G. C. Windsor. *Pulsed Neutron Scattering.* Taylor & Francis Ltd., London, 1981.

[59] R. N. Silver and P. E. Sokol. *Momentum Distributions.* Plenum, New York, 1989.

[60] J. Mayers, C. Andreani, and D. Colognesi. Measurement of the kinetic energy in ? through the superfluid transition by very high-energy neutron scattering. *Journal of Physics Condensed Matter*, 9:10639–10649, December 1997.

[61] J. Mayers, F. Albergamo, and D. Timms. Measurements of the atomic kinetic energy of ^{4}He close to the superfluid transition. *Physica B Condensed Matter*, 276:811–813, March 2000.

[62] D. M. Ceperley and E. L. Pollock. The momentum distribution of normal and superfluid liquid ^{4}He. *Canadian Journal of Physics*, 65:1416, 1987.

[63] H. R. Glyde, R. T. Azuah, and W. G. Stirling. Condensate, momentum distribution, and final-state effects in liquid ^{4}He. *Physical Review B*, 62:14337–14349, December 2000.

[64] M. Nardone F. Albergamo and A. Filabozzi. *Physical Review B*, 56:14614, 1997.

[65] D. Colognesi, C. Andreani, and R. Senesi. Single-particle mean kinetic energy in low-density supercritical ^{4}He. *EPL (Europhysics Letters)*, 50:202–208, April 2000.

[66] S. Ikeda and N. Watanabe. Neutron scattering from superfluid 4he at very large momentum transfer. *Physics Letters A*, 121(1):34 – 38, 1987.

[67] K. W. Herwig, P. E. Sokol, T. R. Sosnick, W. M. Snow, and R. C. Blasdell. Density dependence of the momentum distribution in normal liquid ^{4}He. *Physical Review B*, 41:103–110, January 1990.

[68] D. M. Ceperley and E. L. Pollock. *Physical Review Letters*, 56:351–354, January 1986.

[69] H. R. Glyde. Momentum distributions and final-state effects in neutron scattering. *Physical Review B*, 50:6726–6742, September 1994.

[70] R. T. Azuah, W. G. Stirling, K. Guckelsberger, R. Scherm, S. M. Bennignton, M. L. Yates, and A. D. Taylor. *Journal of Low Temperature Physics*, 101:951–969, December 1995.

[71] K. H. Andersen, W. G. Stirling, and H. R. Glyde. Momentum distribution and final-state effects in liquid ^{4}He. *Physical Review B*, 56:8978–8987, October 1997.

[72] R. T. Azuah, W. G. Stirling, H. R. Glyde, M. Boninsegni, P. E. Sokol, and S. M. Bennington. Condensate and final-state effects in superfluid ^{4}He. *Physical Review B*, 56:14620–14630, December 1997.

[73] H. R. Glyde. *Excitations in Liquid and Solid Helium.* Clarendon, Oxford, 1994.

[74] H. R. Glyde, R. T. Azuah, and W. G. Stirling. *Physical Review B*, 62:14337–14349, December 2000.

[75] R. Senesi, C. Andreani, D. Colognesi, A. Cunsolo, and M. Nardone. Deep-Inelastic Neutron Scattering Determination of the Single-Particle Kinetic Energy in Solid and Liquid ^{3}He. *Physical Review Letters*, 86:4584–4587, May 2001.

[76] S. Moroni, F. Pederiva, S. Fantoni, and M. Boninsegni. Equation of State of Solid ^{3}He. *Physical Review Letters*, 84:2650–2653, March 2000.

[77] G. I. Watson. *Journal of Physics: Condensed Matter*, 8:5955–5975, August 1996.

[78] J. Mayers. Measurement of the proton wave function in molecular hydrogen by neutron Compton scattering. *Physical Review Letters*, 71:1553–1556, September 1993.

[79] G. Reiter and R. Silver. Measurement of interionic potentials in solids using deep-inelastic neutron scattering. *Physical Review Letters*, 54:1047–1050, March 1985.

[80] G. F. Reiter, R. N. Silver, and P. E. Sokol. *Momentum Distributions.* Plenum, New York, 1989.

[81] D. Flammini, M. A. Ricci, and F. Bruni. A new water anomaly: The temperature dependence of the proton mean kinetic energy. *Journal of Chemical Physics*, 130(23):236101, June 2009.

[82] A. Pietropaolo, R. Senesi, C. Andreani, A. Botti, M. A. Ricci, and F. Bruni. Excess of Proton Mean Kinetic Energy in Supercooled Water. *Physical Review Letters*, 100(12):127802, March 2008.

[83] R. Moreh and D. Nemirovsky. On the proton kinetic energy in H_2O and in nanotube water. *Journal of Chemical Physics*, 133(8):084506–+, August 2010.

[84] G. F. Reiter, J. C. Li, J. Mayers, T. Abdul-Redah, and P. Platzman. The Proton Momentum Distribution in Water and Ice. *Brazilian Journal of Physics*, 34:142–147, March 2004.

[85] E. M. Schooneveld, J. Mayers, N. J. Rhodes, A. Pietropaolo, C. Andreani, R. Senesi, G. Gorini, E. Perelli-Cippo, and M. Tardocchi. Foil cycling technique for the VESUVIO spectrometer operating in the resonance detector configuration. *Review of Scientific Instruments*, 77(9):095103, September 2006.

[86] C. Andreani, D. Colognesi, E. Degiorgi, and M. A. Ricci. Proton dynamics in supercritical water. *Journal of Chemical Physics*, 115:11243–11248, December 2001.

[87] A. Pietropaolo, C. Andreani, A. Filabozzi, R. Senesi, G. Gorini, E. Perelli-Cippo, M. Tardocchi, N. J. Rhodes, and E. M. Schooneveld. DINS measurements on VESUVIO in the Resonance Detector configuration: proton mean kinetic energy in water. *Journal of Instrumentation*, 1:4001, April 2006.

[88] U. Bafile, M. Zoppi, F. Barocchi, R. Magli, and J. Mayers. Momentum Distribution of ^{4}He across the Melting Transition. *Physical Review Letters*, 75:1957–1960, September 1995.

[89] J. R. Errington and P. G. Debenedetti. Relationship between structural order and the anomalies of liquid water. *Nature*, 409:318–321, January 2001.

[90] F. A. Deeney and J. P. O'Leary. Zero point energy and the origin of the density maximum in water. *Physics Letters A*, 372:1551–1554, March 2008.

[91] F. Paesani, S. Iuchi, and G. A. Voth. Quantum effects in liquid water from an ab initio-based polarizable force field. *Journal of Chemical Physics*, 127(7):074506, August 2007.

[92] A. Botti, F. Bruni, A. Isopo, M. A. Ricci, and A. K. Soper. Experimental determination of the site-site radial distribution functions of supercooled ultrapure bulk water. *Journal of Chemical Physics*, 117:6196–6199, October 2002.

[93] F. Ricci, M.A. Bruni and A. Giuliani. Similarities between confined and supercooled water. *Faraday Discussions*, 141:347–358, 2009.

[94] P. C. H. Mitchell, S. F. Parker, A. J. Ramirez-Cuesta, and J. Tomkinson. *Vibrational Spectroscopy with Neutrons*. World Scientific, Singapore, 2005.

[95] O. K. Harling. Slow Neutron Inelastic Scattering Study of Light Water and Ice. *Journal of Chemical Physics*, 50:5279–5296, June 1969.

[96] C. Andreani, P. Bosi, F. Sacchetti, and C. K. Loong. Absolute measurements of the stretching mode density of states in polycrystalline ice Ih. *Journal of Chemical Physics*, 83:750–753, July 1985.

[97] G. E. Walrafen. Raman Spectral Studies of Water Structure. *Journal of Chemical Physics*, 40:3249–3256, June 1964.

[98] J. R. D. Copley, D. L. Price, and J. M. Rowe. *Nuclear Instruments and Methods*, 107:501, 1973.

[99] C. Andreani, V. Merlo, and M. A. Ricci. A procedure for multiple scattering corrections in a neutron incoherent inelastic scattering experiment. *Nuclear Instruments and Methods in Physics Research B*, 36:216–221, February 1989.

[100] V. F. Sears. Slow-neutron multiple scattering. *Advances in Physics*, 24:1–45, January 1975.

[101] L. Lin, J. A. Morrone, R. Car, and M. Parrinello. Momentum distribution, vibrational dynamics, and the potential of mean force in ice. *Physical Review B*, 83(22):220302, June 2011.

[102] V. Garbuio, C. Andreani, S. Imberti, A. Pietropaolo, G. F. Reiter, R. Senesi, and M. A. Ricci. Proton quantum coherence observed in water confined in silica nanopores. *Journal of Chemical Physics*, 127(15):154501, October 2007.

[103] A. K. Soper. Comment on “Excess of Proton Mean Kinetic Energy in Supercooled Water”. *Physical Review Letters*, 103(6):069801, August 2009.

[104] G. Reiter, J. C. Li, J. Mayers, T. Abdul-Redah, and P. Platzmann. Erratum: The Proton Momentum Distribution in Water and Ice. *Brazilian Journal of Physics*, 34:334, March 2004.

[105] S. Haq, C. Clay, G. R. Darling, G. Zimbitas, and A. Hodgson. Growth of intact water ice on Ru(0001) between 140 and 160K : Experiment and density-functional theory calculations. *Physical Review B*, 73(11):115414, March 2006.

[106] U. Starke. A low-energy electron diffraction study of oxygen, water and ice adsorption on Pt(111). *Surface Science*, 287:432–437, May 1993.

[107] U. Starke. Ethylidyne on Pt(111): Determination of adsorption site, substrate relaxation and coverage by automated tensor LEED. *Surface Science*, 286:1–14, April 1993.

[108] N. Materer, A. Barbieri, D. Gardin, U. Starke, J. D. Batteas, M. A. van Hove, and G. A. Somorjai. Hollow-site molecular adsorption for NO on Pt(111) and Ni(111): Invalidating vibrational site assignment rules. *Physical Review B*, 48:2859–2861, July 1993.

[109] A. Hodgson and S. Haq. Water adsorption and the wetting of metal surfaces. *Surface Science Reports*, 64:381–451, September 2009.

[110] G.L. Squires. *Thermal Neutron Scattering.* Dover, New York, 1996.

[111] G.L Squires. *Introduction to the theory of thermal neutron scattering.* Cambridge University Press, Cambridge, 1978.

[112] D. D. Fitts. *Principles of quantum mechanics as applied to chemistry and and chemical physics.* Cambridge University Press, Cambridge, 1999.

[113] V. F. Sears. Neutron scattering lengths and cross sections. *Neutron News*, 3(3):26–37, 1992.

[114] G. K. Ivanov and Y. S. Sayasov. Reviews of Topical Problems: Interaction of Neutrons with Molecules. *Soviet Physics Uspekhi*, 9:670–691, May 1967.

[115] G. K. Ivanov and Y. S. Sayasov. Direct Atomic-molecular or Ionic-molecular Reactions. *ZhETF Pis ma Redaktsiiu*, 3:40, January 1966.

[116] C. Ciofi Degli Atti, E. Pace, and G. Salmè. y-scaling analysis of quasielastic electron scattering and nucleon momentum distributions in few-body systems, complex nuclei, and nuclear matter. *Physical Review C*, 43:1155–1176, March 1991.

[117] J. Mayers. Quantum effects in deep inelastic neutron scattering. *Physical Review B*, 41:41–51, January 1990.

[118] N. F. Mott and H. S. W. Massey. *Theory of Atomic Collision*. Oxord University Press, London, 1949.

[119] G. B. West. Electron scattering from atoms, nuclei and nucleons. *Physics Reports*, 18:263–323, June 1975.

[120] H. A. Gersch, L. J. Rodriguez, and P. N. Smith. Corrections to the Impulse Approximation for High-Energy Neutron Scattering from Liquid Helium. *Physical Review A*, 5:1547–1558, March 1972.

[121] H. A. Gersch and L. J. Rodriguez. Final-State Effects on Thermal-Neutron Scattering at High-Energy Transfer. *Physical Review A*, 8:905–912, August 1973.

[122] J. Mayers, C. Andreani, and G. Baciocco. Initial state effects in deep inelastic neutron scattering. *Physical Review B*, 39:2022–2028, February 1989.

[123] S. W. Lovesey. *Theory of Neutron Scattering from Condensed Matter*. Oxford University Press, Oxford, 1987.

[124] A. Pietropaolo. *Research and development of γ rays detectors for neutron scattering at electron Volt energies on VESUVIO spectrometer*. PhD thesis, Università degli studi di Roma Tor Vergata, 2004.

[125] C. Andreani, E. Degiorgi, R. Senesi, F. Cilloco, D. Colognesi, J. Mayers, M. Nardone, and E. Pace. Single particle dynamics in fluid and solid hydrogen sulphide: An inelastic neutron scattering study. *Journal of Chemical Physics*, 114:387–398, January 2001.

[126] L. Lin, J. Morrone, R. Car, and M. Parrinello. Nuclear momentum distribution and potential energy surface in hexagonal ice. In *APS Meeting Abstracts*, page 41006, March 2011.

[127] J. Olivero. Empirical fits to the Voigt line width: A brief review. *Journal of Quantitative Spectroscopy and Radiative Transfer*, 17:233–236, February 1977.

[128] T. R. Sosnick, W. M. Snow, and P. E. Sokol. Deep-inelastic neutron scattering from liquid ^{4}He. *Physical Review B*, 41:11185–11202, June 1990.

[129] M. E. Davison. A singular value decomposition for the radon transform in n-dimensional euclidean space. *Numerical Functional Analysis and Optimization*, 3(3):321–340, 1981.

[130] M. E. Davison and F. A. Grunbaum. Tomographic reconstruction with arbitrary directions. *Communications on Pure and Applied Mathematics*, 34(1):77–119, 1981.

[131] D. Marx and M. Parrinello. Ab initio path integral molecular dynamics: Basic ideas. *Journal of Chemical Physics*, 104:4077–4082, March 1996.

[132] F. James. Minuit minimization package, 1994.

[133] F. McBride. Private comunication.

[134] http://www.nndc.bnl.gov/exfor/cinda.htm.

[135] H. D. Young. *Statistical treatment of experimental data.* McGraw-Hill, 1962.

[136] R. Senesi, A. Pietropaolo, and C. Andreani. Constant-q data representation in Neutron Compton scattering on the VESUVIO spectrometer. *Nuclear Instruments and Methods in Physics Research A*, 594:244–252, September 2008.

[137] K. Toukan, M. A. Ricci, S.-H. Chen, C.-K. Loong, D. L. Price, and J. Teixeira. Neutron-scattering measurements of wave-vector-dependent hydrogen density of states in liquid water. *Physical Review A*, 37:2580–2589, April 1988.

[138] K. Toukan and A. Rahman. Molecular-dynamics study of atomic motions in water. *Physical Review B*, 31:2643–2648, March 1985.

[139] D. D. Klug, E. Whalley, E. C. Svensson, J. H. Root, and V. F. Sears. Densities of vibrational states and heat capacities of crystalline and amorphous H_2O ice determined by neutron scattering. *Physical Review B*, 44:841–844, July 1991.

[140] E. Perelli-Cippo, G. Gorini, M. Tardocchi, C. Andreani, A. Pietropaolo, R. Senesi, N. J. Rhodes, and E. M. Schooneveld. The O H stretching band in ice Ih derived via eV neutron spectroscopy on VESUVIO using the new very low angle detector bank. *Applied Physics A: Materials Science & Processing*, 83:453–460, June 2006.

[141] W. C. Kerr and K. S. Singwi. Neutron Scattering by Liquid Neon. *Physical Review A*, 7:1043–1054, March 1973.

[142] D. Ruppert. *Statistics and Data Analysis for Financial Engineering.* Springer Science, New York, 2010.

[143] A. J. Cohen, P. Mori-Sánchez, and W. Yang. Insights into Current Limitations of Density Functional Theory. *Science*, 321:792–, August 2008.

[144] D. Flammini, A. Pietropaolo, R. Senesi, C. Andreani, F. McBride, A. Hodgson, M. A. Adams, L. Lin, and R. Car. Spherical momentum distribution of the protons in hexagonal ice from modeling of inelastic neutron scattering data. *Journal of Chemical Physics*, 136(2):024504, January 2012.

[145] M. Planck. *Verhandlungen der Deutschen Physikalischen Gesellschaft*, 13:138, 1911.

[146] G. Reiter, C. Burnham, D. Homouz, P. M. Platzman, J. Mayers, T. Abdul-Redah, A. P. Moravsky, J. C. Li, C.-K. Loong, and A. I. Kolesnikov. Anomalous Behavior of Proton Zero Point Motion in Water Confined in Carbon Nanotubes. *Physical Review Letters*, 97(24):247801, December 2006.

[147] A. Botti, F. Bruni, A. Isopo, M. A. Ricci, and A. K. Soper. Experimental determination of the site-site radial distribution functions of supercooled ultrapure bulk water. *Journal of Chemical Physics*, 117:6196–6199, October 2002.

[148] R. Senesi. Direct kinetic energy extraction from neutron Compton profiles. *Nuclear Instruments and Methods in Physics Research A*, 661:70–76, January 2012.

[149] M. Krzystyniak, M.A. Adams, A. Lovell, N. T. Skipper, S. M. Bennington, J. Mayers, and F. Fernandez-Alonso. *Faraday Discussion*, 151:171, January 2011.

[150] M. Ceriotti and D. E. Manolopoulos. Efficient First-Principles Calculation of the Quantum Kinetic Energy and Momentum Distribution of Nuclei. *Physical Review Letters*, 109(10):100604, September 2012.

[151] A. G. Seel, M. Ceriotti, P. P. Edwards, and J. Mayers. Simultaneous measurement of lithium and fluorine momentum in ^{7}LiF. *Journal of Physics Condensed Matter*, 24:J5401, September 2012.

Acknowledgments

First of all I desire to acknowledge professor Carla Andreani.

She gave me the possibility, three years ago, to join her group, beginning an interesting and important activity on neutron spectroscopy. During these three years she fully enrolled me in the research activity of the group, under her constant and patient supervision. Her physical intuition and great experience in condensed matter physics have been a continuous stimulus and guide for my research activity.

I desire to warmly acknowledge Dr. Roberto Senesi who, starting from the first day of work together, gave me his friendship and collaboration, transmitting his great professional skills and his deep knowledge on neutron instrumentation and scattering techniques, teaching me the basis of the VESUVIO$'$s data analysis procedures.

A special thank is directed to Dr. Tonino Pietropaolo for great help and collaboration during my work, suggestions for the development of the data analysis and for precious and interesting scientific discussions.

I desire to further acknowledge the group of Prof. Roberto Car, and especially Lin Lin, from the Princeton University, for their collaboration in the development of the data analysis and for important and stimulating discussions which have been of paramount importance in writing experimental papers together. I want to acknowledge Dr. Mauro Barrui for teaching me the basis of the programming languages, Dr. Stefano P. Brunetti for his wise advices and Dr. Roberto Flammini for his precious suggestion for writing this thesis. Last but not least, Prof. Andrew Hodgson and Dr. Fiona McBride of University of Liverpool, for their professional and friendly collaboration during all the experiments.